VOLTAGE INDUCED OPTICAL WAVEGUIDE MODULATORS IN LITHIUM NIOBATE

by

NICOLAS AUGUST FLEMING JAEGER

B.Sc.E.E., The University of the Pacific, 1981

M.A.Sc., The University of British Columbia, 1986

A THESIS SUBMITTED IN PARTIAL FULFILLMENT

OF THE REQUIREMENTS FOR THE DEGREE OF

DOCTOR OF PHILOSOPHY

in

THE FACULTY OF GRADUATE STUDIES

DEPARTMENT OF ELECTRICAL ENGINEERING

We accept this thesis as conforming

to the required standards

THE UNIVERSITY OF BRITISH COLUMBIA

March 1989

In presenting this thesis in partial fulfilment of the requirements for an advanced degree at the University of British Columbia, I agree that the Library shall make it freely available for reference and study. I further agree that permission for extensive copying of this thesis for scholarly purposes may be granted by the head of my department or by his or her representatives. It is understood that copying or publication of this thesis for financial gain shall not be allowed without my written permission.

Department of ELECTRICAL ENGINEERING

The University of British Columbia
Vancouver, Canada

Date April 21, 1989

Abstract

Two types of optical modulator were studied, both of the voltage induced optical waveguide type first proposed and demonstrated by Channin in 1971. An optical waveguide was created in an electrooptic substrate by applying voltage between two electrodes deposited on the substrate. Channin used wide electrode spacings which resulted in large operating voltages being necessary. The devices discussed in this thesis had much smaller electrode spacings and therefore operated at much reduced voltages. They are of the planar and ridge types. In the planar type the electrodes were deposited on top of a planar substrate and in the ridge type a ridge of electrooptic material separated thick electrodes. The theory of operation for both types of device was developed and they were modeled, fabricated, and tested. Numerically derived results were obtained for light with wavelengths of 442 and 633 nm which showed that the confinement of the light increased with increasing voltage, decreasing gap width, and decreasing wavelength. The theory was further developed to investigate the performance of the device as a voltage-controlled linking waveguide between two optical fibers. The optimum coupling efficiency, as a function of voltage and interelectrode gap width, from optical fibers to both types of device was calculated in terms of the model. Key aspects of the theory were

confirmed by the measurements made on the fabricated devices. A planar device was used as a front-end switch between a laser and an optical fiber using a V-groove etched in silicon to align the voltage induced waveguide with the fiber. One problem was a decay phenomenon in which the induced waveguide disappeared over a period of time during which a constant voltage was applied to the electrodes. This was believed to be due to the photorefractive effect. It was found that the device would recover upon the application of a fly-back cycle.

Table of Contents

List of Figures

Acknowledgments

This part is easy. My parents have been the greatest help to me thoughout this work. Without their support and guidance I doubt that I ever would have reached this point. They deserve and receive my deepest love, thanks, and appreciation. Next to my parents Dr. L. Young deserves my gratitude and thanks. Without his guidance and support I surely would never have found an interest in integrated optics, an area of research that I thoroughly enjoy. This has been a most important contribution to my life.

Now things get a little more difficult. While several people stand out in my mind as having made my life as a graduate student tolerable, even enjoyable, it is hard to say who has contributed what. There are those who have directly contributed to my research either through actions or through discussions. There are also those who, by being available as friends, made the hardest times somewhat easier and thereby made it possible to keep on going. When I try to sort out the one group from the other I find that the fringes begin to blur and many of the same faces appear in my minds eye on either side. When I try to differentiate those who should be mentioned from those who should not I find a department full of shoulds and an empty column of should nots. I can think of no one who has not touched me in some way that has effected who I am and what I have done.

Yet if I thank one and all and mention no one in particular I will not be being true to those who were most true to me. I have, therefore, compiled a list of those people who, for one reason or another will always be part of my memory of what graduate studies truly was. I am sure that the faces of these people will linger in my memory long after the trials and tribulations are forgotten, longer even than the subject matter of my theses. I cannot list everything that each of the following people has done for me nor can I attach a weight to the importance of my interactions with them, I am sure that each one of them knows, I would just like to give them all my special thanks: I. Abdel-Motaleb, B. Ahlborn, N. Beaulieu, M. Beddose, F. Berry, E. Bohn, D. Boshier, K. Brindamour, J. Clark, A. Choi, D. Daines, J. Dindo, S. Dindo, H. Dommel, R. Donaldson, C. Dumont, D. Fletcher, B. Guidici, D. Hui, C. Jaeger, N. Jaeger, R. Jankowski, E. Jull, H. Kato, M. Kharadly, A. MacKenzie, P. Matz, D. Michelson, C. Nesbitt, C. Passmore, W. Passmore, A. Prince, G. Schmidt, C. Sheffield, L. Snider, C. Sudhakar, P. Townsley, J. Weber, L. Wedepohl, and M. Wvong. (And that is the short list!).

To those not listed above, thank you.

Chapter 1

INTRODUCTION

Integrated optics is the name given to the analysis, design, study, and application of devices made using optical components that are fabricated by the same methods as, and are similar in scale to, integrated electronic components. One of the most commonly used materials for the fabrication of integrated optic components and systems is $LiNbO_3$. The kinds of components that can be fabricated in $LiNbO_3$ include waveguides [1,2], modulators [3-7], polarization converters [8,9], and frequency converters [10,11].

This thesis is concerned with the fabrication of voltage induced optical waveguide modulators (VIOWM) in $LiNbO_3$. The voltage induced optical waveguide was first introduced by Channin in 1971 [12]. Channin's device had a serious limitation in that it needed an minimum operating voltage of 300V. Channin's work was followed by that of Soref et al. [13] which also needed such large voltages. The apparent need for such large voltages caused the voltage

induced optical waveguide to be disregarded and other devices to receive more attention. In this thesis it is shown that the voltage levels can be reduced by at least an order of magnitude.

Baumert et al. [14] fabricated and tested voltage induced optical waveguides in $KNbO_3$ (which has a larger electrooptic coefficient* than $LiNbO_3$) with on-off ratios of 12dB for 35V applied. These devices had large electrode spacings, large capacitances, and large optical field distributions. Our devices were able to achieve equally good characteristics at lower voltages and had much lower capacitances.

Savatinova et al. [15] have demonstrated an electrically induced Ti:$LiNbO_3$ strip-waveguide. In their device the optical characteristics of a planar waveguide, formed by modifying the surface layer of the $LiNbO_3$ by the in-diffusion of Ti, are changed by applying voltage to electrodes on the surface of the waveguide. Light is selectively coupled into and out of a particular mode using prism couplers. Regions of the output in which there is a change in the light intensity can then be interrogated. They report a 9V operating voltage with a possible 95% modulation. The devices studied in this thesis differ from the device of Savatinova et al. in that there is no

---

* The electrooptic coefficient is discussed in appendix A.

diffusion and that coupling is achieved by the more direct method of "butt-coupling" [16] or "end-fire-coupling" [17] which removes the need for prisms. Prisms are bulky and make for an optical system needing somewhat precise alignment. Also in our devices the optical field distributions of the guided modes can be controlled so as to be well matched to the field distributions in single mode fibers. As single mode fiber is being used more and more frequently this is an important advantage as regards coupling efficiencies and possible applications. The ability to butt-couple to our device will have further advantages as far as the size of the device and the packaging of a device with fiber pigtails attached is concerned.

Another device that has been investigated by Kawabe et al. [18] consists of a planar diffused Ti waveguide in $LiNbO_3$ in which a 420 nm high ridge has been etched. When voltage is applied to electrodes on either side of the ridge the optical characteristics of the substrate are altered and the guided wave is radiated into the bulk of the crystal. Kawabe et al. report an extinction coefficient -19dB for ±10V (a 20 volt difference) for the E^z mode on a 3 mm long device. We have been able to achieve similar results with out the need for either a Ti indiffusion or a ridge by using long devices (in long devices the coupling from the input fiber to the output fiber due to bulk modes is small). Also

where the throughput of their device seems to saturate ours continues to increase for voltage differences beyond 20V. Further problems that were encountered by Kawabe et al. included surface waveguiding and the propagation of E^y modes for which the voltages required were about 3 times as large. They did not comment on the effect of bulk mode coupling in their device.

In this thesis two types of VIOWM are studied; the first is planar and the second has a ridge. The first is easy to make but the second has added advantages. It will be shown that their performance is as good or better than the performance of the other devices of the voltage induced genre which have been discussed above. They are both strictly of the voltage induced waveguide type in that the surface of the substrate has not been modified in order that it be predisposed to the guiding of optical waves.

In the planar device (figure 1.1) two metal electrodes, separated by a narrow gap, are isolated from a single crystal $LiNbO_3$ substrate by a thin layer of SiO_2.

The second device (figure 1.2) differs from the planar in that a ridge is included between the electrodes which ideally are of the same height as the ridge.

Application of voltage to the electrodes establishes an electric field in the substrate. The substrate is a crystal

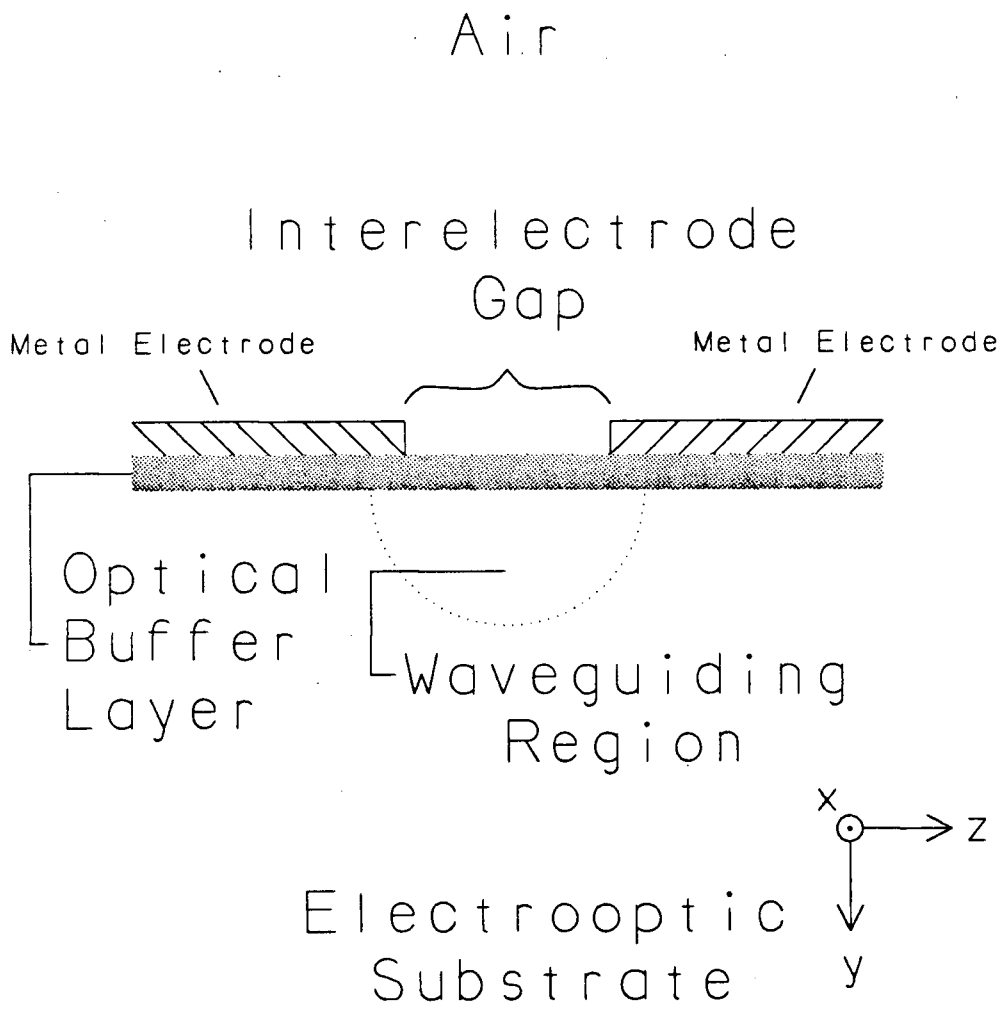

Figure 1.1: The planar VIOWM in cross section. Here light is propagating out of the page toward the reader.

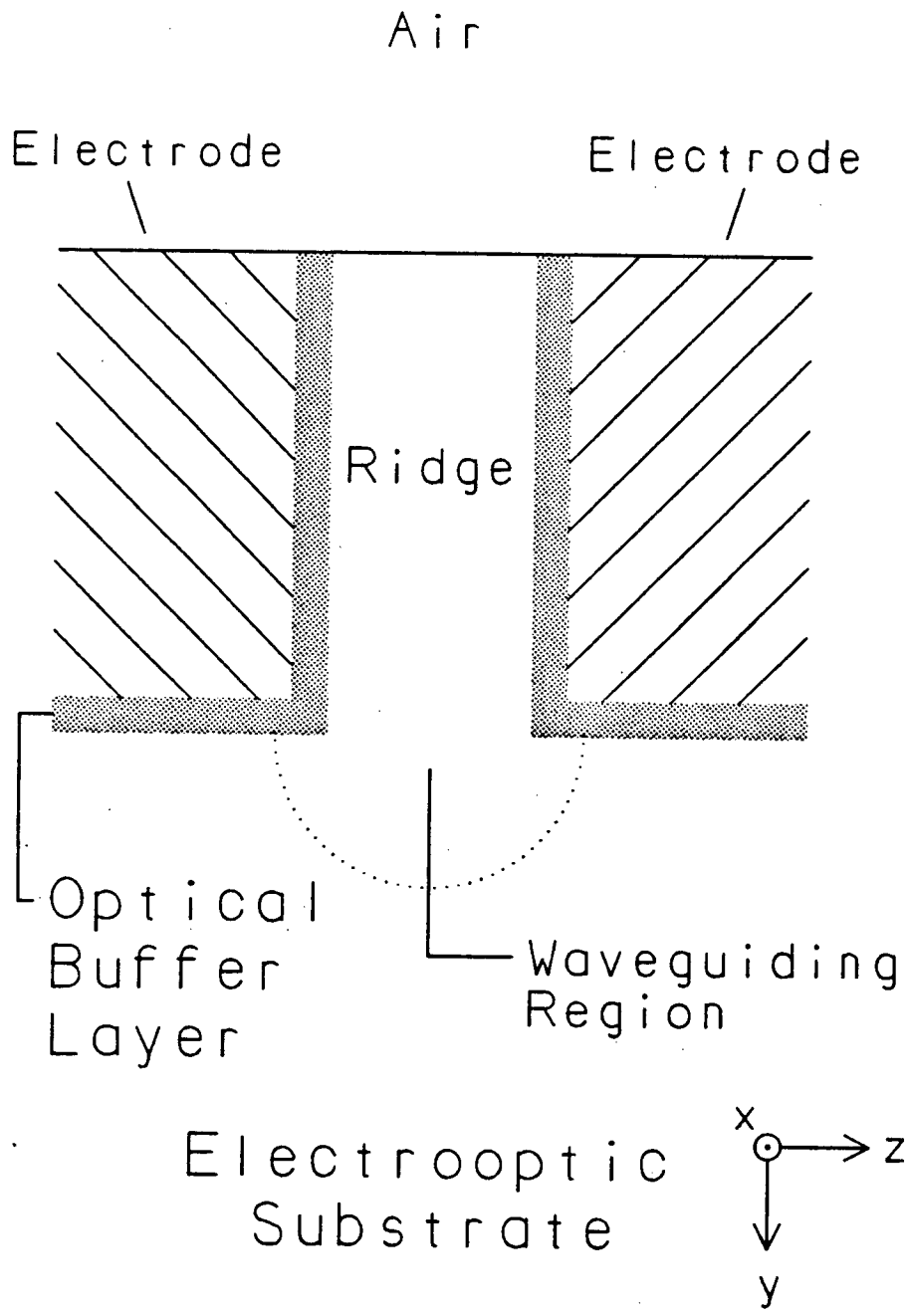

Figure 1.2: The ridge VIOWM in cross section. Here light is propagating out of the page toward the reader.

which exhibits the linear electrooptic effect.* Therefore the electric field alters the refractive indices of the substrate. The field is largest in the regions close to the electrode edges as well as in the immediate region of the interelectrode gap hence as the voltage is increased the optical wave is increasingly confined to that region.* The SiO_2 layer is included to act as an optical buffer layer isolating the optical field from the metal electrodes.

While the operation of the device is conceptually straight forward to study and design VIOWMs it was necessary to develop a method of analysis. Our method consisted of using conformal mapping techniques to calculate the refractive index distribution established in a VIOWM for a particular voltage. Then following the approach used by Marcuse for analyzing step index fibers [19], we used a variational technique to find the optical field distributions for waveguides with these refractive index distributions. In this method appropriate trial functions with variable parameters are assumed to approximate the optical field distributions. We have used Hermite-Gaussian

---

* See appendix A for a discussion of the linear electrooptic effect.

* As will be seen in section 2.2 the voltage must have the correct sign, relative to the crystal axes, for the refractive index to increase otherwise the refractive index will be decreased and light will be radiated out of that region.

functions as the trial functions. The variable parameters are determined for these functions by making use of the stationary nature of the eigenvalues of the scalar wave equation. The width parameters vary with voltage allowing one to predict the development of optical field distributions with increasing voltage.

When designing VIOWMs in $LiNbO_3$ the controllable parameters include: the substrate orientation, the wavelength of the light to be guided, the optical buffer layer material, the optical buffer layer thickness, the interelectrode gap orientation, the interelectrode gap width, the operating voltage, the ridge height, and when being used with fibers the fiber location and if possible the width parameters of the fiber mode.

One application of a VIOWM is as a voltage controlled linking waveguide between two optical fibers (figure 1.3) in which optical power is transferred from one fiber to the other via the VIOWM. In this application it is not sufficient to know how the optical field distribution in the VIOWM develops only but one must also know how the development effects the coupling of light to and from the fibers. A closed form expression for the coupling coefficient for butt-coupling between an optical fiber and a VIOWM is developed in this thesis. Thus a complete model for the study and design of VIOWMs in this application has been developed. The model allowed us to predict the modus

operandi of the VIOWM as a linking waveguide for several applications. For instance it is shown that the VIOWM can be used as a digital switch or as a linear modulator. When being used as a digital switch the change in optical power transfer can be maximized for a given voltage level or the sensitivity of the device to small variations in input voltage level may be minimized.

The theory of operation of VIOWMs was confirmed by fabricating and testing several devices. These were of both the planar and ridge types. The method of fabrication is described in chapter 3. Also arrays of V-grooves [20] were etched in silicon substrates for the alignment of optical fibers with VIOWMs in a flip-chip arrangement [21]. Their fabrication is described as well, as is the alignment technique and the method of eutectic bonding between electrodes on the V-groove substrates and on the electrodes on the VIOWMs.

Tests were made on the devices. Their voltage response was measured. The coupling coefficients between VIOWMs and optical fibers were measured. The devices were tested as digital modulators. It was shown that the output power could be modulated in a linear fashion by the applied voltage and that the coupling efficiency could be optimized for a particular voltage for a particular location of the input optical field distribution, both these phenomena were predicted by the theory. Another prediction was that a

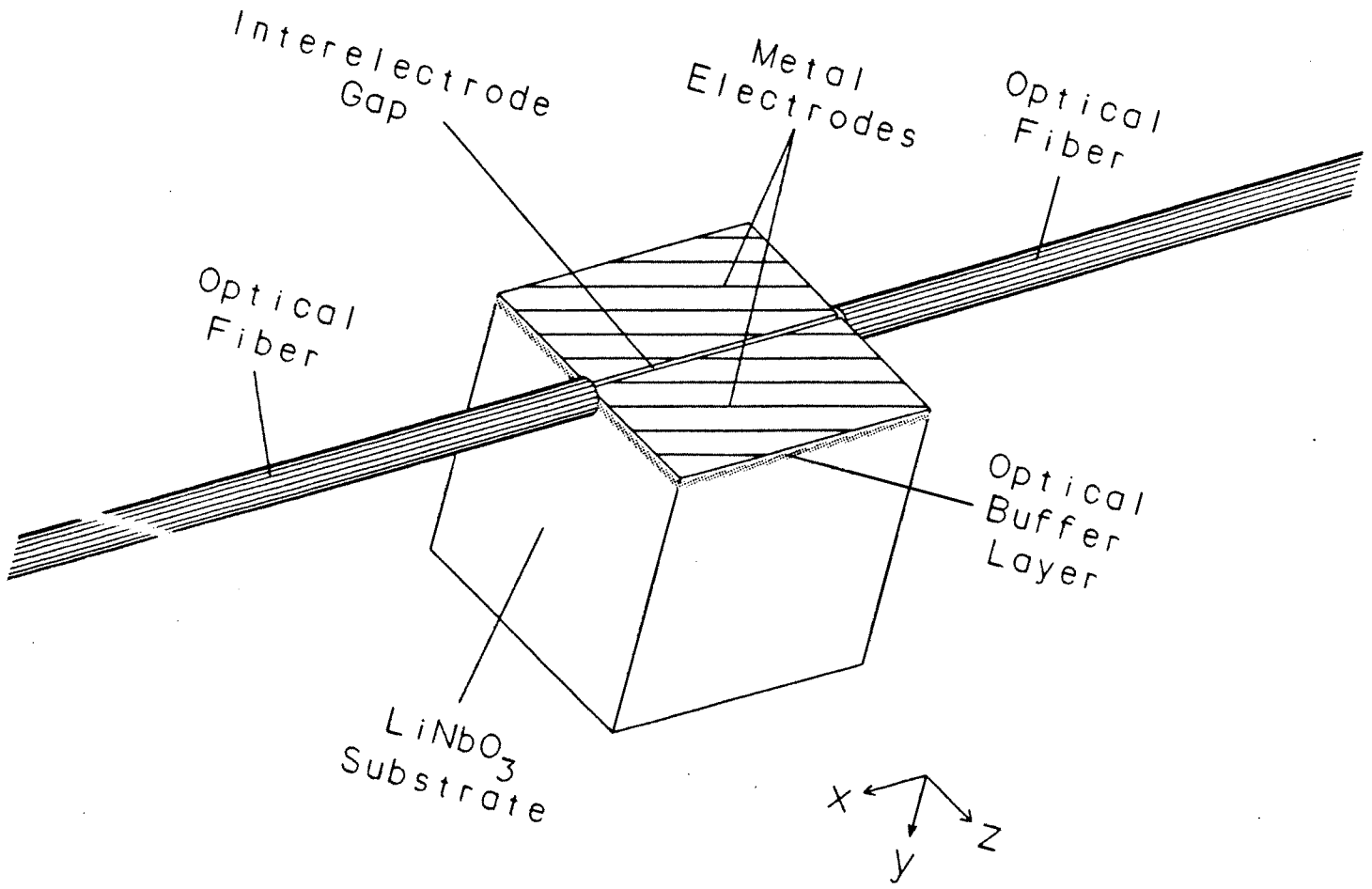

Figure 1.3: The VIOWM acting as a linking waveguide between two optical fibers.

"turn-on" voltage exists for ridge waveguides at which light rapidly becomes confined to the ridge. This effect was also experimentally confirmed. A device with an optical fiber attached, using an array of silicon V-grooves, was also fabricated and tested. This device was envisioned to be used as a front-end switch for the optical system of an optical image recorder such as the FIRE 9000 produced by the local company MacDonald Dettwiler and Associates of Richmond, British Columbia, Canada.

A d.c. decay phenomenon was observed which is believed to be due to the photorefractive effect [22]. It was found that this could be compensated for by the application of a negative "fly-back" voltage to the electrodes of the VIOWM. The application of a negative voltage was also found to be useful on short devices as it created a sort of "anti-waveguide" out of which light in bulk modes was refracted enhancing the extinction ratio of the device.

Chapter 2

THEORY

2.1 Introduction

The theory of the VIOWM is contained in five sections of this chapter entitled:

The Electrooptic Effect,
The Conformal Mappings,
The Variational Method,
The Hermite-Gaussian Approximations, and
The Coupling Coefficient.

In the section on the electrooptic effect expressions for the change in the refractive index are derived and for the rotation of the indicatrix about the X-axis* of the substrate. Both are given in terms of the applied electric

---

* In the coordinate system used here the x, y, and z-axes are coincident with the X, Y, and Z-axes of the $LiNbO_3$ substrate, respectively. They correspond to the x_1, x_2, and x_3-axes in appendix B of Nye [23] pp. 276-288, i.e., $x||x_1||a$, $y||x_2 \perp x_1$, and $z||x_3||c$. The result of this is that the x-direction becomes the direction of propagation therefore the symbol, β, will designate the propagation constant in the x-direction.

field. It is assumed that Y-cut $LiNbO_3$ is the electrooptic substrate. This corresponds to the orientation that was used in the fabrication and testing of the experimental devices described in the following chapters. The applied electric field is assumed to have Y and Z components only. Again this corresponds to the case in our experiments.

The electric field distribution inside the electrooptic substrate needs to be analyzed in order to predict the behavior of the devices at various voltages. In the conformal mappings section both the planar and ridge device types are modeled and the electric field distributions established in them are derived.

In the variational method section a technique for approximating the electromagnetic field distribution of an optical wave propagating in a voltage induced optical waveguide, using the calculus of variations, is presented.

In the section on the Hermite-Gaussian approximation the reasons for choosing these trial functions are presented. Also included in this section is a discussion justifying the use of a Gaussian approximation for the optical field distribution in a single-mode optical fiber.

In the coupling coefficient section a closed form analytic expression for the coupling coefficient is derived for coupling between an optical fiber and a voltage induced optical waveguide. This expression is derived using the approximate optical field distributions assumed for both the

optical fiber and the voltage induced optical waveguide. It is assumed that the ends of the two waveguides can be polished to such a high degree that they can be brought into intimate contact and that power is "butt-coupled" from one waveguide to the other.

2.2 The Electrooptic Effect

In this section we will obtain the relationship between the change in the refractive index and the applied electric field. Both the magnitudes of the principal axes and the orientation of the indicatrix are affected. The change in orientation is shown to be small for the fields used and can be ignored. However the change in the magnitude of the principal axes contains a quadratic term that may be as much as 10% of the change due to the linear term, for the fields used, and is retained. The mathematical formalism for the electrooptic effect is included in appendix A.

The largest linear electrooptic coefficient of $LiNbO_3$ is r_{33} [24] and it is clearly desirable that advantage be taken of it. Y-cut $LiNbO_3$ was chosen to take advantage of r_{33}. The devices were fabricated so that the interelectrode gap runs parallel to the X-axis. This ensured that the distribution of the electric field component parallel to the Z-axis of the substrate, E_z, was symmetric with respect to

the XY-plane. The distribution of the electric field component parallel to the Y-axis of the substrate, E_y, was anti-symmetric to the XY-plane. In what follows an equation giving the change in the extraordinary refractive index, Δn_e, in terms of the two electric field components E_y and E_z is derived.

The general equation relating the change in the optical indicatrix to an electric field is given in appendix A. When a field is applied to an electrooptic crystal a change is incurred in the impermeability. One can construct the new impermeability tensor in terms of the electrooptic coefficients and the electric field components. When the substrate is $LiNbO_3$ and the electric field is entirely in the yz-plane then $B_4 = r_{42}E_y$ is the only nonzero off-diagonal element. B_4 will have an effect only in the yz-plane and the distortion in the indicatrix, in this plane, can be found using the Mohr Circle*. The distortion will, in general, consist of changes in both the magnitudes and orientations of the principal axes. The change in orientation can be expressed as an angle of rotation, θ, with respect to the original axes. Following the procedure in Nye** one can obtain

---

* Nye [23] pp. 43-47.

** Ibid.

$$\tan(2\theta) = \frac{2r_{42}E_y}{n_e^{-2} - n_o^{-2} + r_{33}E_z - r_{22}E_y - r_{23}E_z} \qquad (2.1)$$

which is derived in appendix A. Since the electrooptic coefficients are small the last three terms in the denominator can be ignored. We can approximate the angle of rotation of the indicatrix in the YZ-plane by

$$\theta \approx \frac{r_{42}E_y}{n_e^{-2} - n_o^{-2}} .$$

The highest values for E_y were in the regions near the electrode edges for the thin electrodes and near the corners of the thick electrodes. The peak values of E_y are on the order of 10^6 V/m and will cause a rotation of less than 1°. Therefore the rotation is ignored.

All the guided optical modes of this device will propagate in the x-direction. However they will not have the same propagation constant. This is due to the large anistropy of $LiNbO_3$. The guided modes can be divided into two basic types TE and TM like modes. A TE like mode is one in which the electric field of the mode is predominantly polarized parallel to the Z-axis of the substrate and a TM like mode is one in which the electric field is predominantly polarized in the XY-plane. These modes are analogous to the E^x_{pq} and E^y_{pq} modes of rectangular channel

waveguides described by Marcatili [25] (where the superscripts x and y refer to the coordinate system used by Marcatili). Due to the difference in the electrooptic coefficients $r_{33} = 30.8\times10^{-12}$m/V and $r_{23} = 8.6\times10^{-12}$m/V [24] the change in the refractive index "seen" by a TE like mode will be approximately 3 times that seen by a TM like mode. The lowest order TE like mode will be the most important of the modes propagating in the VIOWM for the voltages used. Therefore it will be assumed throughout this thesis that the mode being coupled into, or out of, and propagating in the VIOWM is a TE like mode. Polarization-preserving fiber could be used to ensure that this is the case.

For TE like modes the waveguide created by the application of voltage to the electrodes of a VIOWM involves the extraordinary refractive index, n_e, of $LiNbO_3$. It is the change in the corresponding principal axis of the optical indicatrix due to the applied electric field that causes the waveguide to be created. The change in the principal axis consists of both a change in magnitude and a change in orientation. However, since the rotation is small we have ignored it and have treated the change as a change in the magnitude of extraordinary refractive index only. The change $\Delta n_e(y,z)$ is given by

$$\Delta n_e(y,z) \approx -\frac{n_e^3 r_{33} E_z(y,z)}{2} - \frac{n_e^3 \{r_{42} E_y(y,z)\}^2}{2(n_e^{-2} - n_o^{-2})} \qquad (2.2)$$

which is also derived in appendix A. The first term on the right hand side of equation 2.2 is the change in the z-direction alone and the second term is the added change in the magnitude of the principal axis. We have retained the second term because it may be as much as 10% of the first term in the regions near the electrode edges or corners even though the rotation is small.

2.3 The Conformal Mappings

The conformal mappings that were used to find the applied field distributions, $E_z(y,z)$ and $E_y(y,z)$, are discussed in the following subsections for both the planar and ridge devices.

First, however, we must derive the Laplacian for the orientation of the substrate used by a transformation of variables. This is necessary due to the anisotropy of $LiNbO_3$. The same transformation is good for both the planar and ridge devices.

Poisson's equation with respect to the YZ-plane of $LiNbO_3$ is given by

$$\nabla \cdot D = \epsilon_y \frac{\partial^2 V}{\partial y^2} + \epsilon_z \frac{\partial^2 V}{\partial z^2} = 0$$

which by the transformation of variables

$$y' = \left(\frac{\epsilon_z}{\epsilon_y} \right)^{1/2} y \qquad (2.3a)$$

and

$$z' = z \ , \qquad (2.3b)$$

where ϵ_y and ϵ_z are the Y and Z-components (ϵ_a and ϵ_c) of the diagonalized permittivity tensor respectively, can be written as the Laplacian

$$\frac{\partial^2 V}{\partial y'^2} + \frac{\partial^2 V}{\partial z'^2} = 0 \ . \qquad (2.4)$$

2.3.1 The Planar Device

2.3.1.1 The Device Structure

The planar VIOWM (figure 2.1) consists of an electrooptic substrate with two thin metal electrodes, separated by a narrow interelectrode gap, deposited on one of its faces. A thin optical buffer layer is included between the substrate and the electrodes to reduce transmission losses due to interactions between the optical field and the electrodes.

The metal electrodes and the optical buffer layer are thin with respect to the interelectrode gap width and their

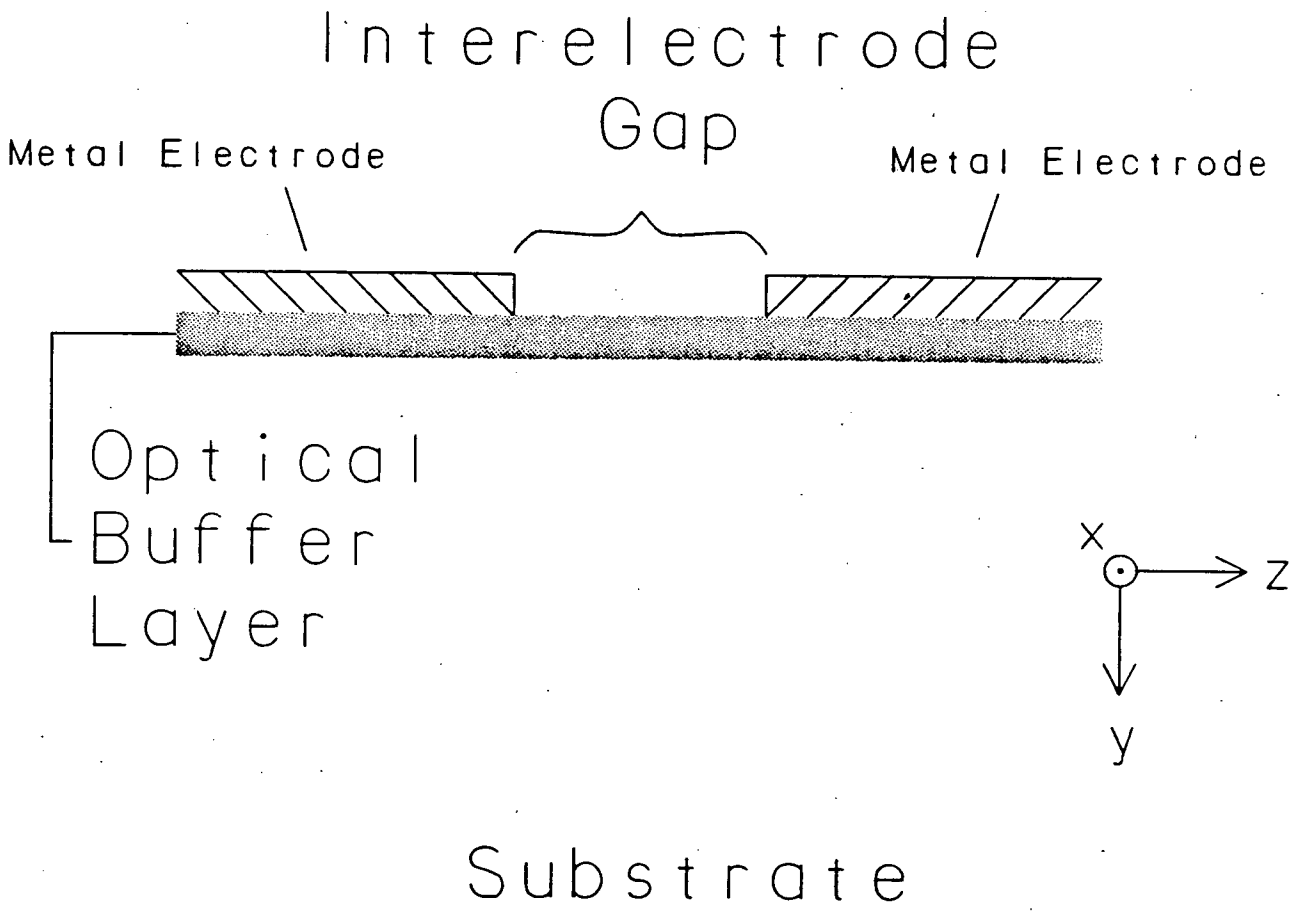

Figure 2.1: The planar VIOWM structure.

thickness may be ignored in modeling the device. The actual structure was replaced by the structure shown in figure 2.2 in which two coplanar electrodes of infinitesimal thickness are situated directly atop the substrate. This structure may in turn be analyzed, and the electric field distribution in the substrate calculated, by substituting one in which the electrodes are embedded in an anisotropic substrate as in figure 2.3. This second substitution will give exact results for the anisotropic half of the structure as it has equivalent boundary conditions to those of the anisotropic region depicted in figure 2.2. The boundary condition for the normal component of the applied field in the interelectrode gap in the plane of the electrodes is

$$E_y\Big|_{y=0} = 0 \ .$$

for both structures.

2.3.1.2 The Electric Field Distributions

The conformal mapping consists of mapping the strip $0 < u < \pi$ in the W-plane to the region exterior to a hyperbola, with its foci at $\pm g/2$, in the S-plane. This mapping is achieved by the mapping $S = -(g/2)\cos(W)$.* Figure 2.4

---

* Ramo et al. [26] section 7.6 pp. 331-340.

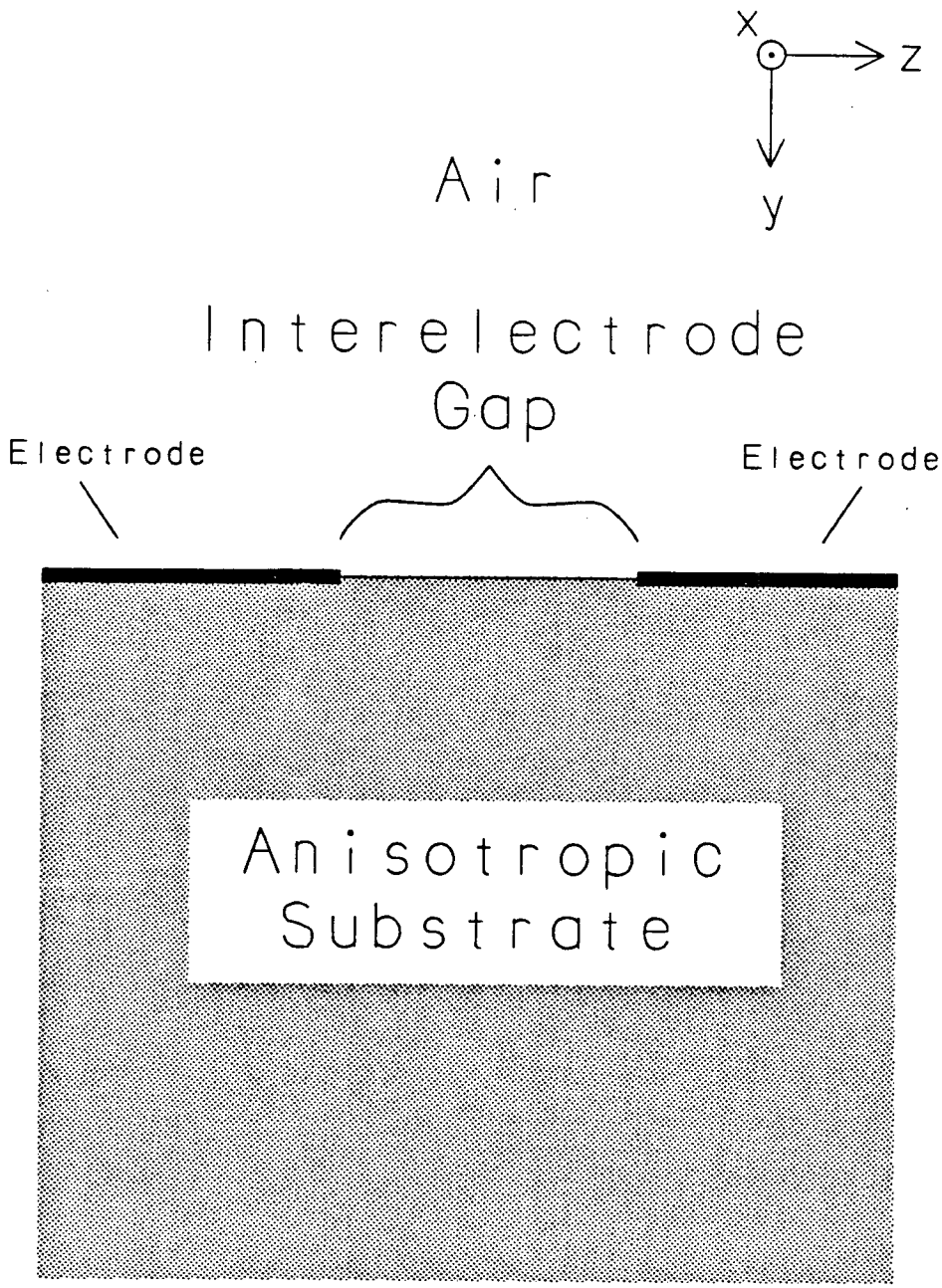

Figure 2.2: An intermediate model of the planar VIOWM structure.

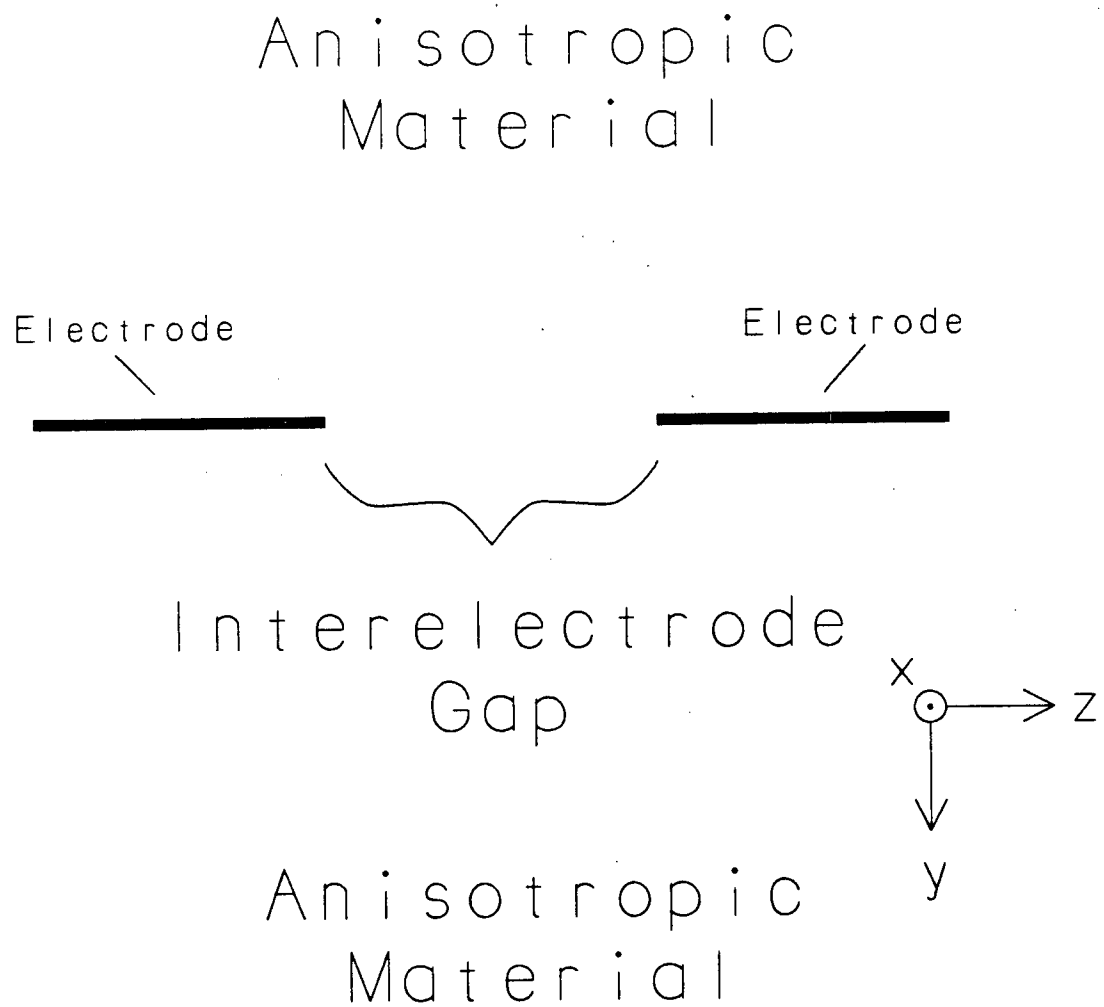

Figure 2.3: The model used to analyze the planar VIOWM structure.

depicts the W and S-planes. The current problem is concerned with the limiting case in which the foci are coincident with the ends of the electrodes resulting in the electrodes being represented by the lines $|\sigma| \geq g/2$.

If the lines $u = 0$ and $u = \pi$ are assumed to be electrodes at ground and V_o volts respectively then the potential function in the strip is given by

$$V(u,v) = \frac{V_o}{\pi} u \ .$$

The electric field components in the S-plane, E_σ and E_ω, are given in terms of the potential function by

$$E_\sigma = - \frac{\partial V(u,v)}{\partial \sigma} = - \frac{V_o \partial u}{\pi \partial \sigma}$$

and

$$E_\omega = - \frac{\partial V(u,v)}{\partial \omega} = - \frac{V_o \partial u}{\pi \partial \omega} = \frac{V_o \partial v}{\pi \partial \sigma}$$

where the Cauchy-Riemann condition $\partial u/\partial \omega = - \partial v/\partial \sigma$ has been used. Here $\partial u/\partial \sigma$ and $\partial v/\partial \sigma$, are the real and imaginary parts of dW/dS,

$$\frac{dW}{dS} = \frac{\partial u}{\partial \sigma} + i \frac{\partial v}{\partial \sigma} \ ,$$

respectively.

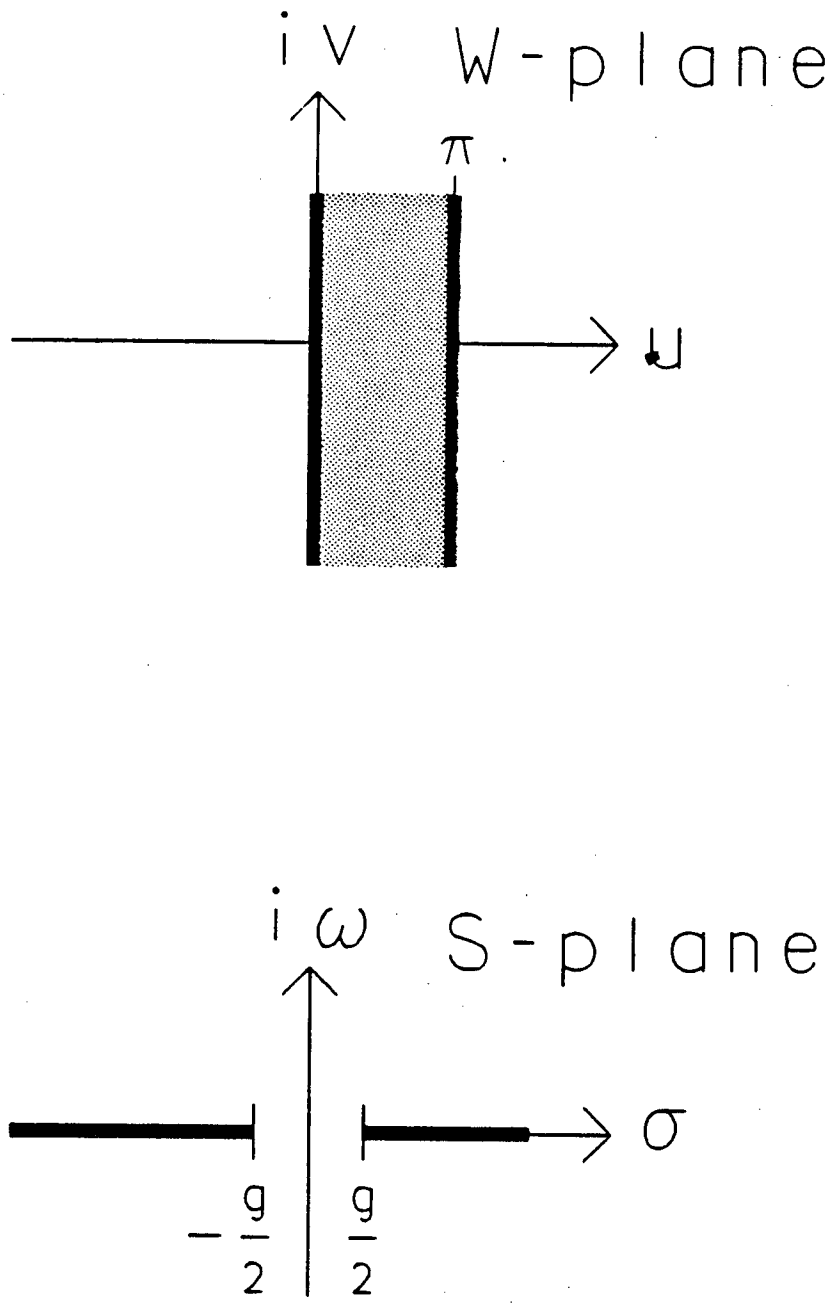

Figure 2.4: The W and S-planes.

The inverse mapping of $S = -(g/2)\cos(W)$, giving W as a function of S, is $W = \pi - \cos^{-1}(2S/g)$. Therefore the derivative, dW/dS, equals $\{(g/2)^2 - S^2\}^{-1/2}$ or

$$\frac{dW}{dS} = \frac{1}{\left\{\left(\frac{g}{2}\right)^2 - \sigma^2 + \omega^2 - i2\sigma\omega\right\}^{1/2}} .$$

which after rearrangement gives

$$E_\sigma = -\frac{V_o \cos\left\{\frac{1}{2}\tan^{-1}\left(\frac{2\sigma\omega}{(g/2)^2 - \sigma^2 + \omega^2}\right)\right\}}{\pi\left\{\left[\left(\frac{g}{2}\right)^2 - \sigma^2 + \omega^2\right]^2 + 4\sigma^2\omega^2\right\}^{1/4}} \qquad (2.5a)$$

and

$$E_\omega = \frac{V_o \sin\left\{\frac{1}{2}\tan^{-1}\left(\frac{2\sigma\omega}{(g/2)^2 - \sigma^2 + \omega^2}\right)\right\}}{\pi\left\{\left[\left(\frac{g}{2}\right)^2 - \sigma^2 + \omega^2\right]^2 + 4\sigma^2\omega^2\right\}^{1/4}} \qquad (2.5b)$$

Obviously the positive σ-axis should correspond to the positive z′-axis. Therefore if we wish the positive ω-axis to correspond to the positive y′-axis this fixes the positive x-axis to be oriented so as to point into the paper

in figure 2.2. Finally on substitution of equations 2.3a and b into 2.5a and b one obtains

$$E_\sigma = - \frac{V_o \cos\left\{ \frac{1}{2} - \tan^{-1}\left(\frac{2z(\varepsilon_z/\varepsilon_y)^{1/2} y}{(g/2)^2 - z^2 + (\varepsilon_z/\varepsilon_y) y^2} \right) \right\}}{\pi \left\{ \left[\left(\frac{g}{2} \right)^2 - z^2 + \left(\frac{\varepsilon_z}{\varepsilon_y} \right) y^2 \right]^2 + 4z^2 \left(\frac{\varepsilon_z}{\varepsilon_y} \right) y^2 \right\}^{1/4}} \qquad (2.6a)$$

and

$$E_\omega = \frac{V_o \sin\left\{ \frac{1}{2} - \tan^{-1}\left(\frac{2z(\varepsilon_z/\varepsilon_y)^{1/2} y}{(g/2)^2 - z^2 + (\varepsilon_z/\varepsilon_y) y^2} \right) \right\}}{\pi \left\{ \left[\left(\frac{g}{2} \right)^2 - z^2 + \left(\frac{\varepsilon_z}{\varepsilon_y} \right) y^2 \right]^2 + 4z^2 \left(\frac{\varepsilon_z}{\varepsilon_y} \right) y^2 \right\}^{1/4}} . \qquad (2.6b)$$

Sputtered silicon dioxide has a much smaller refractive index than $LiNbO_3$ (approximately 1.46 as compared to 2.20 for n_e at λ_o = 633nm). For us it was a good choice as the optical buffer layer material as it was available in the solid state laboratory here at U.B.C. and is easy to work with. Using it we can approximate the decay constant for the evanescent field, normal to the surface by $\{(2\pi/\lambda_o)(2.20^2 - 1.46^2)^{1/2}\}$ which is about 16/μm this means that the field decays to about 4% of its value at the surface in 2000Å. An even better result is obtained at λ_o =

442nm. However, at low frequencies the dielectric constant of SiO_2 is significantly lower than either $K_y = \varepsilon_y/\varepsilon_o$ or $K_z = \varepsilon_z/\varepsilon_o$ for the $LiNbO_3$ (approximately 4 as compared to 43 and 28 respectively). This difference in the relative permittivities of the two materials affects the electric field distribution in the device. It reduces the applied field in the high permittivity region as compared to the case where the electrodes are placed directly in contact with the $LiNbO_3$. Therefore it was important that the buffer layer be kept thin so that the effect was small. In the calculations made for this thesis it was assumed that the buffer layer thickness was 5% of the interelectrode gap width and was treated as a mere offset from the electrodes in calculating the electric field distributions. In other words the electric field distributions were calculated as though the electrodes were directly in contact with the substrate then the surface of the induced waveguide was taken to be at a distance of 5% of the gap width away from the electrodes and into the substrate. The applied field distributions $E_y(y,z)$ and $E_z(y,z)$ are plotted in figures 2.5 and 2.6 respectively. In both of these plots it is assumed that the voltage, V, applied across the electrodes is negative* so that $E_z(y,z)$ is positive. Although the y-

---

* The IRE Standards on Piezoelectric Crystals is used for the sign convention here. See Lines and Glass [27] p. 147.

component of the applied field is seen to be of the same order of magnitude as the z-component in the regions near the electrode edges the term $\{r_{42}E_y(y,z)\}^2$ in equation 2.2 is very small for the field strengths used.

2.3.2 The Ridge Device

2.3.2.1 The Device Structure

While the planar VIOWM works to create a linking waveguide between the input and the output faces of the device it is obvious, by inspecting the structure shown in figure 2.2, that it does not make the best use of the large field in the interelectrode gap region. In order to make the device more efficient a ridge of the electrooptic medium can be included between thick electrodes as in figure 2.7.

If the ridge is high enough the normal component of the applied field at the surface, E_y, will be relatively small and the tangential component, E_z, will be essentially uniform. It can be seen that E_y will be small by comparing the normal component of the field on both sides of the boundary. If E_{ya} is the normal component of the field in air at the boundary and E_{ys} is that in the substrate then $E_{ys} = (\varepsilon_{air}/\varepsilon_{substrate})E_{ya}$ or $E_{ys} \approx 0.02E_{ya}$. It follows then

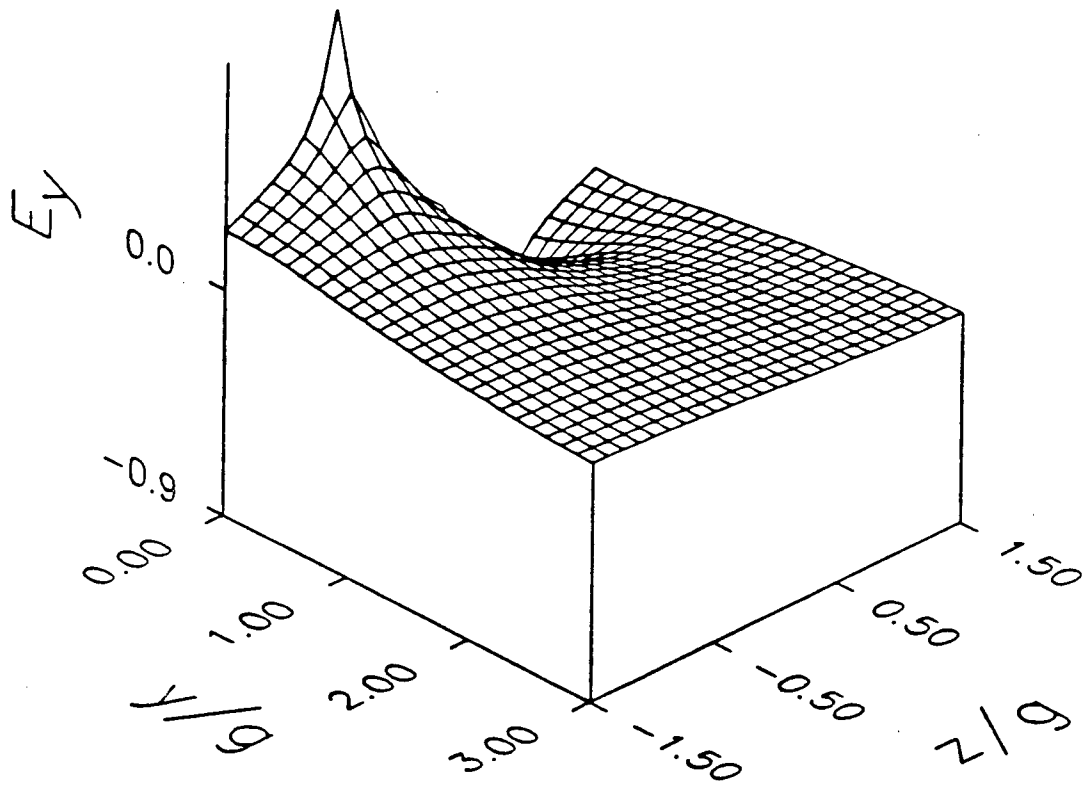

Figure 2.5: A plot of $E_y(y,z)$ for the planar VIOWM.

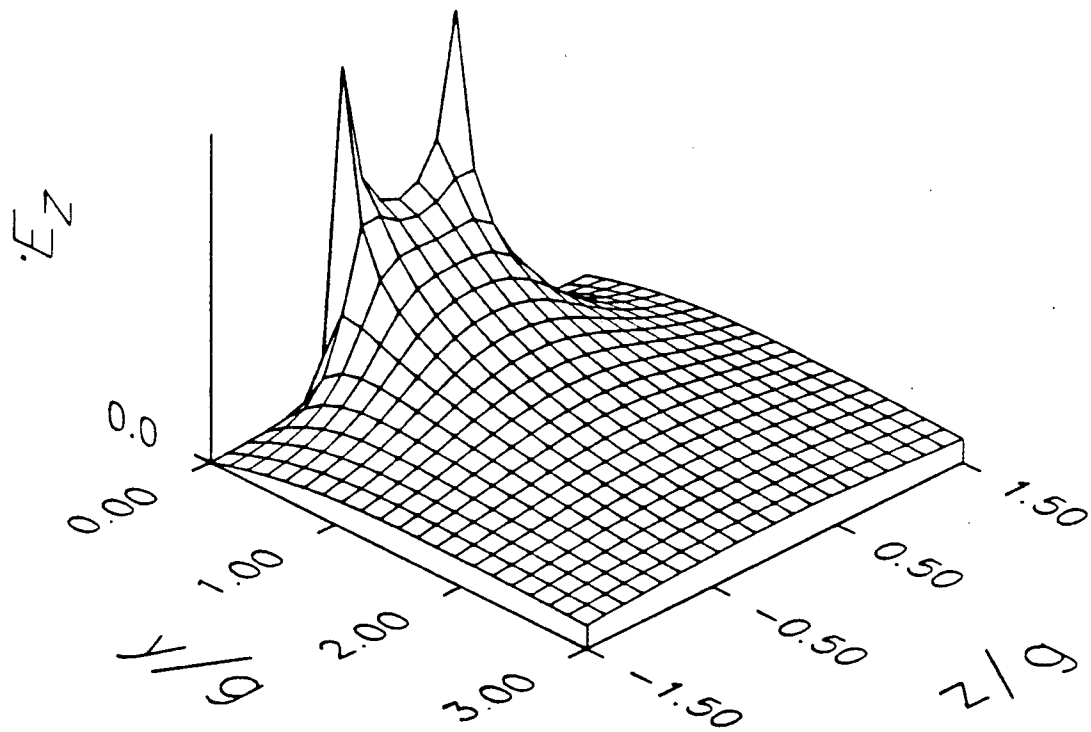

Figure 2.6: A plot of $E_z(y,z)$ for the planar VIOWM.

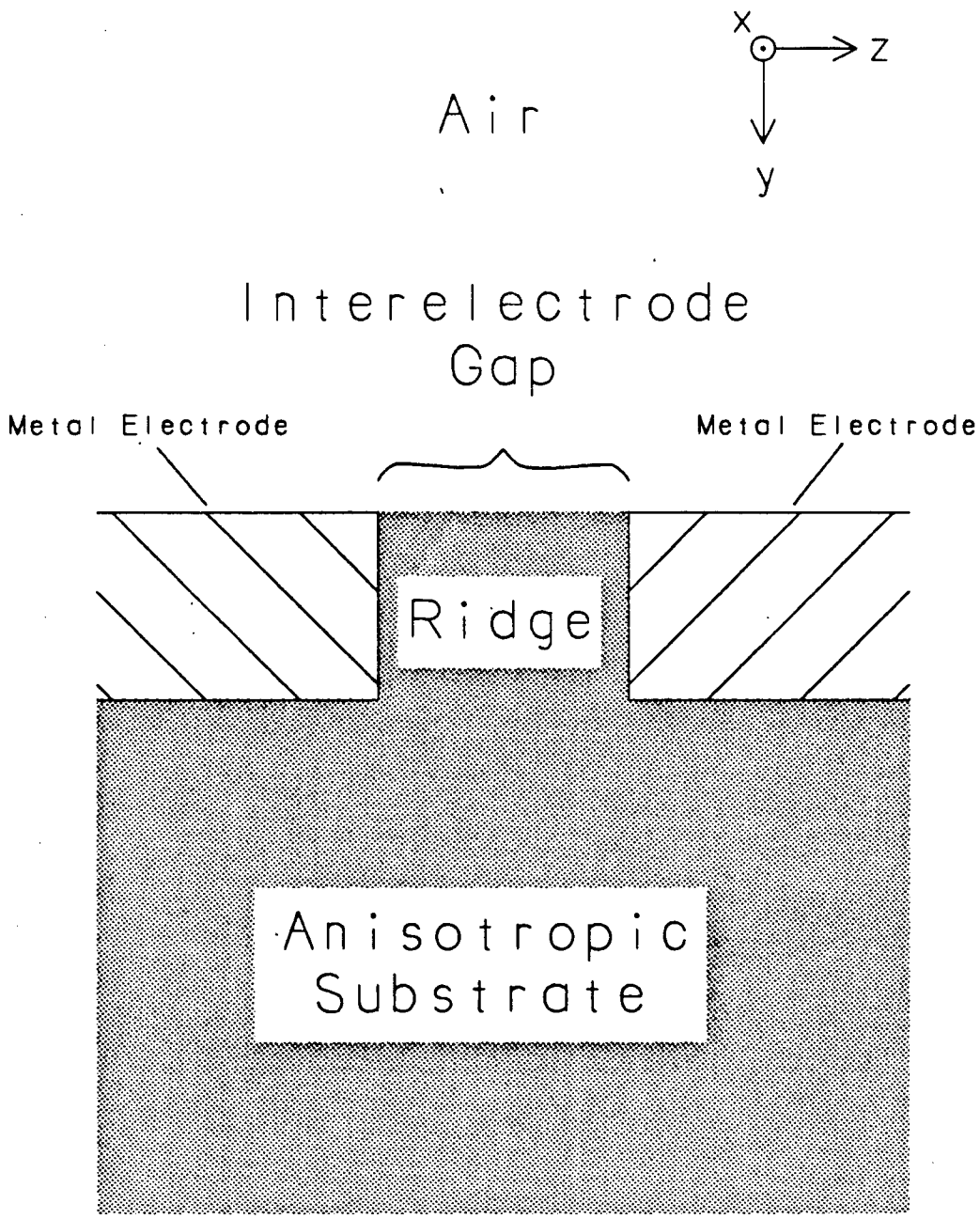

Figure 2.7: The ridge VIOWM structure.

that if the ridge is high enough* that we can approximate the actual structure by that shown in figure 2.8.

The structure depicted in figure 2.8 is similar to that commonly used for calculating the fringing field in a parallel plate capacitor [28] with the difference that the upper electrode makes a 90° angle rather than folding back on itself. In the case of the parallel plate capacitor the fringing effects quickly disappear as one moves away from the edge, into the capacitor, and the field becomes uniform and normal to the electrodes. It is one of the goals of this section to show that this is also the case for the structure of figure 2.8.

2.3.2.2 The Electric Field Distributions

In order to find the applied field distributions in the structure under analysis it is necessary to do two mappings. First the strip $0 < \eta < \pi$ in the ζ-plane, figure 2.9a, is mapped to the upper half plane of the intermediate W-plane, figure 2.9b, and second the upper half plane of the W-plane is mapped to the unshaded region of the S-plane, figure 2.9c. It is sufficient to analyze the structure shown in

---

* High enough being when $E_{ys} \approx 0$.

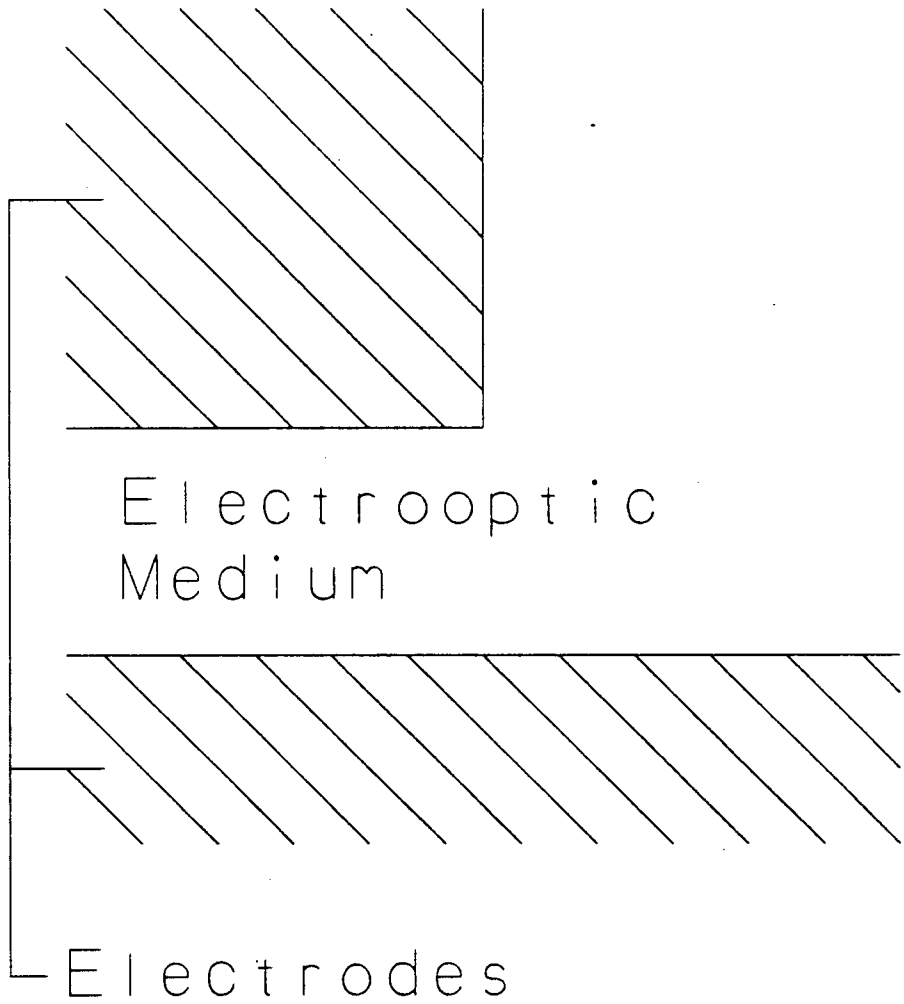

Figure 2.8: The model used to analyze the ridge waveguide VIOWM structure.

figure 2.9c rather than that shown in figure 2.8 due to the symmetry of the two structures.

The mapping used to map the ζ-plane to the W-plane is $W = e^{\zeta}$ and a Schwartz-Christoffel transform is used to map the W-plane to the S-plane. The Schwartz-Christoffel transform is found by integrating the derivative

$$\frac{dS}{dW} = \frac{(W + 1)^{1/2}}{W}$$

which gives

$$S = K\left\{ 2(W+1)^{1/2} + \ln\left[\frac{(W+1)^{1/2} - 1}{(W+1)^{1/2} + 1} \right] \right\} + C$$

$$= K\left\{ 2(u+1+iv)^{1/2} + \ln\left[\frac{(u+1+iv)^{1/2} - 1}{(u+1+iv)^{1/2} + 1} \right] \right\} + C \,. \qquad (2.7)$$

The complex constants, K and C, are evaluated by first letting $u \rightarrow -1$ on the line $v = 0$, which maps to the point $ig/2$. By doing this equation 2.7 becomes

$$\frac{ig}{2} = (K_1 + iK_2)\ln(-1) + (C_1 + iC_2) = iK_1\pi - K_2\pi + C_1 + iC_2$$

equating the real and imaginary parts of which gives

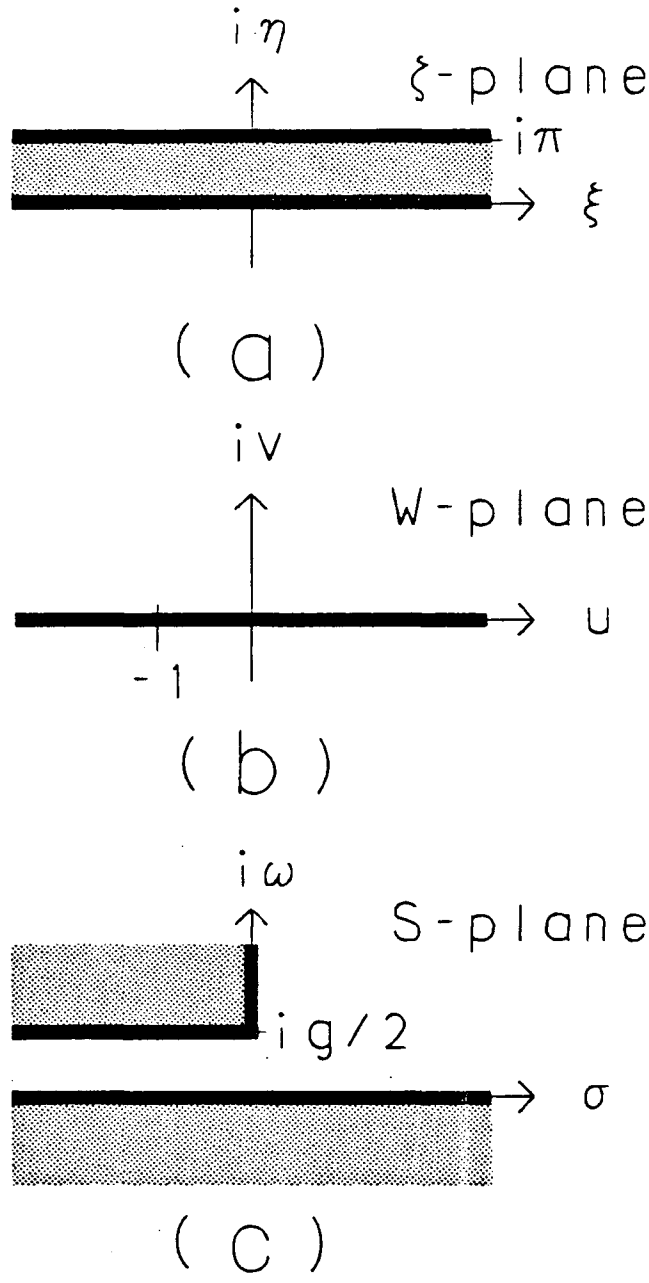

Figure 2.9: The (a) ζ, (b) W, and (c) S-planes.

$$K_1 = \frac{g}{2\pi} - C_2$$

and

$$K_2 = \frac{C_1}{\pi}$$

and by letting $u \rightarrow 0^+$ on $v = 0$, which maps to $S = -\infty$, equation 2.7 becomes

$$-\infty = (K_1 + iK_2)(2 + \ln(0)) + (C_1 + iC_2)$$

the imaginary part of which is

$$0 = K_2(2 - \infty) + C_2$$

which implies that K_2 must be equal to zero and therefore so must C_1 and C_2 so that one obtains

$$K = \frac{g}{2\pi}$$

and

$$C = 0 .$$

As it turns out the term $(u + 1 + iv)^{1/2}$ appears continually through out the solutions for the applied electric field distributions. Therefore we will first find an expression for it in the form $Me^{i\theta}$. This gives

$$M = \{(u + 1)^2 + v^2\}^{1/4}$$

and

$$\theta = \frac{1}{2} \tan^{-1}\left(\frac{v}{u + 1} \right) .$$

Rewriting equation 2.7 one obtains

$$S = \frac{g}{2\pi} \left\{ 2M\cos(\theta) + \frac{1}{2}\left[\ln(M^2 - 2M\cos(\theta) + 1) - \ln(M^2 + 2M\cos(\theta) + 1) \right] \right.$$

$$\left. + i \left[2M\sin(\theta) + \tan^{-1}\left(\frac{M\cos(\theta)}{M\cos(\theta) - 1} \right) - \tan^{-1}\left(\frac{M\cos(\theta)}{M\cos(\theta) + 1} \right) \right] \right\}$$

or

$$\sigma = \frac{g}{2\pi} \left\{ 2M\cos(\theta) + \frac{1}{2}\left[\ln(M^2 - 2M\cos(\theta) + 1) - \ln(M^2 + 2M\cos(\theta) + 1) \right] \right\} \quad (2.9a)$$

and

$$\omega = \frac{g}{2\pi} \left[2M\sin(\theta) + \tan^{-1}\left(\frac{M\cos(\theta)}{M\cos(\theta) - 1} \right) - \tan^{-1}\left(\frac{M\cos(\theta)}{M\cos(\theta) + 1} \right) \right] . \quad (2.9b)$$

Equations 2.9a and b give the coordinates, σ and ω, in the S-plane in terms of the coordinates, u and v, in the W-plane. In the next paragraph expressions for the electric field components, E_σ and E_ω, in the S-plane in terms of the W-plane coordinates, u and v will be derived.

It is convenient to consider that one of the electrodes is held at zero volts with V_o volts applied to the other electrode. It is possible to use the symmetry of the electrode configuration to see that if the model of figure 2.8 is used to analyze the electrode configuration and if it is assumed that the upper electrode is at $+V_o$ volts then the lower electrode must be at $+V_o/2$ volts. In the ζ-plane this situation corresponds to the ξ-axis being at $+V_o/2$ volts and the line $\eta = \pi$ being at $+V_o$ volts. The potential function in the strip between the ξ-axis and the line $\eta = \pi$ will be denoted, $V(\xi,\eta)$, and is given by

$$V(\xi,\eta) = \frac{V_o}{2\pi}\eta \ .$$

the electric field components are then given by

$$E_\sigma = -\frac{\partial V(\xi,\eta)}{\partial\sigma} = -\frac{V_o\partial\eta}{2\pi\partial\sigma}$$

and

$$E_\omega = -\frac{\partial V(\xi,\eta)}{\partial\omega} = -\frac{V_o\partial\eta}{2\pi\partial\omega} = -\frac{V_o\partial\xi}{2\pi\partial\sigma}$$

where the Cauchy-Riemann condition $\partial\eta/\partial\omega = \partial\xi/\partial\sigma$ has been used. The partial derivatives $\partial\xi/\partial\sigma$ and $\partial\eta/\partial\sigma$, are the real and imaginary parts of the derivative $d\zeta/dS$,

$$\frac{d\zeta}{dS} = \frac{\partial \xi}{\partial \sigma} + i \frac{\partial \eta}{\partial \sigma} ,$$

respectively. Thus the relations

$$E_\sigma = - \frac{V_o}{2\pi} \mathrm{Im} \left[\frac{d\zeta}{dS} \right]$$

and

$$E_\omega = - \frac{V_o}{2\pi} \mathrm{Re} \left[\frac{d\zeta}{dS} \right]$$

are obtained. The derivative $d\zeta/dS$ is given by

$$\frac{d\zeta}{dS} = \frac{d\zeta}{dW} \frac{dW}{dS} = \frac{d \ln(W)}{dW} \left[\frac{dS}{dW} \right]^{-1} = \frac{1}{W} \frac{W}{(W+1)^{1/2}} = (W+1)^{-1/2} = M^{-1} e^{-i\theta}$$

which gives

$$E_\sigma = \frac{V_o}{2\pi M} \sin(\theta)$$

and

$$E_\omega = - \frac{V_o}{2\pi M} \cos(\theta) \quad .$$

From figures 2.8 and 2.9c it is obvious that the σ-axis will correspond to the y'-axis of the device and that the ω-axis will correspond to the z'-axis. Therefore if we wish

to find the electric field in the yz-plane, using the above method, the transformations of the equations 2.3a and b must be applied after the conformal mapping.

Figures 2.10 and 2.11 show the distributions of $E_y(y,z)$ and $E_z(y,z)$ in the substrate. An offset from the electrodes of 5% of the gap width has been assumed to account for the optical buffer layer. Again, as in section 2.3.1.2, it is assumed that the voltage applied across the electrodes is negative i.e. V_o is negative. Although the y-component of the applied field is of the same order of magnitude as the z-component in the regions around the corner in the electrode the square of the product $r_{42}E_y$, in equation 2.2, is very small for the field strengths used.

By inspection of figures 2.10 and 2.11 it is apparent that for ridge heights of g/2 or greater the y-component of the applied field is much smaller than the z-component. Therefore this model of the ridge VIOWM can be used for ridges g/2 high or higher.

2.4 The Variational Method

In order to exactly determine the distribution of the optical field of an optical waveguide with a refractive index distribution that varies in two dimensions it is necessary to be able first to construct the appropriate wave

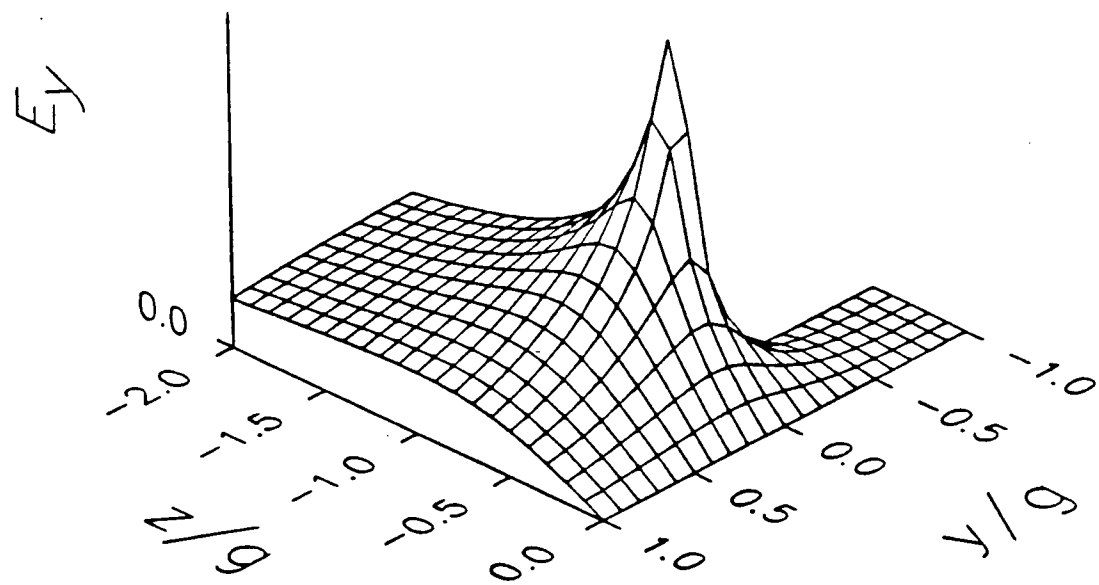

Figure 2.10: A plot of $E_y(y,z)$ for the ridge VIOWM. Here the plot has been cut along the line $z = 0$ showing the field for $z \leq 0$ only.

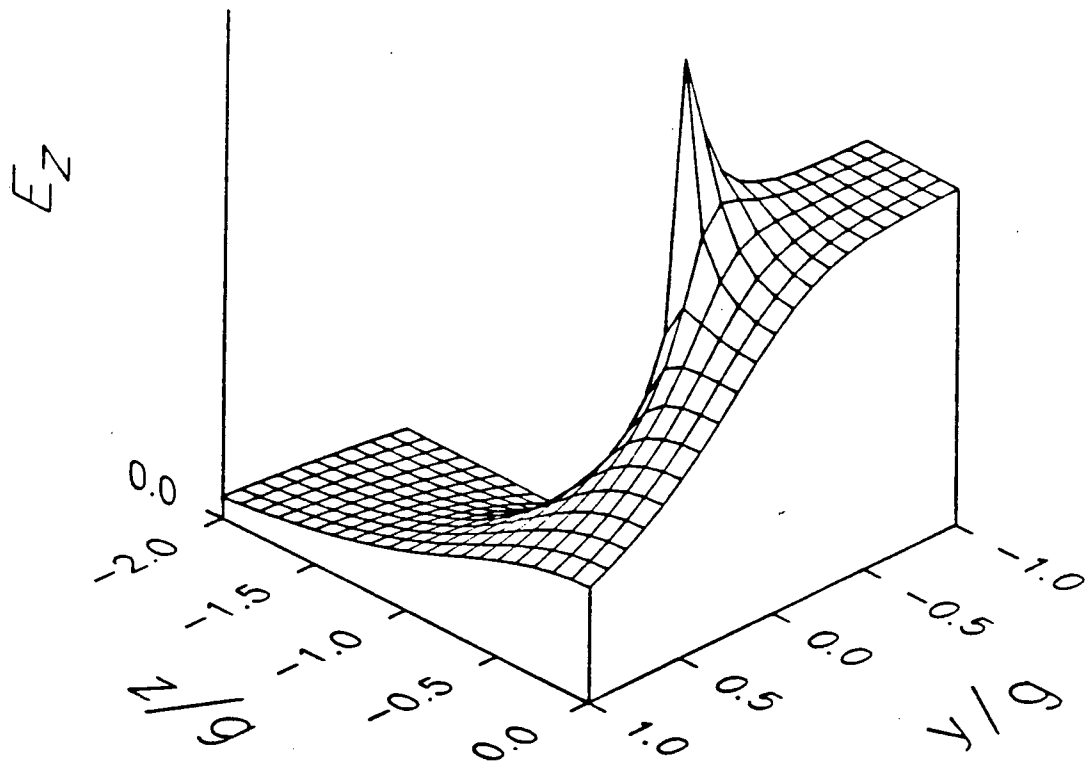

Figure 2.11: A plot of $E_z(y,z)$ for the ridge VIOWM. Here the plot has been cut along the line $z = 0$ showing the field for $z \leq 0$ only.

equation and second to solve it exactly for the optical field distribution. Indeed there exist certain refractive index distributions for which an exact approach is possible [29-31]. It is, however, far more common that while a solution obviously exists, as is evidenced by the fact that a certain waveguide guides optical waves, the problem of finding it exactly is intractable. Hence approximate methods are needed for obtaining the optical field distributions in optical waveguides with arbitrary refractive index distributions and over a period of time these have been developed.

The two main approximate methods that have emerged are the effective refractive index method and the finite element method. The development of both methods began ca. 1969. The concept of the effective dielectric constant* was first introduced by Knox and Toulios in 1970 [32] as an extension to the method of Marcatili [25]. Hocker and Burns [33] used to it find the propagation constants for arbitrary waveguides. Optical field distributions can be obtained using the propagation constants and any of a number of numerical techniques for solving second order differential equations, for example the method of Runge-Kutta [34]. The application of the finite element method to solving

---

* The term effective refractive index was applied somewhat later but the only difference is that the effective dielectric constant is defined to be $\varepsilon_{re} = \beta^2/k_o^2$ and the effective refractive index is defined to be $n_{eff} = \beta/k_o$.

electromagnetic waveguiding problems began with Ahmed and Daly's paper [35]. Later it was applied to arbitrarily shaped inhomogeneous optical waveguides by Yeh et al. [36]. More recently Koshiba et al. have used the finite element method to analyze anisotropic optical waveguides [37]. Other techniques based on, for example, expansion in terms of circular harmonics [38], the WKB method* [39], Green's functions [40], or finite difference methods [41] have been applied to optical waveguiding problems but the finite element method and the effective refractive index method have received by far the most attention.

Variational methods have long been applied to electromagnetic waveguiding problems in metal clad waveguides.** The variational method has also been used to obtain approximate width parameters for the optical field distributions and propagation constants of circular core optical fibers.*** In fact the finite element method is itself a variational technique [44]. Here the variational

---

* The eigenvalue equation derived in the WKB method can be used to find the effective refractive index and is in fact the same as that derived by Hocker and Burns [33] using a wave vector (ray) approach. Therefore it is not necessarily a separate method but may in fact be considered as part of the effective refractive index method.

** Harrington [42] chapter 7 pp. 317-380.

*** Marcuse [19] pp. 339-347 or Okoshi [43] pp. 114-121.

method has been extended to derive the optical field distributions of the fundamental mode of a channel waveguide with an arbitrary refractive index profile.

In the variational method an expression for the eigenvalues of the Euler-Lagrange equation of a stationary integral of a functional is derived. In this application the Euler-Lagrange equation is the scalar wave equation. Using the integral of the functional an expression for β^2 (the eigenvalue), of a particular mode of the waveguide, is obtained. Furthermore it is known that the eigenvalues are stationary values. Thus by plotting β^2 as a function of certain variable parameters of a function chosen to approximate the optical field distribution those values of the parameters which make β^2 stationary may be found.

In section 2.5 the choice of Hermite-Gaussian functions as the approximate optical field distribution will be motivated. The Hermite-Gaussian functions used have two variable parameters that determine the transverse extent of the optical field distribution. Here the equations relevant to the variational method are developed for the exact solution.

The general form of the scalar wave equation can be expressed in the form

$$\nabla_t^2 \psi + v^2(y,z)\psi = 0 \ ,$$

where

$$\nabla_t^2 \psi = \frac{\partial^2 \psi}{\partial y^2} + \frac{\partial^2 \psi}{\partial z^2} .$$

If the above wave equation is multiplied by ψ and the result is integrated over the entire yz-plane* it gives

$$\int_{-\infty}^{\infty} \int_{-\infty}^{\infty} \left\{ \psi \nabla_t^2 \psi + v^2(y,z) \psi^2 \right\} dydz = 0$$

and if Green's Theorem is applied to the first term of this integral one gets

$$\int_{-\infty}^{\infty} \int_{-\infty}^{\infty} \psi \nabla_t^2 \psi \, dydz = - \int_{-\infty}^{\infty} \int_{-\infty}^{\infty} \left\{ \left(\frac{\partial \psi}{\partial y} \right)^2 + \left(\frac{\partial \psi}{\partial z} \right)^2 \right\} dydz + \int_C \psi \frac{\partial \psi}{\partial n} ds$$

of which the last term on the right hand side is equal to zero. Finally the integral

$$I = \int_{-\infty}^{\infty} \int_{-\infty}^{\infty} \left\{ \left(\frac{\partial \psi}{\partial y} \right)^2 + \left(\frac{\partial \psi}{\partial z} \right)^2 - v^2(y,z) \psi^2 \right\} dydz = 0 \qquad (2.10)$$

is obtained.

---

* The domain of integration for a dielectric optical waveguide is the entire transverse plane. This is due to the boundary condition for the guided modes of these waveguides which forces the optical field to be zero at infinity if the guided power is to remain finite. Yariv and Yeh [45] chapter 11 pp. 405-503.

It remains to be shown that equation 2.10 is in fact stationary and that it is a minimum. In appendix B the proof is presented that equation 2.10 is stationary and that the general form of the scalar wave equation, given above, is the Euler-Lagrange equation.*

The wave equation for the exact optical field distribution, $\Phi_e(x,y,z)$ (the subscript e is for exact), is obtained from Maxwell's equations. In this work the scalar wave equation for an optical waveguide in which the refractive index varies in two dimensions, in the yz-plane, is

$$\frac{\partial^2 \phi_e}{\partial y^2} + \frac{\partial^2 \phi_e}{\partial z^2} + \left\{ \frac{\partial^2 \ln[n_z^2(y,z)]}{\partial z^2} + \frac{\partial \ln[\phi_e]}{\partial z} \frac{\partial \ln[n_z^2(y,z)]}{\partial z} + n_z^2(y,z)k_o^2 - \beta^2 \right\} \phi_e = 0$$

where $\Phi_e(x,y,z) = e^{-i\beta x}\phi_e(y,z)$, $n_z(y,z)$ is the refractive index distribution, and k_o is the free space wavenumber ($k_o = 2\pi/\lambda_o$). From the above equation the function $v^2(y,z)$, in the general form of the wave equation (page 46), is given by

$$v^2(y,z) = \frac{\partial^2 \ln[n_z^2(y,z)]}{\partial z^2} + \frac{\partial \ln[\phi_e]}{\partial z} \frac{\partial \ln[n_z^2(y,z)]}{\partial z} + n_z^2(y,z)k_o^2 - \beta^2.$$

---

* Fox [46] chapter 3 pp. 59-79.

However, in appendix B it is shown that equation 2.10 is stationary and the general form of the scalar wave equation is the Euler-Lagrange equation provided that $\delta v(y,z) = 0$. In the above equation this is obviously not so. In section 2.5.2 an approximation to $v^2(y,z)$, based on the approximate optical fields distributions, will be introduced that is independent of ϕ_e and which is then invariant and which will be the function that is actually used. In fact if one had a priori knowledge of the function ϕ_e then the above expression could also be treated as being invariant.

In the following section the approximate functions for the optical field distributions in the optical fiber and the VIOWM will be given and equation 2.10 and the above equation will be presented in terms of the approximations.

2.5 The Hermite-Gaussian Approximations

In this work approximations to the optical field distributions of the waveguides employed will be used. The approximation consists of choosing functions that are similar to those that are expected to be solutions to the scalar wave equation. The choice of the approximating functions should be based on a knowledge of the characteristics of solutions to similar problems where the exact solution is known. In the following subsections a

discussion of the choice of each of the approximate functions will be given in terms of its application to the waveguide used.

One of the main goals of this work is to show that the VIOWM has an application as a linking waveguide between two optical fibers (or other waveguides). It is therefore necessary to be able to predict the efficiency of coupling between the two waveguide types when they are brought together in a butt-coupling arrangement. If the optical field distributions in both waveguide types can be expressed in terms of Hermite-Gaussian functions it is possible to obtain a closed form analytic solution for the coupling coefficient.

As will be shown in section 2.6 the coupling coefficient is obtained in terms of the overlap integral of the two field distributions. The contribution to the overlap integral made by the evanescent fields is obviously small. Therefore the fact that the evanescent field of the approximate functions will be of the form $\exp(-r^2)$ rather than of the form $\exp(-r)$ will have little effect.* Thus it is seen that if the approximate optical field distributions are to be used to calculate the coupling coefficients for butt-coupled waveguides that it is most important that the

---

* For this reason Hermite-Gaussian functions should not be used to approximate optical field distributions in evanescent field coupling problems. However, in the current problem they are entirely appropriate.

approximations be close to the actual distributions in the regions where the fields are largest.

2.5.1 The Optical Fiber

It has long been known that a high permittivity dielectric rod can act as a waveguide* and solutions to the wave equation have been obtained for rods with various cross sections including circular [29], elliptical [30], and rectangular [25]. Typically optical fibers have refractive index profiles that are either circularly symmetric or elliptically symmetric in the transverse plane, i.e. a plane normal to the direction of propagation. A useful approximation to the refractive index distribution of many fibers is the "step index" profile. The step index profile is one in which the refractive index of the core is assumed to have one value, n_{co}, and that in the cladding is assumed to have another value, n_{cl}, such that $n_{co} > n_{cl}$. Figure 2.12 illustrates the refractive index profile of a step index fiber. Few, if any, of the commercially available optical fibers have a step index profile. The profiles of these fibers have refractive index distributions that are determined by the method of fabrication.

---

* See Okoshi [43] chapter 1 pp. 1-16 for an historical development.

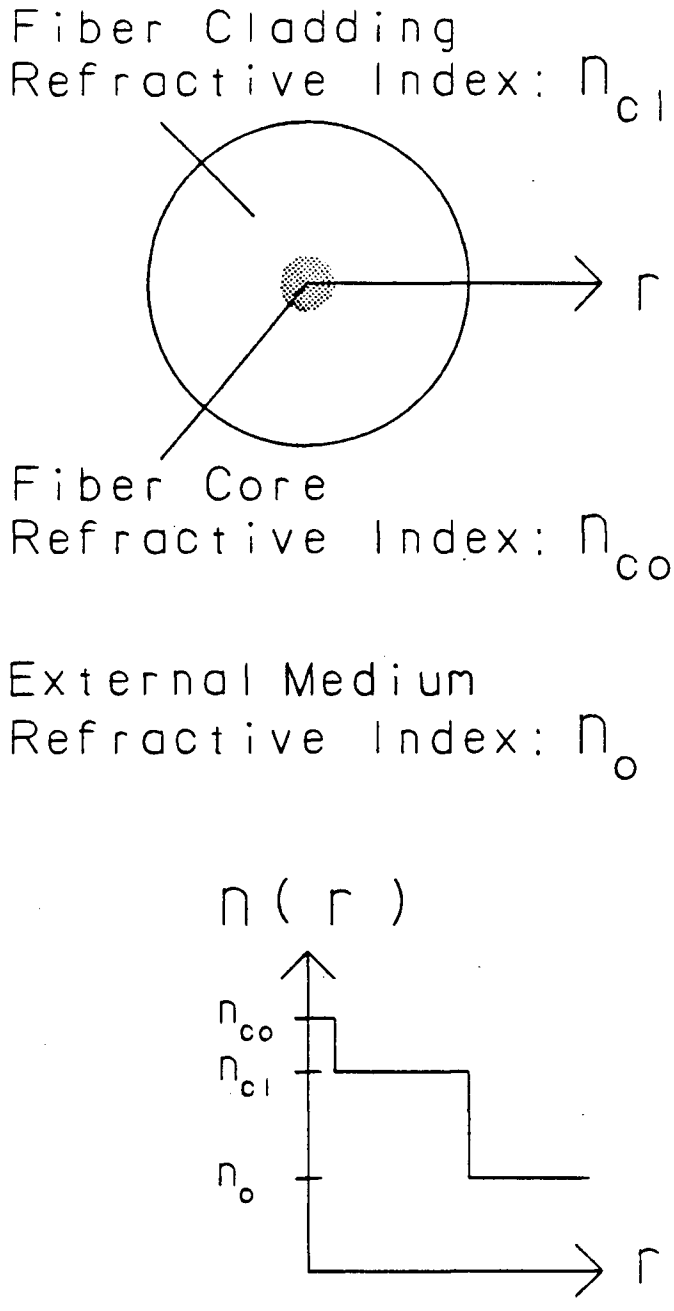

Figure 2.12: The refractive index distribution of a fiber with step index profile.

While exact solutions exist for both circular and elliptical cross section fibers with a step index profile [29,30] they are in terms of rather complicated higher functions. For example the circular core step index fiber has solutions that are in terms of Bessel functions in the core and in terms of modified Kelvin functions in the cladding.* While such solutions form a complete set of basis functions useful in describing the optical field distributions in large core multi-mode fibers and for calculating the propagation constants of the various modes, thus allowing the study of optical fibers in a general theoretical sense, they are of little practical use when dealing with the light emanating from a particular single-mode optical fiber.

Often it is easier to work with an approximation to the exact solution. Gaussian** approximations are particularly useful. They are mathematical simpler to use having the form $\exp(-r^2)$. They are known to propagate in free space*** and so the propagation characteristics (the diffraction characteristics) of a beam launched into free space from a

---

* Marcuse [19] chapter 8 pp. 286-347.

** A Gaussian function is a Hermite-Gaussian function multiplied by the Hermite polynomial H_0 which is equal to 1.

*** Verdeyen [47] chapter 3 pp. 53-69.

fiber, say as part of an optical system, is predictable. The coupling efficiency of a focused laser beam to a guided Gaussian mode is easily calculated [48]. Furthermore the Gaussian profile is found to be the solution to the wave equation for fibers with a quadratic refractive index profile.*

It is also demonstrable that the Gaussian approximation is in fact a good approximation to the optical field distributions encountered in single-mode optical fibers. Comparisons of theoretically predicted profiles for fibers have been compared to the Gaussian function [41] and have indicated a close correlation between the two. Also comparisons between measured power distributions emanating from actual fibers and the Gaussian function have been made [49,50] again showing a convincing correlation.

The optical field distribution of a circularly symmetric fiber may in general be seen as being composed of two degenerate, orthogonal polarizations.** The choice of the directions of polarization is arbitrary for these two modes, therefore in this work it will be assumed that one polarization is coincident with the y-axis and one with the z-axis. In the case of polarization-preserving fiber the two modes are no longer degenerate still it will be assumed

---

* Ibid.

** Okoshi [43] chapter 4 pp. 48-81.

that the fiber is oriented so that, as above, one polarization is coincident with the y-axis and one with the z-axis.

Since the electric field of the optical distribution in a VIOWM is polarized parallel to the z-axis only the optical field distribution in the fiber that is also polarized parallel to the z-axis need be considered. The optical field in the fiber can thus be approximated by the expression

$$\Phi_f(x,y,z) = e^{-i\beta_f x}\phi_f(y,z) \qquad (2.11)$$

where the subscript f stands for fiber and

$$\phi_f(y,z) = a_f e^{-(y^2/w_{yf}^2 + z^2/w_{zf}^2)/2}$$

where a_f is the normalized amplitude and w_{yf} and w_{zf} are the width parameters in the y and z-directions respectively. The normalized amplitude is a constant that ensures that the mode carries unit power and will is discussed further in appendix C.

Figure 2.13 shows a Gaussian optical field distribution in which $w_{yf} = w_{zf}$ and figure 2.14 shows one in which $w_{yf} = w_{zf}/2$.

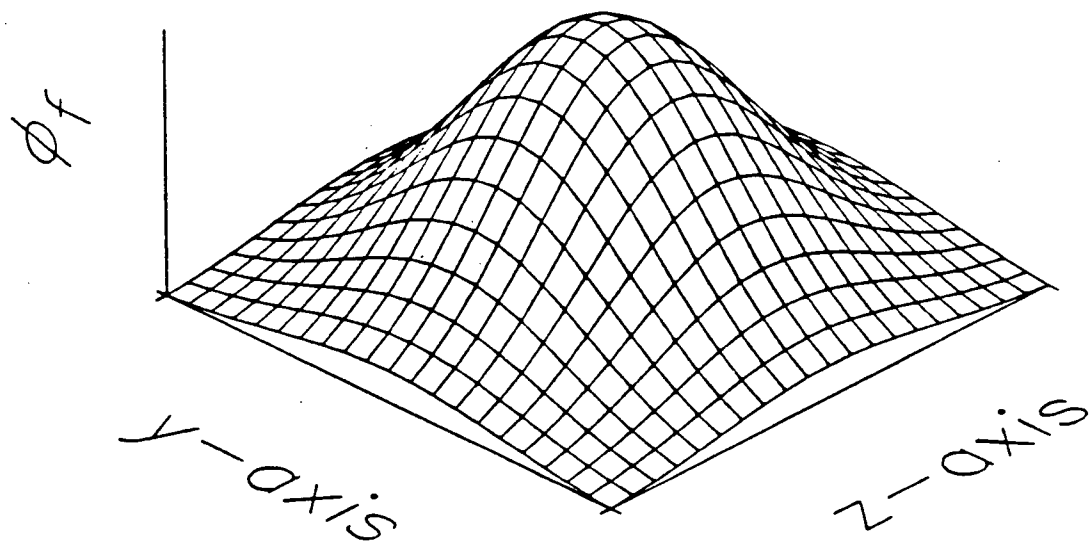

Figure 2.13: A Gaussian optical field distribution in which $w_{yf} = w_{zf}$.

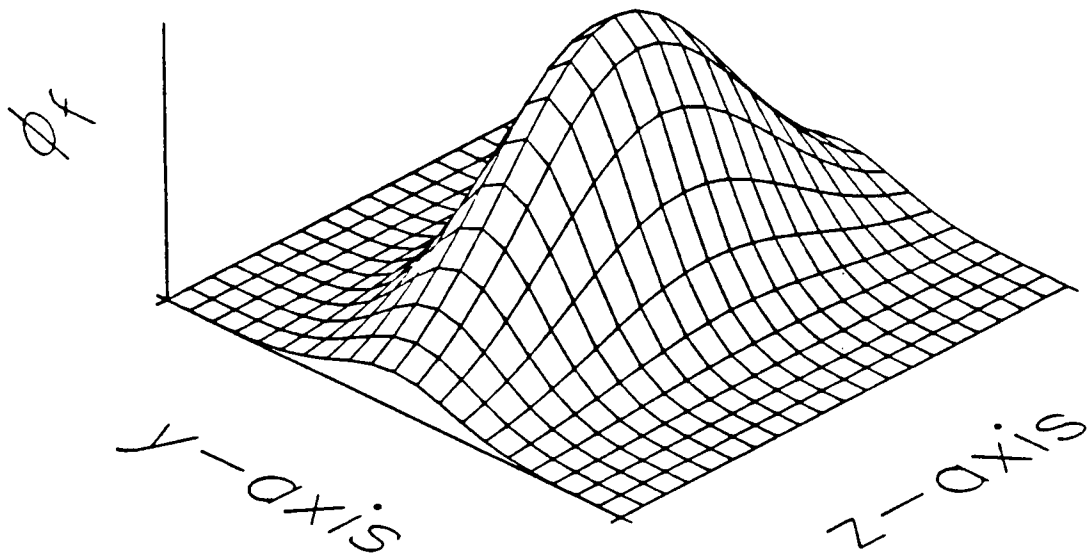

Figure 2.14: A Gaussian optical field distribution in which $w_{yf} = w_{zf}/2$.

2.5.2 The Voltage Induced Optical Waveguide

Based on the material presented in sections 2.2 and 2.3 it can be seen that the refractive index distribution will be rather complex for both the planar and ridge VIOWM. Since it is very unlikely that an exact solution to the wave equation could be found for a waveguide with such a refractive index distribution the variational method will be used. In this section the choice of Hermite-Gaussian functions to approximate the actual optical field distributions is justified.

To begin with, certain observations can be made about the refractive index distribution and a knowledge of the optical field distributions in similar waveguides can be used:

1) The refractive index distribution is symmetric with respect to the xy-plane,

2) The difference in the refractive index of the substrate and the optical buffer layer is large,

3) And for a certain range of applied voltages the change induced in the refractive index of the substrate is larger in the interelectrode gap region than in the "surrounding" region and the change induced in the

surrounding region decreases monotonically to zero at infinity.*

From the above observations certain characteristics of a bound mode can be anticipated.

1) The optical field distribution will be either symmetric or anti-symmetric with respect to the xy-plane,

2) The shape of the optical field distribution will be such that it is very small at the boundary between the substrate and the buffer layer as compared to its peak value further into the substrate,

3) Most of the power will be confined to the interelectrode gap region and will decrease monotonically to zero at infinity in the surrounding region.

Hence trial functions must be chosen which will have similar characteristics.

In order to understand the modus operandi of the VIOWM only the lowest order mode need be considered. The lowest order mode will be the most highly confined mode for the

---

* The "surrounding" region is defined here as that region in which the refractive index decrease is monotonic.

lowest operating voltage and will have the highest degree of coupling to or from the fiber if the fiber is well positioned. The approximate optical field distribution for the VIOWM will be designated $\Phi_v(y,z)$, subscript v for VIOWM, and is given by

$$\Phi_v(y,z) = \begin{cases} e^{-i\beta_v x}\,\phi_v(y,z) & ;\ y \geq 0 \\ 0 & ;\ y < 0 \end{cases} \qquad (2.12)$$

where β_v is the propagation constant of the mode and

$$\phi_v(y,z) = a_v \left(\frac{y}{w_{yv}} \right) e^{-(y^2/w_{yv}^2 + z^2/w_{zv}^2)/2}$$

where a_v is the normalized amplitude, w_{yv} and w_{zv} are the width parameters in the y and z-directions respectively.* The normalized amplitude is discussed further in appendix C.

Figure 2.15 shows a Hermite-Gaussian optical field distribution in which $w_{yv} = w_{zv}$ and figure 2.16 shows one in which $w_{yv} = w_{zv}/2$.

As can be seen from figures 2.15 and 2.16 the Hermite-Gaussian approximations to the field distributions meet each of the desired characteristics: they are symmetric with respect to the xy-plane, they are small, zero in fact, at

---

* As can be seen $\Phi_v(y,z)$ has the form $H_1(y)\exp(-y^2)$ in the y-direction, for positive y, and $H_0(z)\exp(-z^2)$ in the z-direction, for all z, hence the name Hermite-Gaussian.

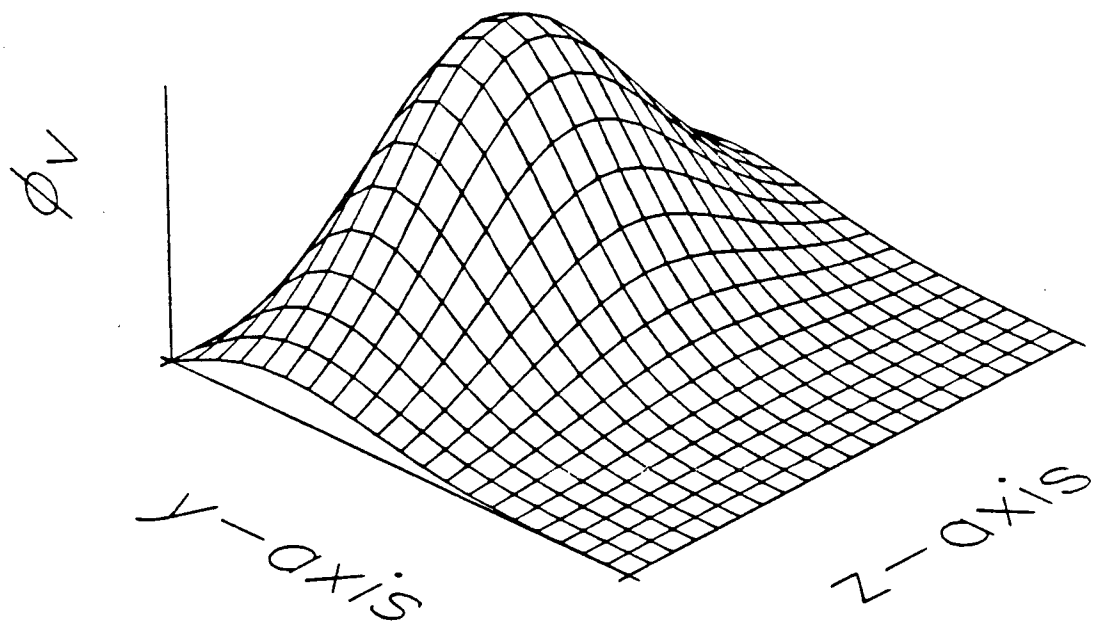

Figure 2.15: A Hermite-Gaussian optical field distribution in which $w_{yv} = w_{zv}$.

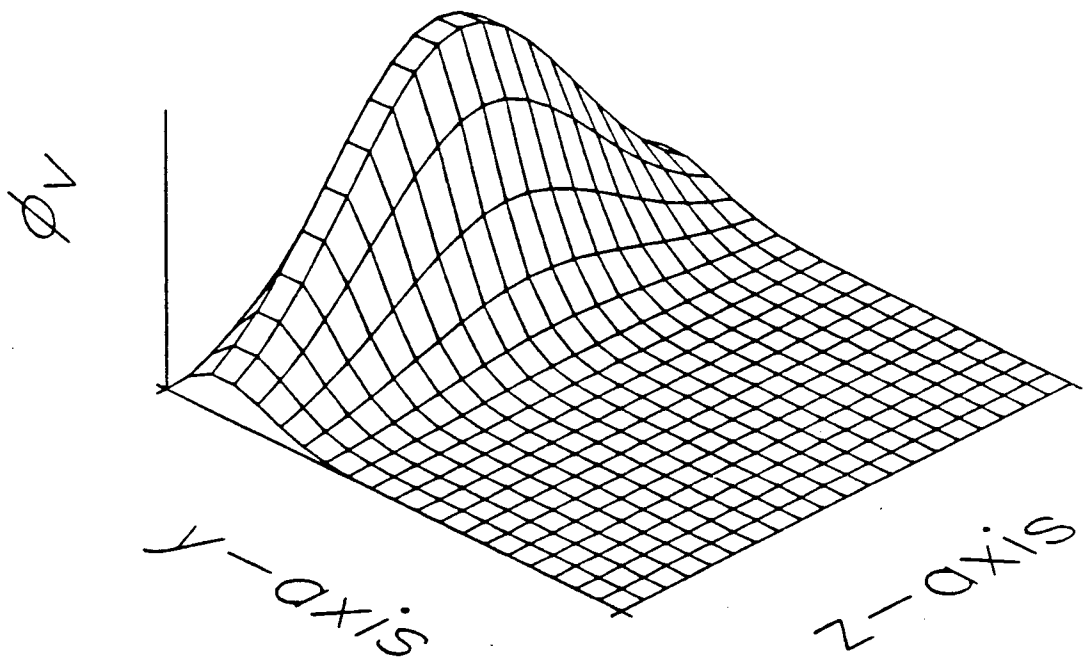

Figure 2.16: A Hermite-Gaussian optical field distribution in which $w_{yv} = w_{zv}/2$.

the interface between the substrate and the optical buffer layer, and the evanescent field goes to zero monotonically at infinity.

In section 2.4 all the results were derived in terms of the exact field distribution. Now the equations are presented in terms of the approximate functions. To begin with the approximation to $v^2(y,z)$ is given in terms of the approximate optical field distribution by

$$v_v^2(y,z) = \frac{\partial^2 \ln[n_z^2(y,z)]}{\partial z^2} - \frac{z}{w_{zv}^2}\frac{\partial \ln[n_z^2(y,z)]}{\partial z} + n_z^2(y,z)k_o^2 - \beta_v^2 .$$

which gives the stationary integral for this approximation

$$I = \int_{-\infty}^{\infty}\int_{-\infty}^{\infty}\left\{\left(\frac{\partial\psi}{\partial y}\right)^2 + \left(\frac{\partial\psi}{\partial z}\right)^2 - v_v^2(y,z)\psi^2\right\} dydz = 0 \qquad (2.13)$$

which becomes

$$I_v = \int_{-\infty}^{\infty}\int_{-\infty}^{\infty}\left\{\left(\frac{\partial\phi_v}{\partial y}\right)^2 + \left(\frac{\partial\phi_v}{\partial z}\right)^2 - v_v^2(y,z)\phi_v^2\right\} dydz \qquad (2.14)$$

in terms of the approximate function.

The first two terms of the integral I_v can be evaluated exactly and are given by

$$\int_{-\infty}^{\infty}\int_{-\infty}^{\infty}\left(\frac{\partial\phi_v}{\partial y}\right)^2 dydz = \frac{1.5}{w_{yv}^2}\int_{-\infty}^{\infty}\int_{-\infty}^{\infty}\phi_v^2\, dydz$$

and

$$\int_{-\infty}^{\infty}\int_{-\infty}^{\infty}\left(\frac{\partial\phi_v}{\partial z}\right)^2 dydz = \frac{0.5}{w_{zv}^2}\int_{-\infty}^{\infty}\int_{-\infty}^{\infty}\phi_v^2\, dydz\ .$$

Since I is a minimum I_v must provide an upper bound on I; i.e. $I_v \geq I$. Therefore if 2.13 is rewritten to provide an equation for β_v

$$\beta_v^2 = \frac{-\int_{-\infty}^{\infty}\int_{-\infty}^{\infty}\left[\left(\frac{\partial\psi}{\partial y}\right)^2+\left(\frac{\partial\psi}{\partial z}\right)^2-\left\{\frac{\partial^2 \ln[n_z^2(y,z)]}{\partial z^2}-\frac{z}{w_{zv}^2}\frac{\partial \ln[n_z^2(y,z)]}{\partial z}+n_z^2(y,z)k_o^2\right\}\psi^2\right]dydz}{\int_{-\infty}^{\infty}\int_{-\infty}^{\infty}\psi^2\, dydz}$$

then rewriting equation 2.14 in a similar fashion provides a lower bound on β_v

$$\beta_v^2 \geq -\frac{1.5}{w_{yv}^2}-\frac{0.5}{w_{zv}^2}+\frac{\int_{-\infty}^{\infty}\int_{-\infty}^{\infty}\left\{\frac{\partial^2 \ln[n_z^2(y,z)]}{\partial z^2}-\frac{z}{w_{zv}^2}\frac{\partial \ln[n_z^2(y,z)]}{\partial z}+n_z^2(y,z)k_o^2\right\}\phi_v^2\, dydz}{\int_{-\infty}^{\infty}\int_{-\infty}^{\infty}\phi_v^2\, dydz}\ .$$

Since the propagation constant is a stationary value the above equation can be used to find the width parameters w_{yv}

and w_{zv}. Proof that β_v is a stationary value is provided in appendix B. By varying the width parameters a grid of values for β_v^2 can be created and the values of w_{yv} and w_{zv} for which β_v^2 is stationary may be found graphically.

Figure 2.17 shows a plot of β_v^2 versus w_{yv} and w_{zv} for a planar VIOWM with a 4μm interelectrode gap with 50.0V applied to the electrodes and where λ_o = 442nm, n_e = 2.2884, n_o = 2.371, r_{33} = 30.8x10^{-12}m/V, and r_{42} = 28.0x10^{-12}m/V.

Figure 2.18 shows the development of the optical field for the VIOWM with the 4μm interelectrode gap with increasing voltage, for applied voltages of 10.0, 30.0, and 50.0 volts, as predicted by the variational method.

2.6 The Coupling Coefficient

Hermite-Gaussian functions have the advantage, as the chosen approximate optical field distributions, that they are convenient to manipulate mathematically. In the following, the coupling coefficients are determined by expanding the optical fields in the two butt-coupled waveguides in terms of both guided and radiation modes. This approach has been used by Burns and Milton [51] to study the conversion of modes in separating waveguides and by Hunsperger et al. [52] to study butt-coupling between solid state lasers and surface waveguides.

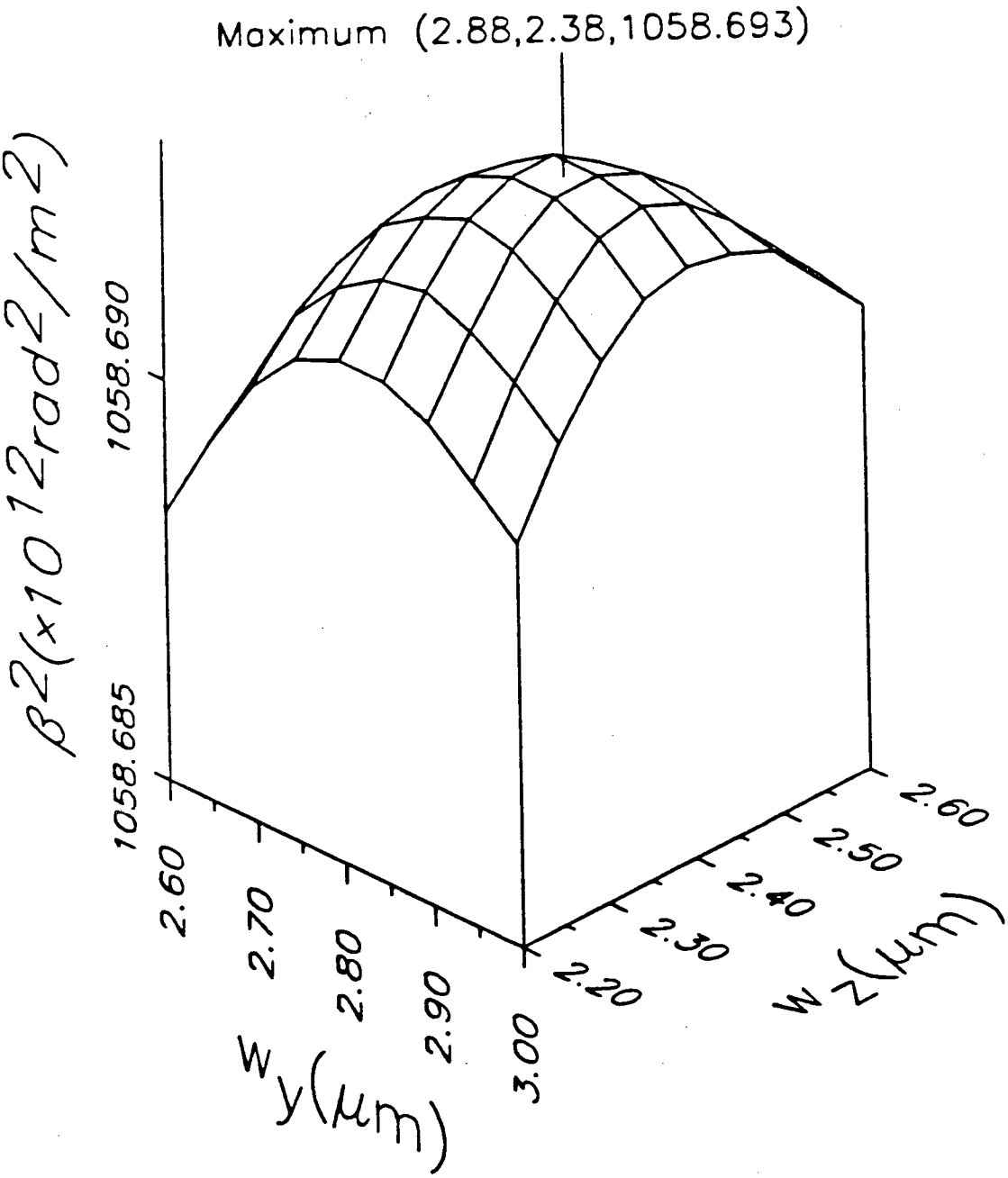

Figure 2.17: A plot of β_V^2 versus w_{yv} and w_{zv} for a VIOWM with a 4μm interelectrode gap with 50.0V applied to the electrodes for λ_o = 442nm.

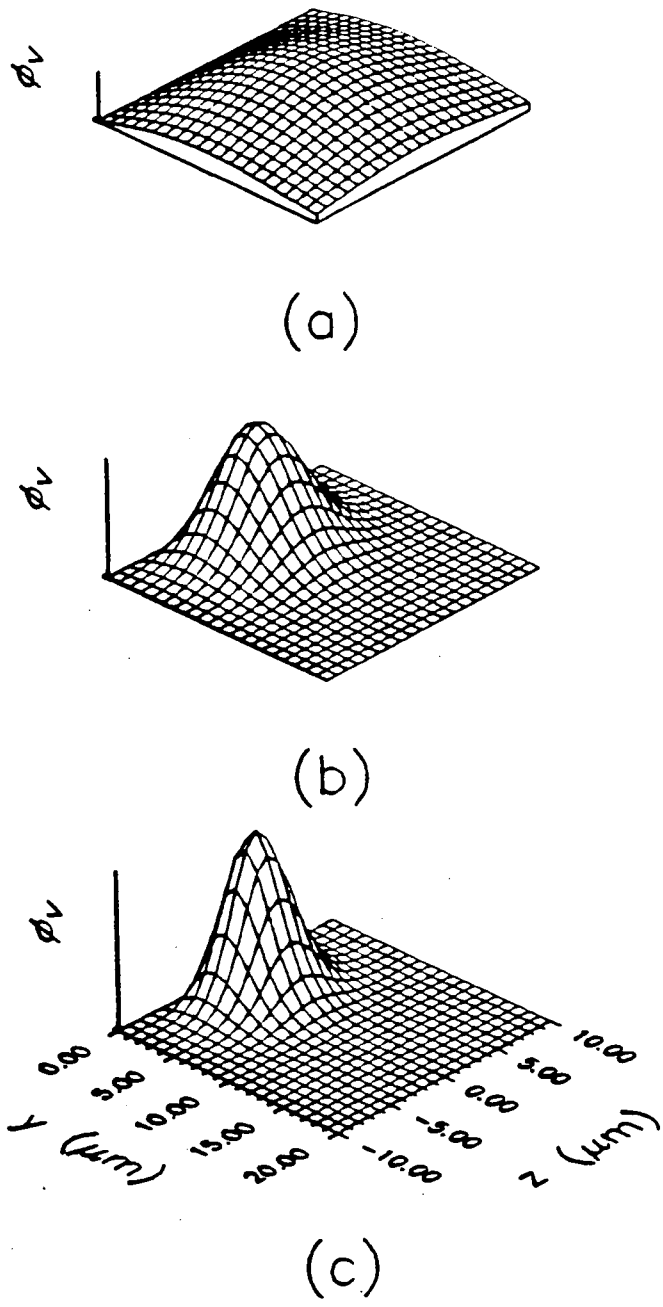

Figure 2.18: The development of the optical field for a VIOWM with a 4μm interelectrode gap for (a) 10.0, (b) 30.0, and (c) 50.0V applied to the electrodes for λ_o = 442nm.

The continuity of the tangential field components at the interface between the optical fiber and the VIOWM is considered. If both waveguides are assumed to be designed for single-mode operation one can write

$$\Phi_f + R\Phi_f + E_{ref} = T\Phi_v + E_{trans} \tag{2.15a}$$

for the electric field and

$$\beta_f\Phi_f + R\beta_f\Phi_f + H_{ref} = T\beta_v\Phi_v + H_{trans} \tag{2.15b}$$

for the magnetic field for coupling from the optical fiber to the VIOWM. Here R and T are the reflection and transmission coefficients, respectively, and E_{ref} and E_{trans} are the reflected and transmitted electric field distributions of the radiated modes and similarly H_{ref} and H_{trans} are the reflected and transmitted magnetic field distributions of the radiated modes.

To solve for the coupling between the two waveguides the assumption is made that the power in the reflected radiated modes is negligible and that the major part of the reflected power is in the back traveling guided mode. Each of the remaining terms, remaining after the terms representing the reflected radiated mode have been dropped, is multiplied by $\beta_v^2\Phi_v^*$ in equation 2.15a and is multiplied by $\beta_v\Phi^*$ in equation 2.15b and both are integrated over the boundary plane, the interface between the optical fiber and the VIOWM, which is assumed to be the plane $x = 0$. The two

resulting equations are then subtracted, one from the other, leaving

$$\beta_v(\beta_f - \beta_v)\int_{-\infty}^{\infty}\int_{-\infty}^{\infty} \Phi_v^* \Phi_f \, dydz - R\beta_v(\beta_f + \beta_v)\int_{-\infty}^{\infty}\int_{-\infty}^{\infty} \Phi_v^* \Phi_f \, dydz = 0$$

and solving for R gives

$$R = \frac{\beta_f - \beta_v}{\beta_f + \beta_v} = \frac{n_f' - n_v'}{n_f' + n_v'} = \Gamma \qquad (2.16)$$

where n_f' and n_v' are the effective refractive indices of the optical fiber and the VIOWM, respectively, and Γ is the Fresnel reflection coefficient for plane waves at normal incidence.

To justify neglecting the power in the reflected radiated modes one must look at the result that equation 2.16 represents. In effect the assumption is that the reflected power, Γ^2, in the case of optical waveguides is essentially the same as that for plane waves at normal incidence. The plane wave solution is, in fact, the limiting case for weakly guided modes. In other words as the variations in the refractive index distributions of the waveguides disappear on both sides of the boundary plane the optical field distributions extend to become plane waves and the amount of reflected power is exactly equal to Γ^2. The modes of the waveguides considered in this work are weakly guided, in that the extents of the optical field

distributions are much greater than a wavelength, and the amount of power reflected is small, $\Gamma^2 \approx 5\%$ of the total incident power, therefore the approximation should lead to reasonable results.

Using equations 2.15a and b the transmission coefficient can be solved for. First 2.15a is multiplied by $\beta_v\beta_f\Phi_v^*$ and 2.15b is multiplied by $\beta_v\Phi_v^*$ and the resulting equations are integrated over the boundary plane x = 0. This time, however, the equations are added resulting in

$$2\beta_v\beta_f\int_{-\infty}^{\infty}\int_{-\infty}^{\infty}\Phi_v^*\Phi_f\,dydz = T\beta_v(\beta_f+\beta_v)\int_{-\infty}^{\infty}\int_{-\infty}^{\infty}\Phi_v^*\Phi_v\,dydz$$

which after some rearrangement gives

$$T = \frac{2a_f\beta_f\int_{-\infty}^{\infty}\int_{0}^{\infty}\left(\frac{y}{w_{yv}}\right)e^{-(y^2/w_{yv}^2 + z^2/w_{zv}^2 + (y-a)^2/w_{yf}^2 + (z-b)^2/w_{zf}^2)/2}\,dydz}{a_v(\beta_f+\beta_v)\int_{-\infty}^{\infty}\int_{0}^{\infty}\left(\frac{y}{w_{yv}}\right)^2 e^{-(y^2/w_{yv}^2 + z^2/w_{zv}^2)}\,dydz}$$

where the variables a and b locate the center of the optical fiber relative to the center of the surface of the waveguiding region of the VIOWM, see figure 2.19. The ratio a_f/a_v is determined by normalizing the power in each mode and is given by*

---

* See appendix C.

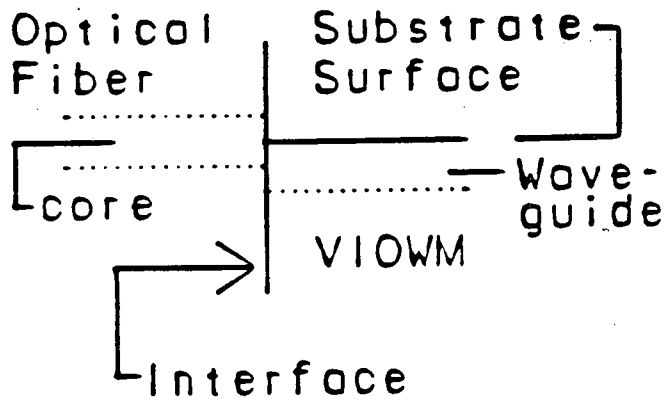

Edge View

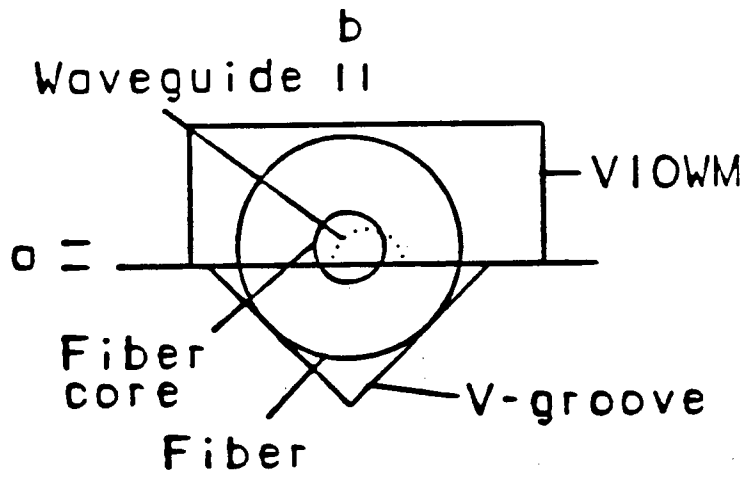

End View

Figure 2.19: The interface between the optical fiber and the VIOWM.

$$\frac{a_f}{a_v} = \left[\frac{\beta_v \int_{-\infty}^{\infty}\int_{0}^{\infty} \left(\frac{y}{w_{yv}} \right)^2 e^{-(y^2/w_{yv}^2 + z^2/w_{zv}^2)} \, dydz}{\beta_f \int_{-\infty}^{\infty}\int_{-\infty}^{\infty} e^{-(y^2/w_{yf}^2 + z^2/w_{zf}^2)} \, dydz} \right]^{\frac{1}{2}} .$$

The expression for the transmission coefficient can be rewritten* as

$$T = \frac{2(\beta_f\beta_v)^{1/2}\Omega_y\Omega_z^{1/2} \; e^{-(a^2/w_{yf}^2 + b^2/w_{zf}^2)/2 + b^2\Omega_z/4w_{zf}^4}}{\pi^{1/2}(\beta_f + \beta_v)(w_{yv}w_{zv}w_{yf}w_{zf})^{1/2}w_{yv}}$$

$$\times \left[1 + \frac{a\Omega_y^{1/2}\pi^{1/2} \; e^{a^2\Omega_y/4w_{yf}^4} \; \mathrm{erfc}\left(\frac{-a\Omega_y^{1/2}}{2w_{yf}^2} \right)}{2w_{yf}^2} \right] \qquad (2.17)$$

where

$$\Omega_y = \frac{2w_{yv}^2 w_{yf}^2}{w_{yv}^2 + w_{yf}^2}$$

and

---

* See appendix C.

$$\Omega_z = \frac{2w_{zv}^2 w_{zf}^2}{w_{zv}^2 + w_{zf}^2} .$$

A similar line of reasoning yields an equation that is identical to equation 2.17 for light coupled from a VIOWM to an optical fiber.

As is evident from equation 2.17 the location of the fiber relative to the input of a VIOWM is important in determining the coupling. It is obvious that in the z-direction the best coupling is obtained when b = 0 as this will give the best overlap between any two Gaussian distributions independent of their respective width parameters. On the other hand finding the best location in the y-direction will depend on the operating voltage and mode of operation, see chapter 4.

Chapter 3

FABRICATION

3.1 Introduction

In this chapter the fabrication of both planar and ridge VIOWMs in lithium niobate, including cutting and polishing, and of V-grooves in silicon is described. Also included is a section on the alignment of the VIOWMs and optical fibers using the V-grooves. The fabrication and alignment information is contained in three sections entitled:

The VIOWM,
The Silicon V-groove, and
Device/Optical Fiber Alignment.

The VIOWM section begins by discussing issues that are common to the fabrication of both planar and ridge devices. Then the fabrication techniques that are unique to each device type are contained in their own subsections. The

cutting and polishing of two types of device is contained in a separate subsection.

The silicon V-groove section is dedicated to a description of the anisotropic etching of silicon to produce V-grooves.

V-grooves etched in silicon can be used to form a stable method of coupling light into and out of integrated optic devices by a flip-chip technique [21]. The device/optical fiber alignment section describes the alignment of a VIOWM and an optical fiber using an array of V-grooves. The combination of a VIOWM and an optical fiber on the V-groove array is used as an optical front-end switch. Measurements on the switch are presented in chapter 4.

3.2 The VIOWM

The initial preparation of the $LiNbO_3$ wafers was the same for both planar and ridge devices as was the final cutting and polishing stage in the fabrication. The devices were fabricated on Y-cut* $LiNbO_3$ wafers obtained from Crystal Technology Inc., Palo Alto, Ca. The wafers were 3 inches in diameter and 0.04 inches thick. In order to make

---

* These substrates are cut and polished so that the Y-axis of the crystal is normal to the optical quality surface.

better use of the large wafers they were divided into quarters by first covering the entire optically polished face of the wafer with a coat of Al about 1μm thick evaporated using a conventional diffusion pumped vacuum system (made by Carl Hermann Assoc.) capable of holding 3 sources. The Al protected the optically polished surface from scratches during the cutting process and provided a means of undercutting any inert dirt that had been picked-up. The cutting was done on a high speed diamond saw. The Al layer was removed by etching in a 1:1 solution of phosphoric acid and DI (de-ionized) water at 50°C.

The wafers were then cleaned by immersion in a 1% solution of Alconox for 5 min. followed by a 10 min. rinse in DI water, a 5 min. soak in buffered HF followed by a 10 min. rinse in DI water, and a 5 min. soak with ultrasonic agitation in boiling methanol. The sample was heated with the methanol then both were transferred to the agitator in order to avoided thermal shock shattering the $LiNbO_3$.

After removal from the boiling methanol the wafers were blown dry with nitrogen immediately prior to being loaded into a Perkin-Elmer Sputtering System Model 3140.

The patterning of the waveguides on the $LiNbO_3$ substrates was done using photolithography. The mask used was made by Sierracin, Santa Clara, Ca. On the mask were long stripes varying in length from 1 to 23 mm and in width from 4 to 10 μm. Photoresist was patterned on the sample so

that the longer dimension of the stripes would run parallel to the X-axis of the crystal. Thus the waveguides would run parallel to the XY-plane of the crystal and the electric field, created by application of voltage to the electrodes, would have a component parallel to the Z-axis.

3.2.1 The Planar VIOWM

A 200 nm optical buffer layer of SiO_2 was RF sputtered (in the Perkin-Elmer sputtering system) onto the optically polished face of a section of the $LiNbO_3$ wafer. The target was nominally of 99.95% purity. The deposition was preceded by a 1 hr. preclean of the target with a shutter placed between the target and the wafer. The atmosphere in the chamber was 18 mTorr of Ar and 5 mTorr O_2. The sputtering was done at 100 W forward and about 2 W reflected power for 0.5 hr. The refractive index of SiO_2 is about 1.5 and it therefore provides a good optical buffer layer on $LiNbO_3$ which has a refractive index of about 2.3. See section 2.3.1.2.

The wafer was removed from the sputtering system and patterned with photoresist so as to allow the interelectrode gap to be formed using a lift-off technique [53].

The photoresist patterning was done as follows: the photoresist* was applied in a photoresist spinner at 4000 rpm for 25 sec.; a prebake was performed at 95°C for 25 min.; the photoresist was exposed to 320 nm radiation (UV) with a power density of 25 mW/cm^2 for 40 sec.; the photoresist was then soaked in chlorobenzene for 2.5 min. [53]; a post-bake was performed for 25 min. at 95°C; the photoresist was developed in a 1:1 solution of Shipley MF-312 developer and DI water; the final step was rinsing in flowing DI water. By this method a long and narrow photoresist ridge was formed with some undercutting so that the interelectrode gap could be fabricated using lift-off.

The electrodes of the planar VIOWM were designed so as to be joined to similar electrodes on the Si V-grooves by a eutectic bond. Therefore they were made out of AuGe with a eutectic temperature of 363°C.* However, the adhesion of AuGe on SiO_2 is poor and it was necessary to include a thin Ti layer between the two. Thus the electrodes were fabricated in the Carl Herrmann system, with one Ti and one AuGe source, by depositing 50 nm Ti on the SiO_2 and then 300 nm AuGe on the Ti.

---

* Shipley's S1400-30.

* Ghandhi [54] p. 59.

Once the metal had been deposited the photoresist was removed by immersion in a sequence of solvents for 5 min. each: hot (95°C) Microstrip**, hot acetone, and 2-propanol.

Figure 3.1 shows the interelectrode gap of a VIOWM. Here the gap is 4 μm wide.

3.2.2 The Ridge VIOWM

In a ridge VIOWM the ridges must be formed first. Etching $LiNbO_3$ has been achieved by several authors by several different methods including: argon ion milling [55], plasma etching in Freon plasmas using CF_4 [56], reactive ion-beam etching using CHF_3 [57], and reactive ion etching and using CF_4 and CCl_2F_2 [58]. In this work the $LiNbO_3$ substrate was sputter etched in an argon plasma.

After the initial cleaning the wafer was placed in the Perkins-Elmer sputtering system with a Ti source. The source was precleaned, by sputter etching, with a shutter between the target and the sample until the metal was being deposited. The plasma had a distinctive blue tint when Ti was being deposited, prior to which it is uniformly pink. The preclean usually takes between 1 and 2 hr.

** A product of Philip A. Hunt Chemical Corporation, West Paterson, N. J.

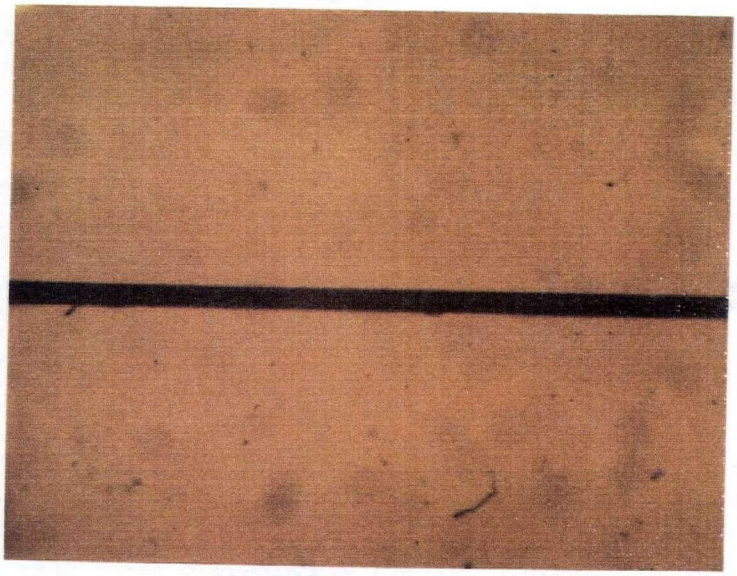

Figure 3.1: The interelectrode gap of a VIOWM. Here the gap is 4 μm wide.

The Ti was deposited with 100 W forward and about 2 W reflected power which gave a deposition rate of about 40 Å/min. The deposition was continued for 1.5 hr. giving a metal layer about 500 nm thick.

The Ti was formed into stripes by applying a photoresist mask to protect those areas that were not to be etched. The unprotected Ti was removed in a CF_4 plasma in a Plasma-Therm* system. The chamber pressure was 500 mTorr and the forward power was 100 W with 2 W reflected. The etch time varied with Ti thickness and was usually between 30 and 45 min. The photoresist was applied as described above for the planar VIOWM except that the chlorobenzene soak was omitted.

The remaining Ti stripes were then oxidized in a MiniBrute oven at 600°C with a 1 l/min. flow of O_2 for 12 hr. The oxide provided the mask for the sputter etch of the $LiNbO_3$.

The sputter etch was done in the Perkin-Elmer with 100 W forward and about 2 W reflected power at 18 mTorr. Here too the time was determined by the thickness of the oxidized Ti. As the Ti has a different etch rate than the $LiNbO_3$, about half, the time was decided upon by monitoring the differential etch rate. Before placing the sample in the

---

* A Multiversion Plasma, Reactive Ion Etch and Plasma Deposition System Model PK-1250PE/RIE/PD.

sputterer the thickness of the oxidized Ti was measured on a Tencor Alpha-Step 200 profilometer. After the first 4 hrs. of sputter etching the sample was removed from the sputterer and the new height was measured. The sample was then returned to the sputterer and the etching was continued for another 2 hrs. Then it was removed and the height was again measured. This process was repeated until there was no increase in the height of the ridges.

If the height of the ridge was insufficient then a new layer of Ti was deposited, patterned and oxidized and the ridge height was increased by further sputter etching.

Typically an initial Ti layer of 0.5 μm resulted in an increase in the ridge height of about 1.5 μm.

Once the desired ridge height was achieved and optical buffer layer of SiO_2 was deposited as described above for the planar VIOWMs.

Figure 3.2 is a scanning electron microscope (SEM) picture of a sputter etched ridge in $LiNbO_3$. The width of the ridge can be obtained from figure 3.3 where it is seen to be about 7.5 μm. Figure 3.4 is a photocopy of the profilometer output of the ridge shown in figures 3.2 and 3.3. The height of the ridge is seen to be 4 μm.

The electrodes for the ridge VIOWM were aluminum. They were sputter deposited with a bias applied to the sample table in an argon plasma at 18 mTorr. The bias causes some sputter-cleaning of the sample's surface which removes

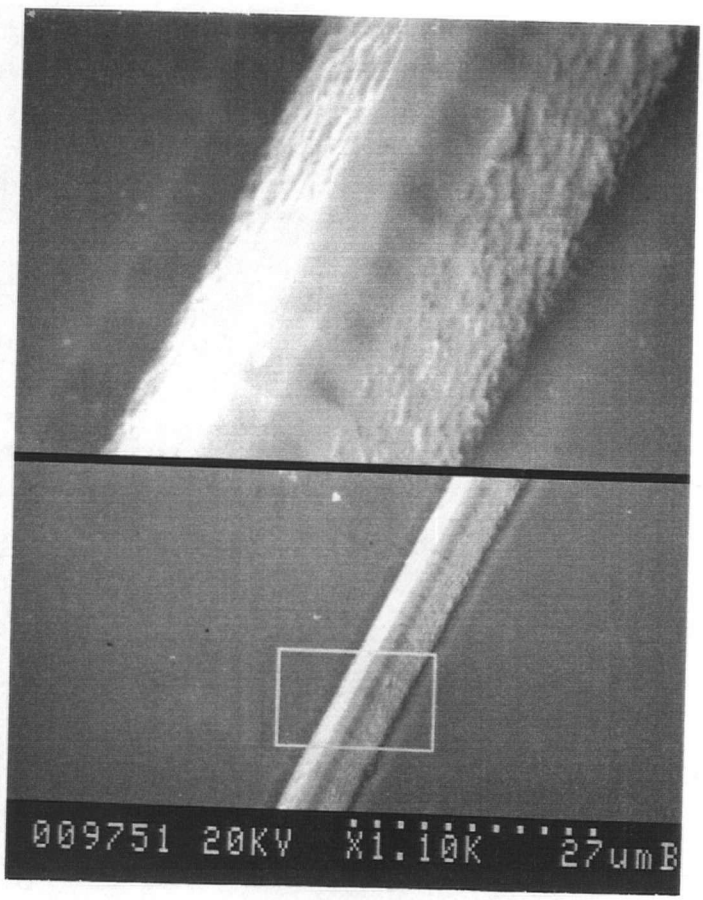

Figure 3.2: SEM picture of a ridge etched in $LiNbO_3$. The scale of the upper picture is 5 times that of the lower picture.

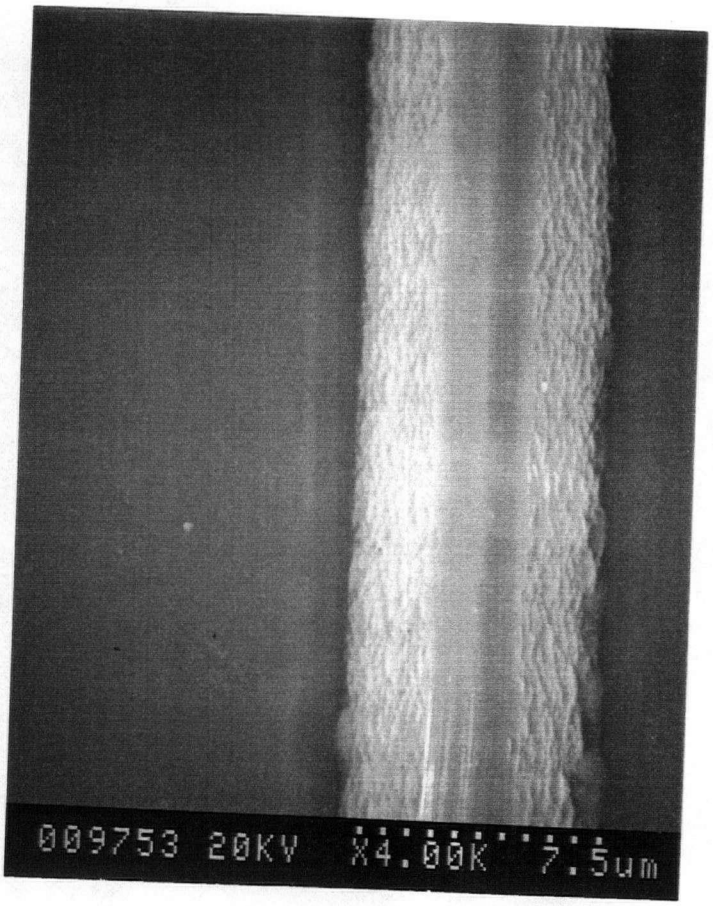

Figure 3.3: SEM picture showing that the ridge is about 7.5 µm wide.

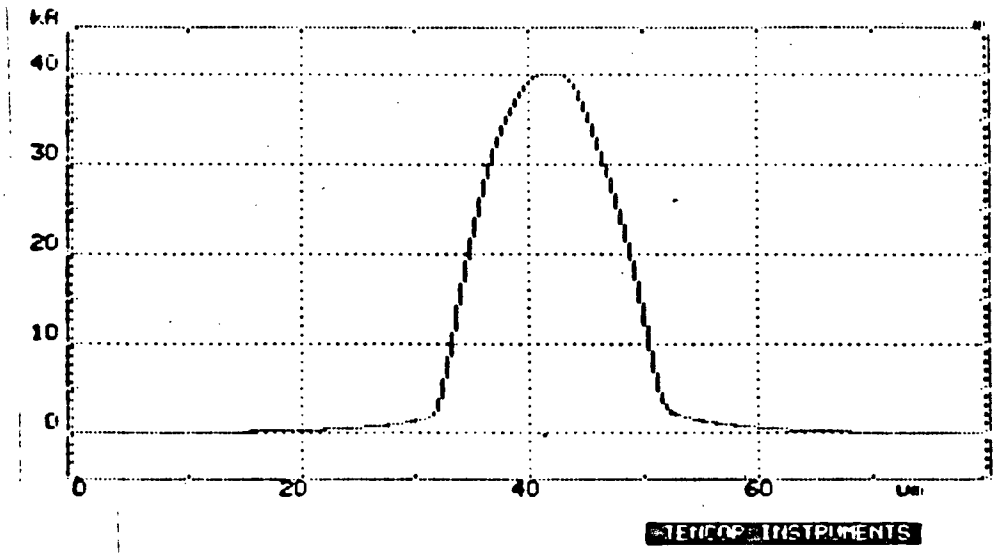

Figure 3.4: Profilometer output showing that the height of the ridge is 4 μm

adsorbed gases and which in turn increases the adhesion of the aluminum. The forward power was 100 W and the reflected power was about 2 W. The target was precleaned for an hour with a shutter placed between the sample and the target (with the bias applied to the sample table for only the last few minutes). Then the shutter was removed and Al was deposited for 2 hrs. The deposited metal layer was between 1 and 2 μm thick. The electrodes were formed by a self-aligned technique. Photoresist was spun onto the metal coated sample (Shipley's 1400-30 at 2000 rpm) at a low speed to give a thick layer in the valleys between the ridges and a thin layer on the tops of the ridges. The photoresist was hard baked for an hour at 130°C and etched in the Plasma-Therm in an oxygen atmosphere. The chamber pressure was 320 mTorr and the forward power was 100 W and the reflected power was 2 W. Etching was continued for about 50 min until the thin photoresist was removed from the tops of the ridges forming a narrow, ~ 4 μm, gap in the photoresist. The sample was then placed in the Perkin-Elmer system and sputter etched in an 18 mTorr Ar plasma until the aluminum along the tops of the ridges was removed (1/2 hr. longer than it took to deposit the Al).

Figure 3.5 is a picture of the aluminum electrodes fabricated by the self-aligned technique described above. The central dark line running from the top to the bottom of the figure is the top of the $LiNbO_3$ ridge.

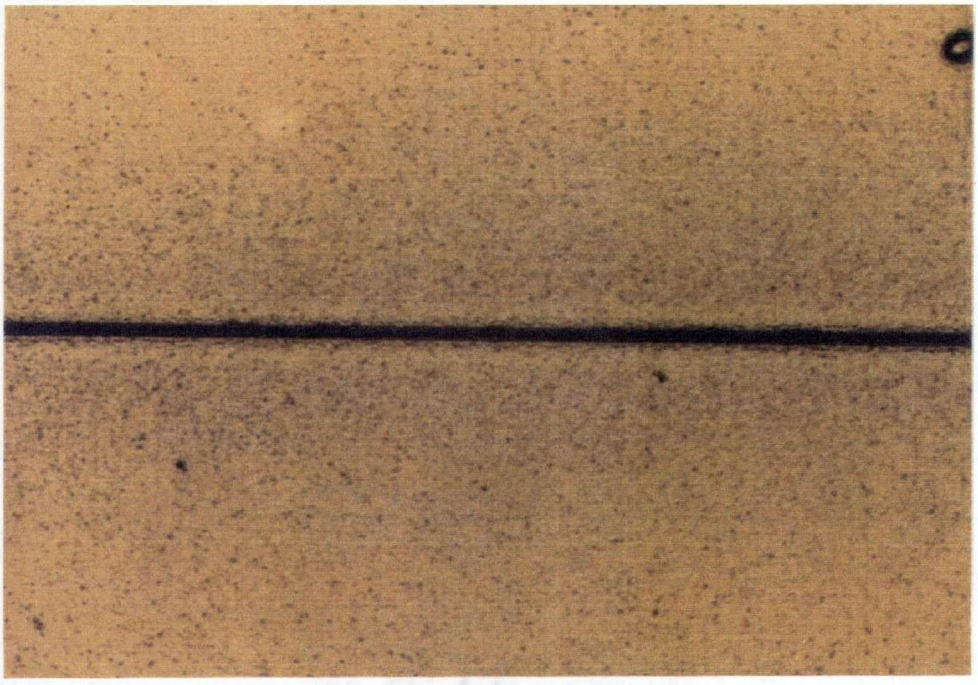

Figure 3.5: The aluminum electrodes of a ridge VIOWM formed by the self-aligned technique.

3.2.3 Cutting and Polishing

The individual VIOWMs were cut from the substrate using either a high speed diamond saw or a wire saw. The choice of the cutting method depended on the desired yield. When using the diamond saw the edge damage can be severe so that the waveguides must be cut into about 3 mm long sections. Using the wire saw the waveguides may be cut into 2 mm long sections. In both cases the final device is to be about 1 mm long.

The length of the device was kept short to minimize the losses due to absorption, scattering and optical field/metal electrode interactions. The drawback of a short device is that there is a relatively large amount of coupling due to bulk modes. Although a device about 1 inch long was fabricated most were between 1.6 mm and 0.8 mm.

The polishing jig consisted of two parts; the main body and the polishing plate. The main body had a large center screw that could be lowered to provide a backstop for the crystal being polished and a set screw to hold the center screw in place. The polishing plate consisted of a stainless steel plate about 1 mm thick (the thickness decreased with excessive grinding and polishing) with a 2 mm x 10 mm slot cut into its center. Figure 3.6 shows the polishing jig: the main body and the polishing plate.

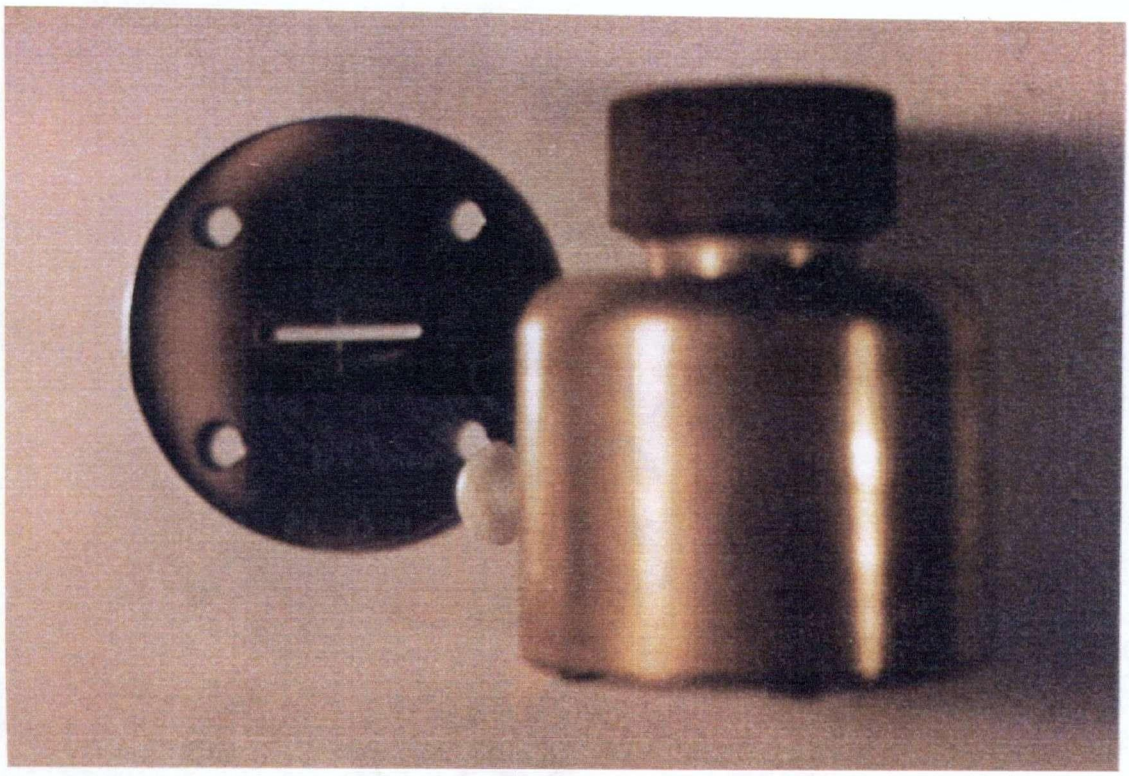

Figure 3.6: The polishing jig: the main body (right) and the polishing plate (left).

The samples were polished two at a time. The faces of the two bits of crystal containing the VIOWMs were epoxied together using a 5 minute epoxy. The sandwich thus formed was pressed together to remove excess epoxy from between the two. It is important to reduce the thickness of the epoxy layer so as to reduce the edge damage that results during the grinding process.

When the epoxy between the two samples had had time to set the sandwich was epoxied into the slot in the polishing plate of the polishing jig so that it protruded equally from both sides.

The protruding $LiNbO_3$ was then ground, using 600 grit grinding paper, until it extended about a quarter of a millimeter out from either side of the polishing plate. A second grind is done using 800 grit compound.

Polishing was done using a 1 μm alumina slurry until the edge damage was removed. The edge of the crystal was continually monitored, using a microscope, to determine when the edge damage has been removed. The final polish was done using a 0.05 alumina slurry.

Figure 3.7 shows the polished end face of such a sandwich for two ridge waveguide samples following the 1 μm alumina polish. The large light areas at the top and bottom of the picture are the $LiNbO_3$ substrates, the dark central region is the epoxy, the thin bright stripes are the aluminum electrodes. The central bump is the $LiNbO_3$ ridge.

The ridge height is about 0.4 times the width in this figure. One can clearly see that the aluminum electrodes climb up the sides of the ridge. Also the results of edge damage can be seen on the upper substrate.

Once both faces of both VIOWMs have been polished they were removed from the polishing plate by soaking them in hot Microstrip for about 5 min. Once they had been removed from the polishing plate they were again soaked in hot Microstrip until they came apart, about 1 hr.

Figure 3.8 shows a planar device that had been polished on both ends the interelectrode gap is seen to run from one end to the other. This device was about 1.6 mm long. Figure 3.9 shows the end of the device where the interelectrode gap was perpendicular to the polished end face.

Finally the excess $LiNbO_3$ could be removed from either side of the device by mounting it on a glass microscope slide and cutting it using a low speed diamond saw.

3.3 The Silicon V-grooves

The use of V-grooves anisotropically etched in Si substrates [59,60] for the alignment of optical fibers with in-diffused waveguides in $LiNbO_3$ provides a practical method of achieving efficient butt-coupling. The "flip-chip"

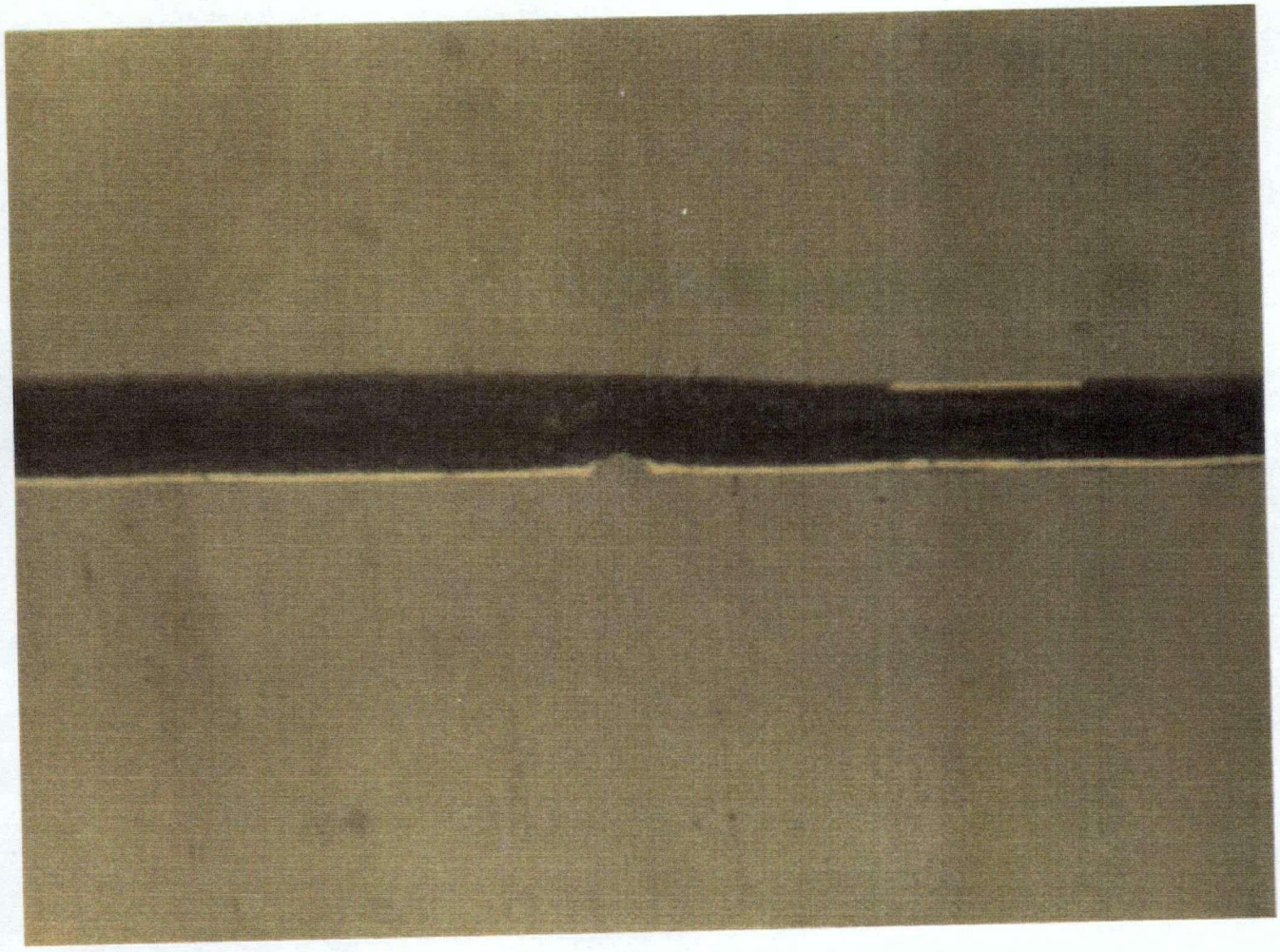

Figure 3.7: The endface of two ridge VIOWMs, epoxied together, after a 1 μm alumina polish.

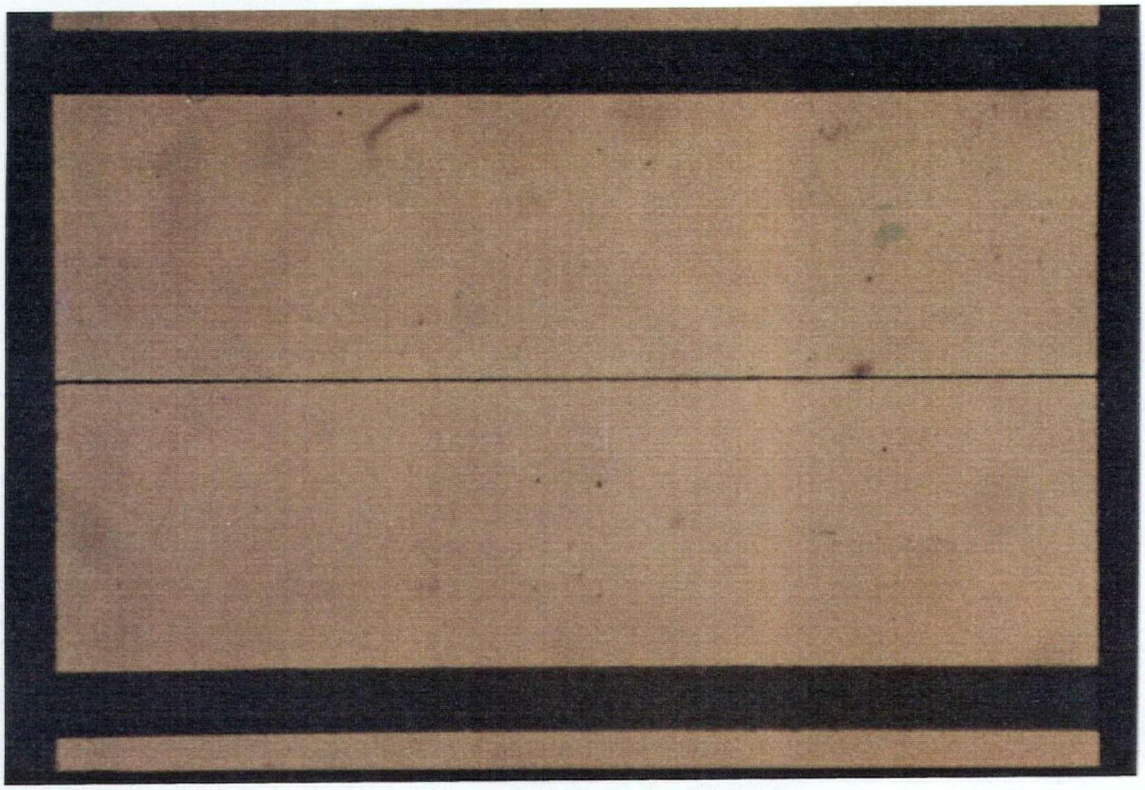

Figure 3.8: A planar VIOWM with the ends polished.

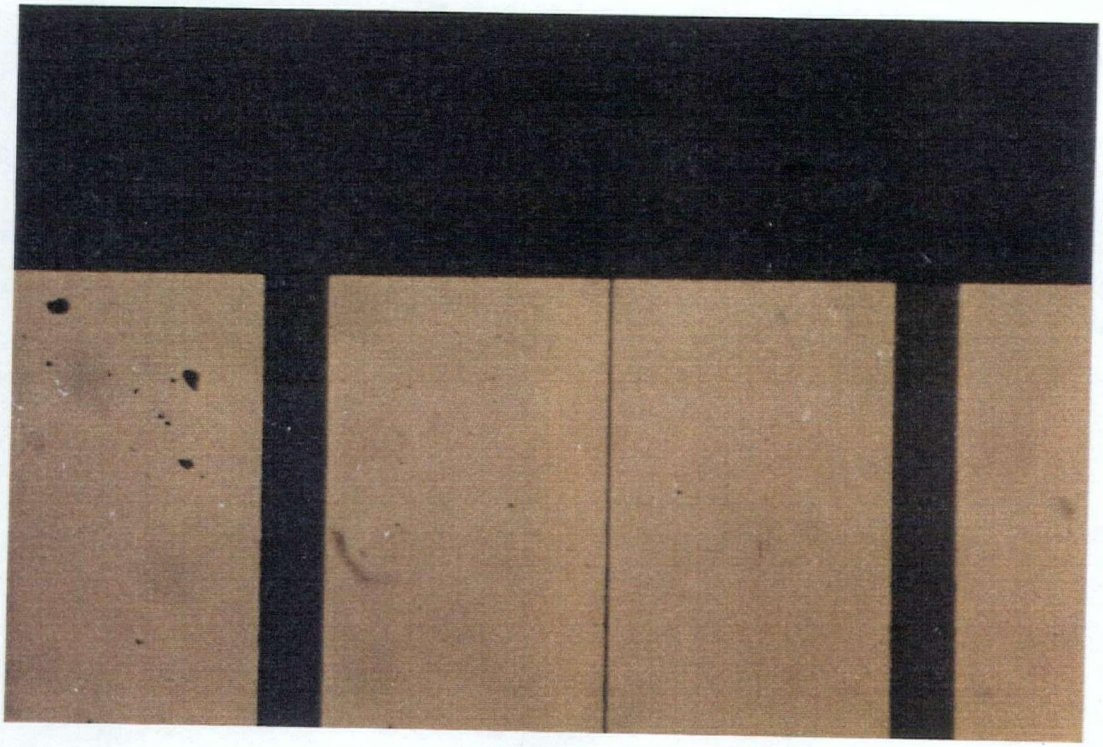

Figure 3.9: The polished end of a planar VIOWM where the interelectrode gap is seen to run perpendicular to the endface.

method of coupling between optical fibers and Ti:$LiNbO_3$ waveguides was first reported by Hsu and Milton in 1976 [21].

In this method a V-groove is etched in a (100) p-type silicon wafer. The depth of the V-groove is controlled so that an optical fiber lying in the V-groove has its core positioned at a height above the unetched surface of the wafer that will result in efficient coupling of light to an integrated optic device. The depth control is obtained by taking advantage of the anisotropy of the etch rate of Si which is about 35 times greater in the (100) direction than it is in the (111) direction for the etchant described below. Electrodes are formed on the unetched portions of the wafer to provide electrical contact with the electrodes of the integrated optics device which is placed "upside down" on the wafer containing the V-grooves. In this way the optical fiber and integrated optics device are located so as to facilitate a high degree of overlap between the optical fields in both waveguides when they are butted together.

The variables critical to the vertical alignment of an optical fiber and an integrated waveguide, by this method, are the outer diameter of the fiber, the core-cladding concentricity and the V-groove depth. It would be necessary to control each of these variables to sub-micron tolerances (less than 1% in each case) if one were to predictably

obtain a certain degree of coupling, therefore it is desirable to have a method of varying the height of the fiber above the surface of the Si wafer. Sheem and Giallorenzi [61] accomplished this using a tapered fiber in a second, deeper V-groove. In this method the height of the fiber being aligned was controlled by sliding the second tapered fiber in the deeper V-groove beneath it. In the present work an array of 13 V-grooves was used each of which is of a different depth, increasing by 1 μm from one groove to the next.

The fabrication of the V-grooves consists of 6 basic steps: oxide growth, electrode fabrication, oxide sputtering, V-groove window fabrication, V-groove etching, and oxide removal.

In order to get repeatable results it is necessary to start with a clean wafer. Therefore the fabrication was preceded by cleaning the wafer using the well known RCA process [62].

A thermal oxide was grown on the wafer for two reasons. Primarily it is not attacked by the etchant used to create the V-grooves, therefore it can act as the V-groove mask fixing the width of the windows and thereby the depth of the V-grooves, and secondarily it serves to isolate the electrodes electrically from the substrate. The oxide was grown to a thickness of 500 nm. To do this an oven was heated to 1100°C with an O_2 flow of 1 l/min. The slices

were introduced to the oven and allowed to heat up for 5 min. A flow of 1.6 l/min. of H_2 was started giving an O_2+H_2 "wet" atmosphere. Wet growth is approximately an order of magnitude faster that dry growth (O_2 only) [63]. After 80 min. the H_2 flow was stopped and 5 min. after that the O_2 flow was also stopped. There followed a 20 min flow of N_2 at 1 l/min.

The electrodes on the V-grooves were formed using a lift-off technique that was identical to that used to form the electrodes of the planar VIOWM (section 3.2.1). The reason that the electrodes were formed at this stage was because if the V-grooves were formed first the application of photoresist was uneven in the intergroove regions making the lift-off procedure uncertain.

A second layer of SiO_2 was deposited at this point to protect the electrodes from the V-groove etchant. This layer was deposited in the Perkins-Elmer sputtering system and was about 700 nm thick.

Windows were etched in the SiO_2. Photoresist was applied to cover those areas that were not to be etched (including the back of the wafer). The SiO_2 was then etched in buffered HF for 20 min. followed by a rinse in DI water. The HF etch was intended to be a bit too short to completely etch the grown oxide. This was to avoid over etching which would result in widening the V-grooves. The final layer was removed by a 20 min. CF_4 plasma etch performed as described

in section 3.2.2 for the Ti etch. Finally the photoresist was removed.

The V-grooves were etched in a solution of KOH (20% by weight), DI water (64%) and 2-propanol (16%). The solution was heated to 85°C in a beaker with a condenser. The wafer was immersed for 85 min. The wafer was then removed and was blown dry with N_2.

The sputtered oxide layer protecting the electrodes was then removed by etching for about 5 min. in buffered HF. This was followed by a rinse in DI water and blow drying with N_2.

Figure 3.10 depicts the entire V-groove fabrication process.

Since the device was to act as a front-end switch, in which it is placed between a laser and an optical fiber, controlling the light coupled from the laser to the fiber by the application of voltage to its electrodes, the V-grooves were designed so that the VIOWM would slightly overhang one end of the Si wafer with the V-groove on the other side.

3.4 Device/Optical Fiber Alignment

The coupling between a VIOWM and an optical fiber was discussed in section 2.6. It was pointed out that the theoretical development of the coupling coefficient was

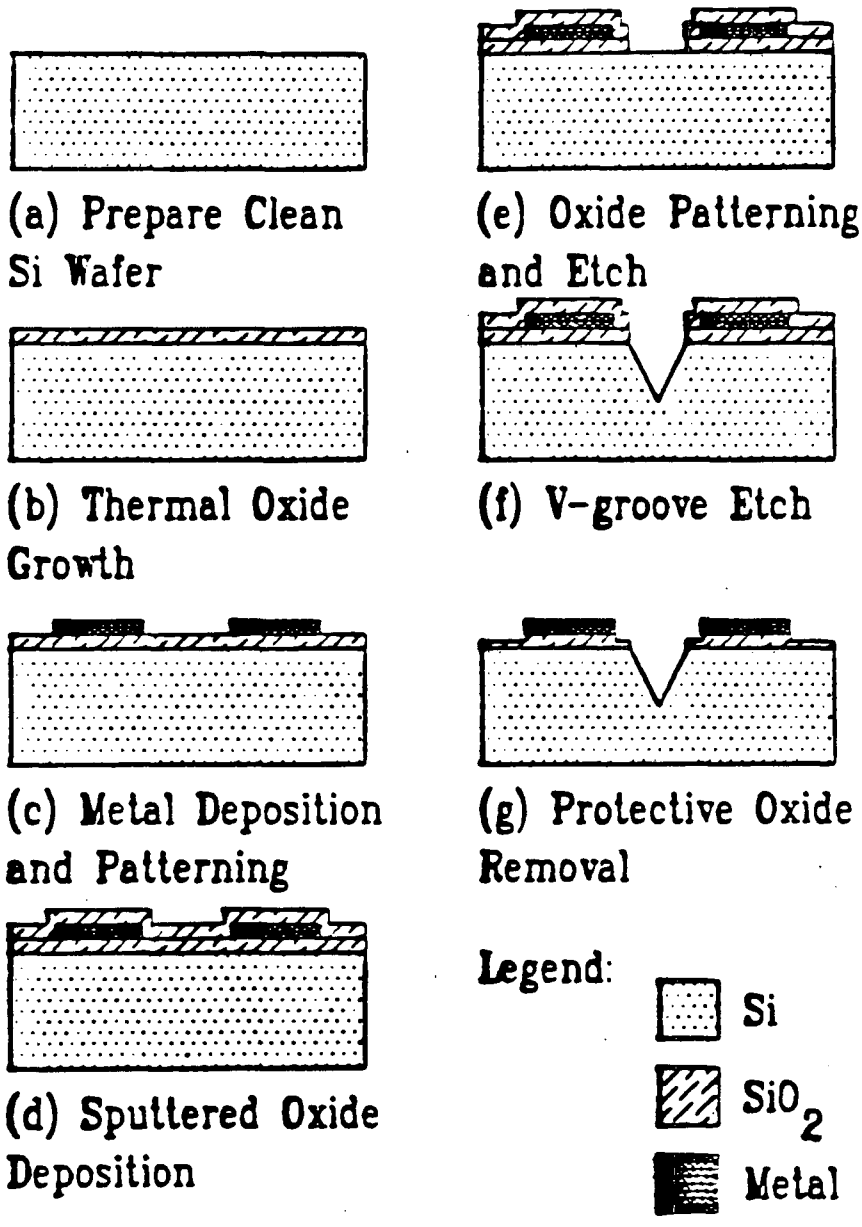

Figure 3.10: The V-groove fabrication process.

insensitive to whether light was coupled from the VIOWM to the fiber or from the fiber to the VIOWM. Therefore it was possible to align the device with the light propagating in the reverse direction from that intended for the actual operation i.e. with light from the fiber coupled into the VIOWM.

First a length of optical fiber was prepared by removing the plastic coating from both ends and then cleaving them. The output of a laser was then focused on one of the cleaved end faces while monitoring the output at the other. Cladding modes were removed by a series of tight, about 1 inch in diameter, loops in the fiber. In the case that the fiber was multimode, having been designed for monomode operation at a longer wavelength, these loops also served to strip the higher order guided modes.

The back of the sample VIOWM was cemented to a pin which was attached to the boom of a crane mounted on a two axis piezoelectric micropositioner. The sample hung upside down with its electrodes facing the floor.

The Si wafer containing the V-grooves was mounted right side up, so that its electrodes were facing the ceiling, on a stage that could be heated to the eutectic temperature of AuGe. The surfaces of the wafer and the VIOWM were aligned by placing the two in contact and heating the stage just enough to soften the cement holding the VIOWM to the pin.

The output end of the optical fiber was laid in a V-groove and a small weight was placed atop it hold it in place. The sample VIOWM was positioned so as to be in contact with the end of the fiber. A signal was applied to the electrodes on the wafer containing the V-grooves and the sample's position was adjusted until it was felt that the best coupling for that groove had been obtained. If it was necessary the surfaces were realigned by heating following rotations. This procedure was repeated from groove to groove until the groove giving the best coupling was found.

Once the best coupling was obtained a permanent bond was formed by heating the stage to the eutectic temperature of AuGe, 363°C. During the heating cycle the cement between the VIOWM and the pin was oxidized and the two were easily separated after the stage had cooled. The bond was reinforced by the application of droplets of cyano-acrylate glue to both sides of the crystal. The fiber was also bonded in place by applying a drop of the same glue on the fiber at the far end of the V-groove away from the butt couple.

Figure 3.11 shows the V-groove array, fiber, VIOWM, pin and probes during the alignment procedure.

Figure 3.12 shows the V-groove array, fiber, VIOWM, probes and input objective after the alignment and permanent bonding procedure.

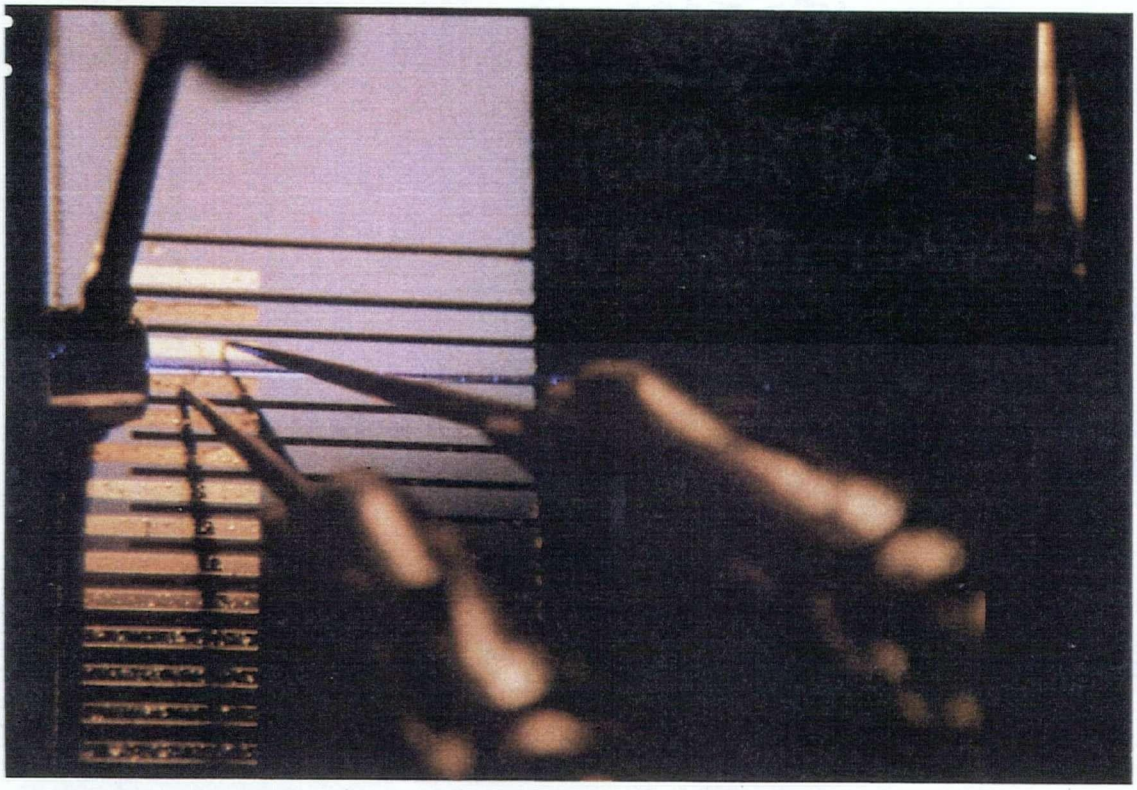

Figure 3.11: The V-groove array, fiber, VIOWM, pin, and probes during the alignment procedure.

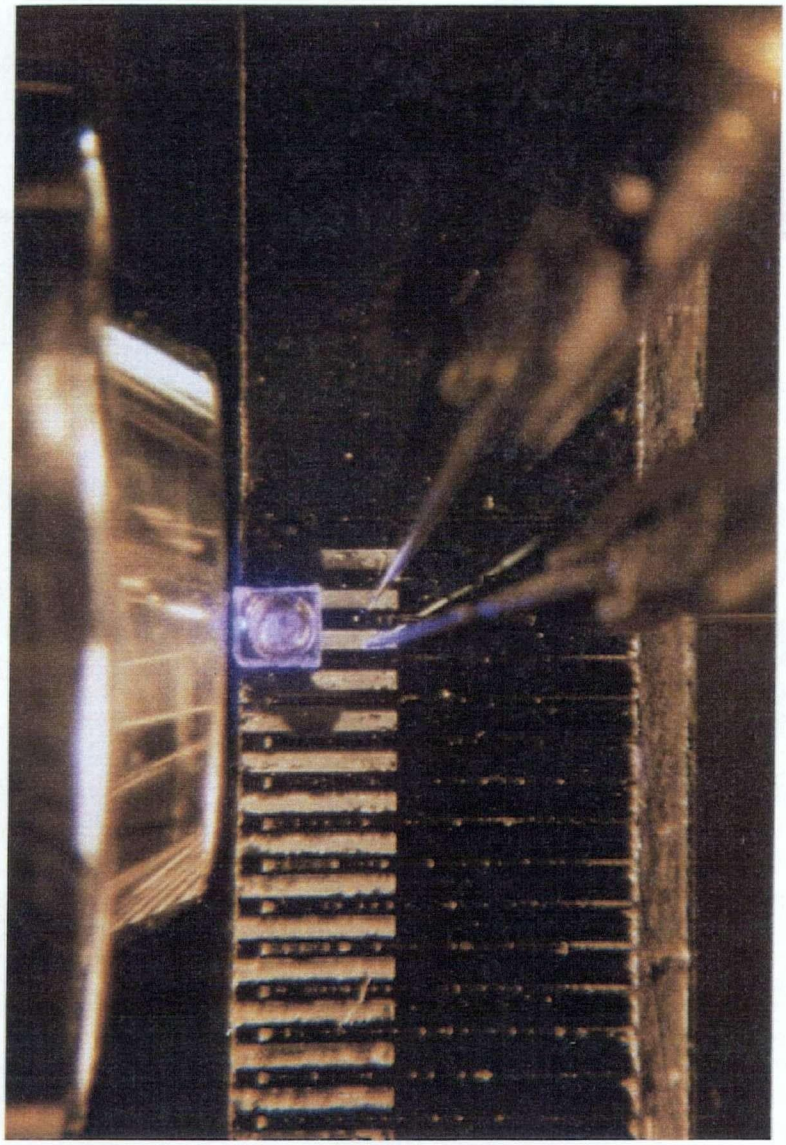

Figure 3.12: The V-groove array, fiber, VIOWM, probes, and input objective after the alignment and permanent bonding procedure.

The crystals shown in figures 3.11 and 3.12 are about 1 mm on a side.

Chapter 4

RESULTS

4.1 Introduction

The results, both calculated from the model and measured, for the planar VIOWM are presented in section 4.2 and the results for the ridge VIOWM are presented in section 4.3. Section 4.4 contains the results of measurements on the VIOWM permanently mounted on the Si V-grooves with an optical fiber attached. Finally section 4.5 provides a discussion of the various results obtained.

To predict the behavior of the VIOWM device with optical fibers it was assumed that the fibers have circularly symmetric optical field distributions and that the nominal width parameters were $w_{yf} = w_{zf} = 1.5$ μm.*

---

* This was close to the value given to us by the engineers at MacDonald Dettwiler and Assoc. for the width of the mode of the optical fiber they use in the FIRE 9000 b/w optical image recorder. They measured the half width at $1/e^2$ of the peak power to be ~ 2 μm.

Other fibers could, of course, support modes with different mode widths.

The numerical integrations were done using adaptive techniques for which the accuracy could be specified. Turbo Pascal was used on an IBM AT compatible with an 80287 math coprocessor. The integration routines were taken from the Turbo Pascal Numerical Methods Toolbox. The accuracy was specified to be to eight significant figures. The accuracy of the routines were tested on Hermite-Gaussian functions and found to be within the specified tolerance. The limits of integration were set to 5 times the width parameter of the trial function in both the y and z-directions. This ensured that the error incurred by neglecting that part of the integral that was outside of the limits of integration would be less than the tolerance.

4.2 The Planar VIOWM

The calculated results from the model for the planar VIOWM are presented in section 4.2.1 and the measured results are presented in section 4.2.2.

4.2.1 Calculated Results

Figures 4.1 and 4.2 are topographical plots of the width parameters, w_{yv} and w_{zv}, as functions of the applied voltage and interelectrode gap width for a VIOWM for light with a wavelength of 442 nm. Figures 4.3 and 4.4 are plots of the width parameters for 633nm radiation. These results indicate that the width parameters decrease with increasing voltage, with decreasing gap width and with decreasing wavelength. In other words the optical field distribution of a guided mode becomes more highly confined to the high refractive index region in the vicinity of the interelectrode gap as one applies an increasing voltage to the electrodes and this effect is greater for smaller gaps as well as at shorter wavelengths.

The fact that increasing voltage will result in higher optical confinement is to be expected. As the change in the refractive index distribution due to the application of voltage to the electrodes becomes larger the turning point of the mode moves closer to the interelectrode gap. This is because the change in direction of a ray is proportional to the gradient of the refractive index distribution [19] and the change in the refractive index is directly proportional to the applied voltage. This argument is equally well applied to the increase in confinement with decreasing

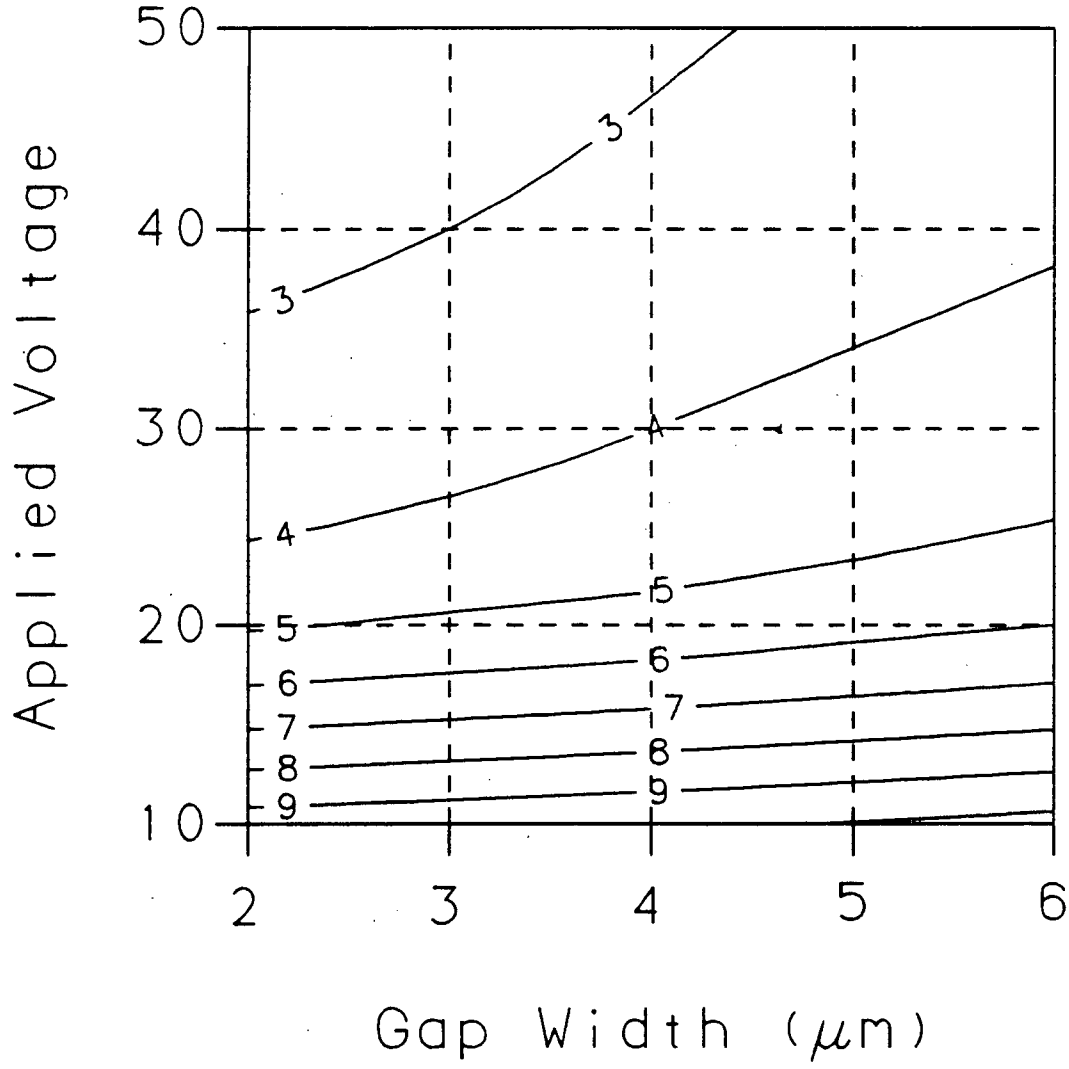

Figure 4.1: A topographical plot of w_{yv} for λ_o = 442 nm.

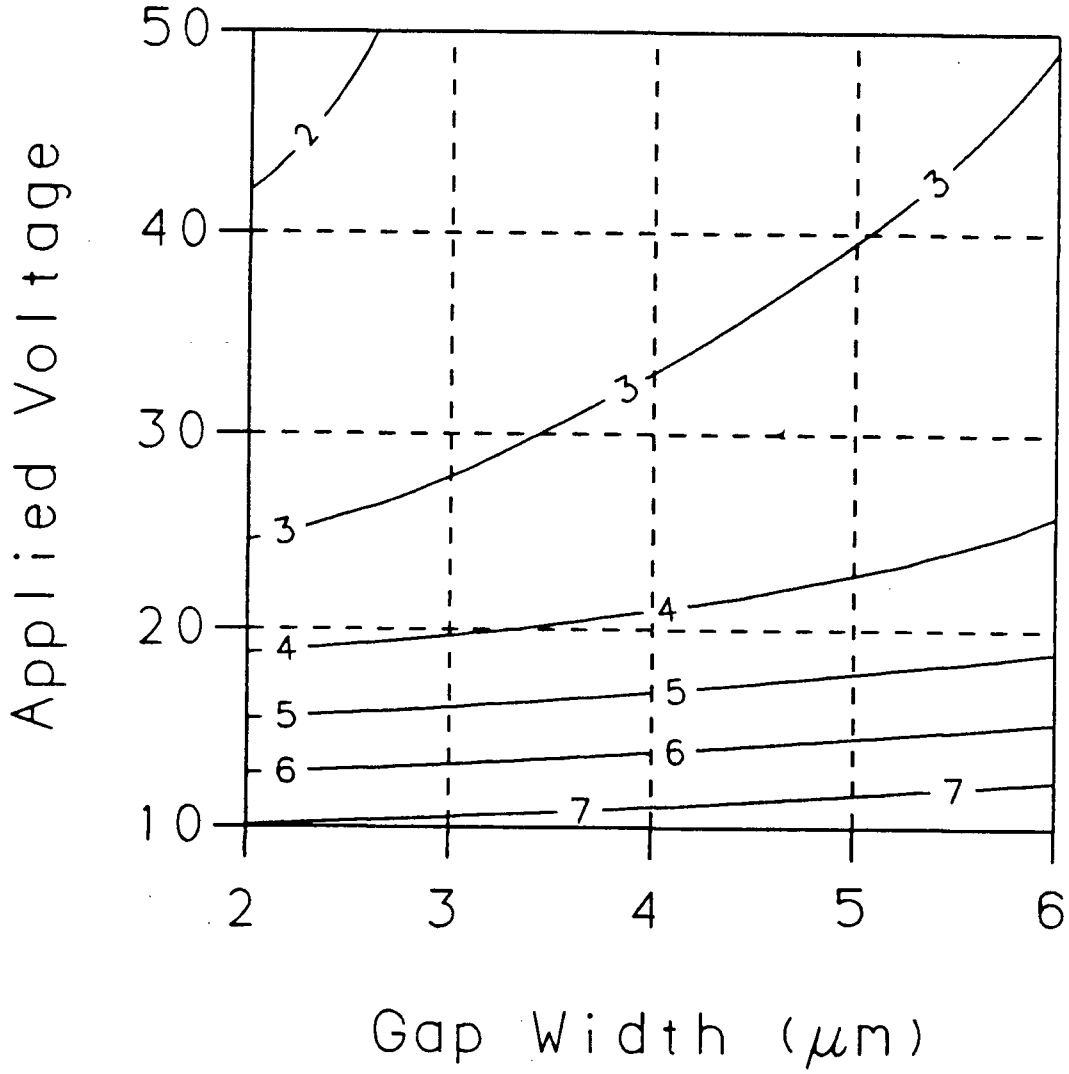

Figure 4.2: A topographical plot of w_{zv} for λ_o = 442 nm.

Contours of constant w_{yy}

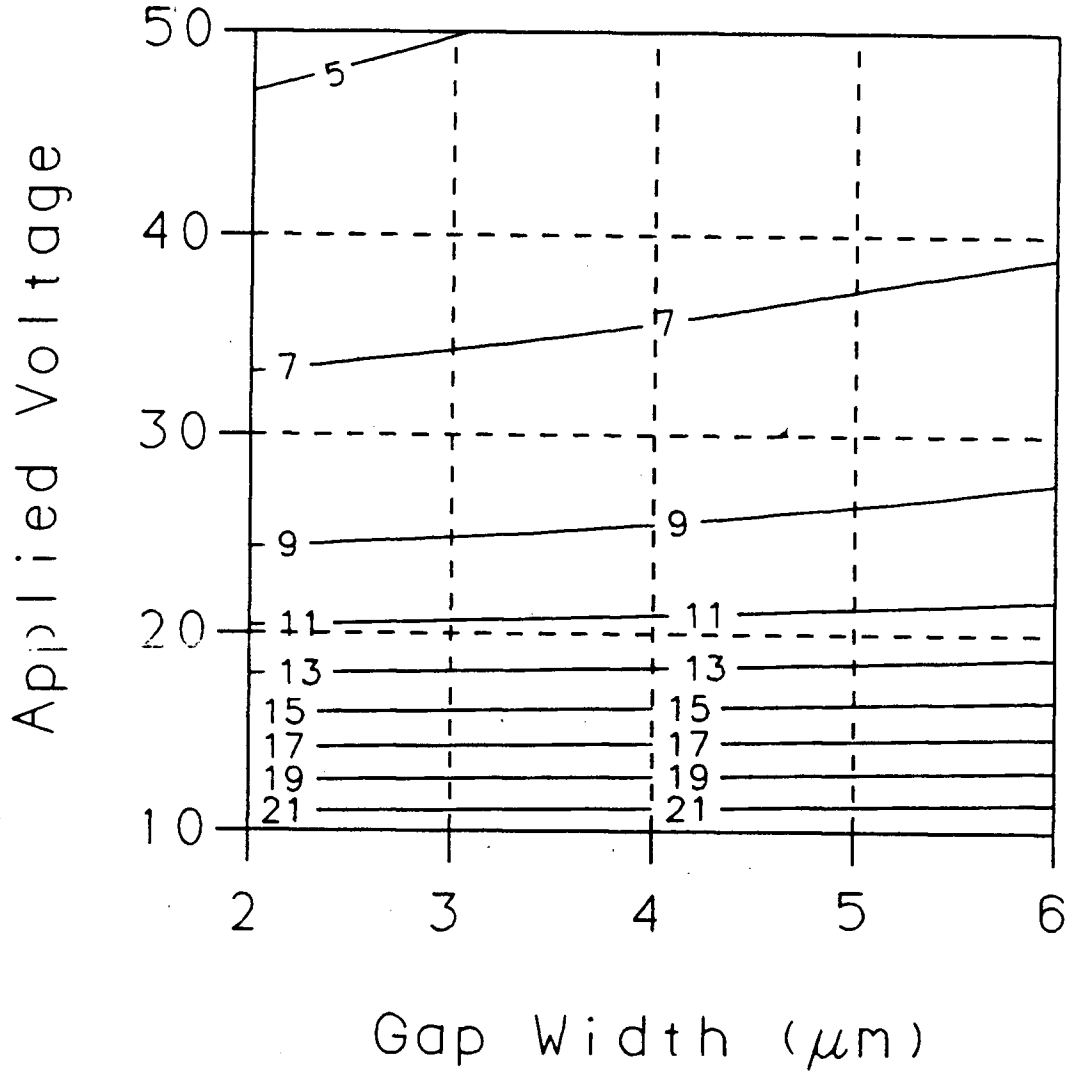

Figure 4.3: A topographical plot of w_{yy} for λ_o = 633 nm.

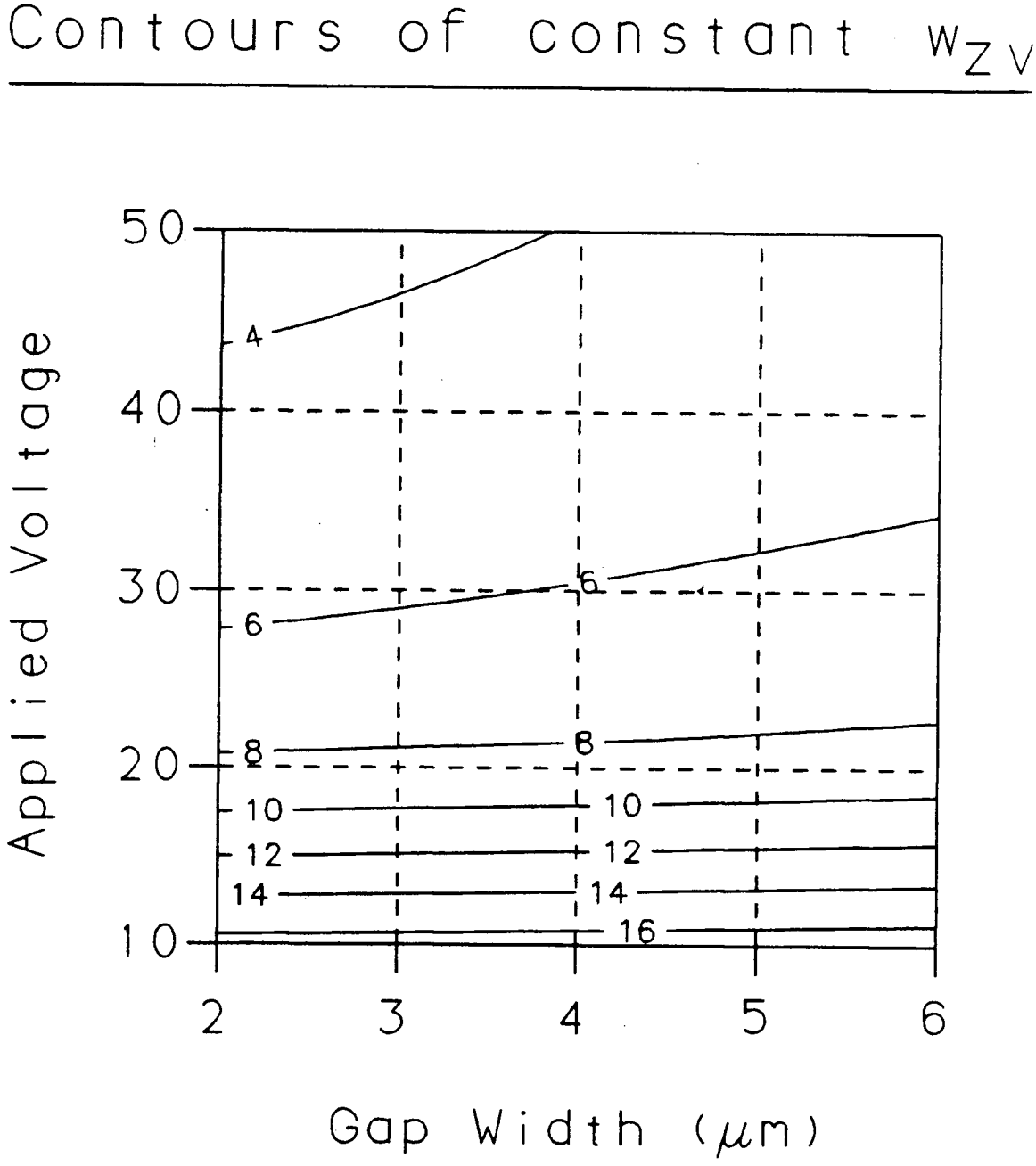

Figure 4.4: A topographical plot of w_{zv} for λ_o = 633 nm.

interelectrode gap width for the electric field in the substrate is inversely proportional to the gap width. Also the change in the refractive index distribution is directly proportional to the cube of the refractive index of the substrate which in $LiNbO_3$ tends to increase as one approaches the absorption edge [64].

The location of the fiber relative to the input of the VIOWM is an important factor in determining the coupling coefficient. Here, in any practical switching application the location of the optical fiber will depend on the intended application and the range of applied voltages. The optimum position for the fiber in the z-direction will always be at b = 0. However, the location of the fiber in the y-direction must be determined by the application.

In the case that the intended application of the VIOWM is as a digital switch situated between two single-mode optical fibers one might want to ensure that the maximum amount of power is transferred from the input fiber to the output fiber for a particular applied voltage or one might want to ensure that the output power is insensitive to slight variations in the applied voltage. Both of these situations can be achieved by judiciously choosing the fiber location.

In figures 4.5 and 4.6 are plotted the coupling coefficient T as a function of applied voltage. For these figures it has been assumed that the optical fibers are

located so as to maximize the power transfer for applied voltages of 30 V and 50 V respectively. In this case the VIOWM is assumed to have a 2 μm interelectrode gap and the wavelength of the light is taken to be 442 nm. It is apparent from both figures that a greater degree of coupling will occur at voltages greater than either 30 V, in figure 4.5, or 50 V, in figure 4.6, however the coupling achieved at these voltages are the greatest that may be achieved for these voltages.

In figures 4.7 and 4.8 is plotted the coupling coefficient T as a function of voltage for the optical fibers positioned so that the maximum coupling that can be obtained for 30 V and 50 V applied to the electrodes for an interelectrode gap width of 4 μm and 442 μm light.

In figure 4.5 the actual peak value of the coupling occurs at - 37 V rather than 30 V. This indicates that if the device were operated at 37 V then the coupling coefficient would vary by only a few percent for a larger change in the applied voltage. Also figures 4.5 and 4.7 show that for applied voltages of ~ 37 V and 43 V respectively the coupling coefficient T is stationary. The coupling coefficient remains within 5% of its maximum value for changes exceeding ±7 volts in figure 4.5 and for even greater variations in figure 4.7.

The effect described above would also be useful in rendering the VIOWM less sensitive to changes in the

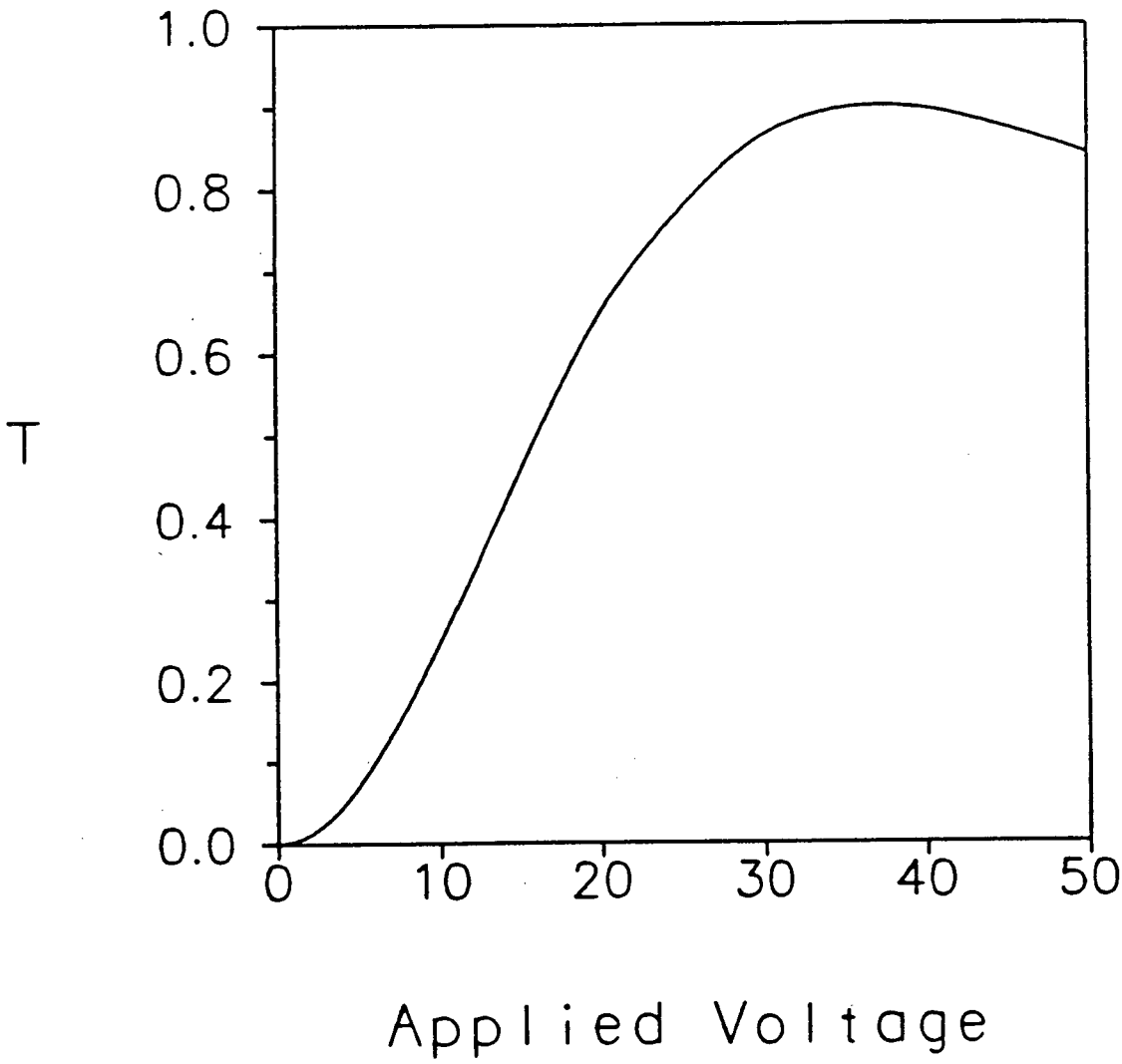

Figure 4.5: The coupling coefficient T vs. voltage for g = 2 μm where the coupling at 30 V is maximized.

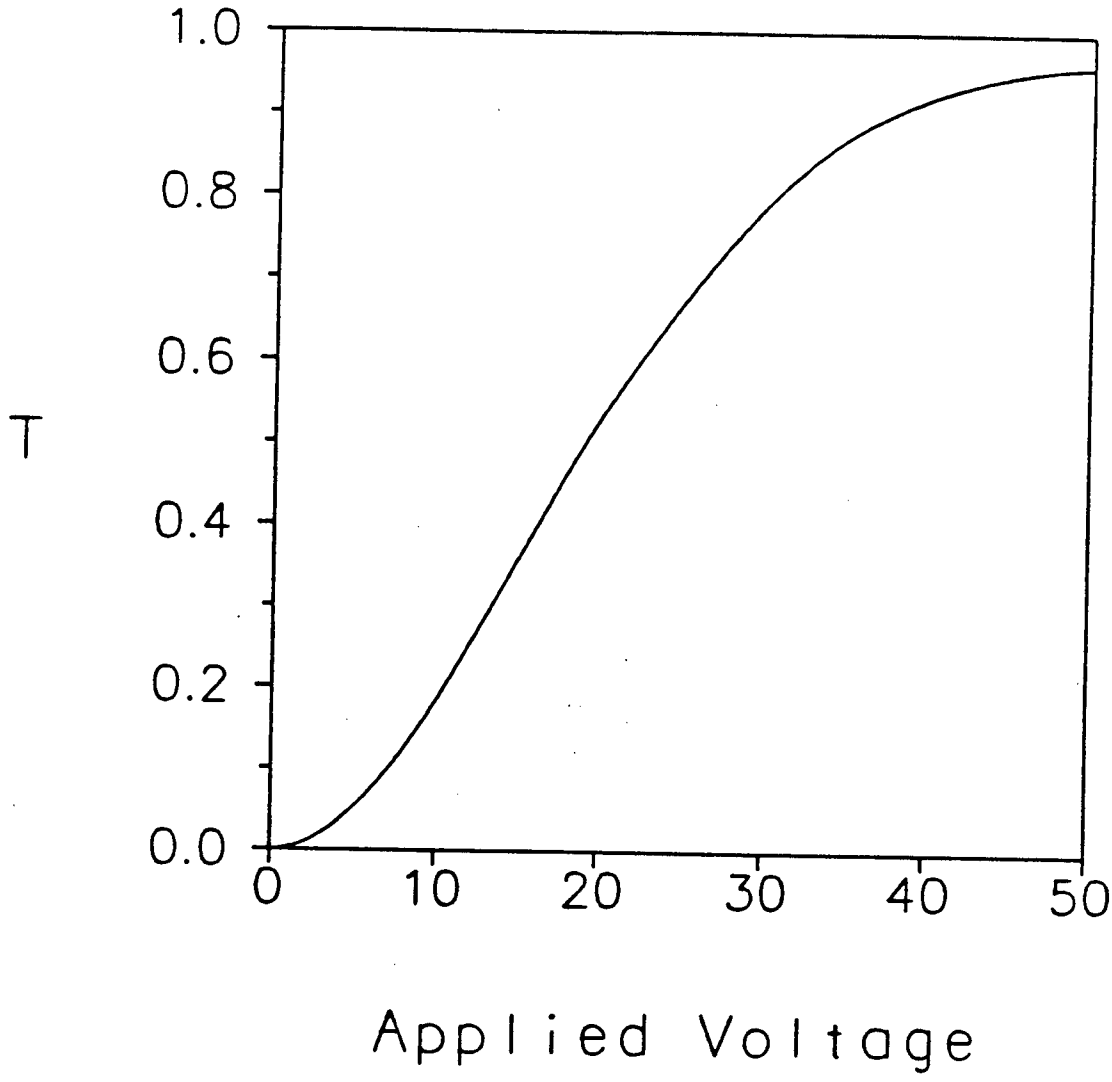

Figure 4.6: The coupling coefficient T vs. voltage for g = 2 μm where the coupling at 50 V is maximized.

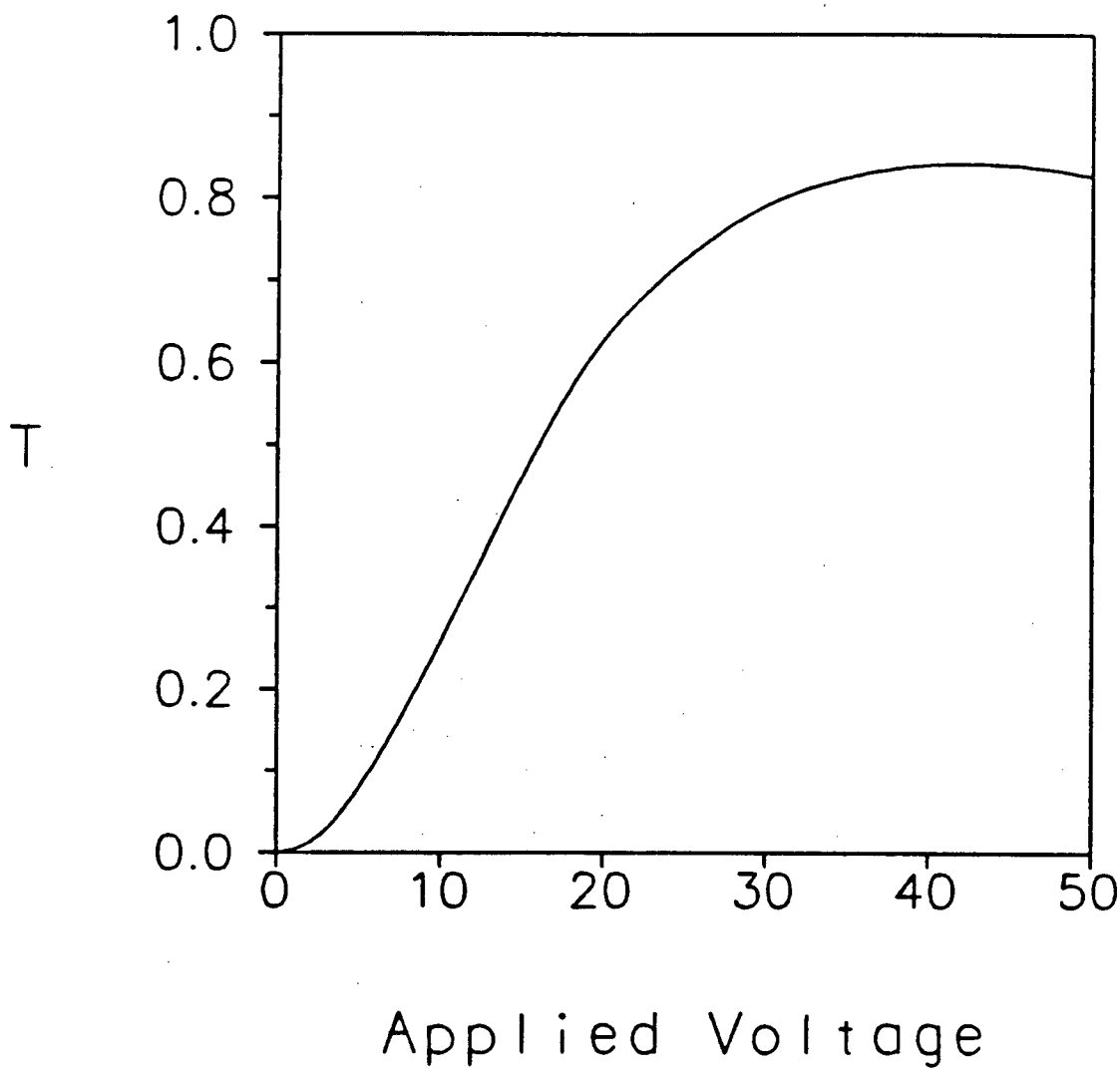

Figure 4.7: The coupling coefficient T vs. voltage for g = 4 μm where the coupling at 30 V is maximized.

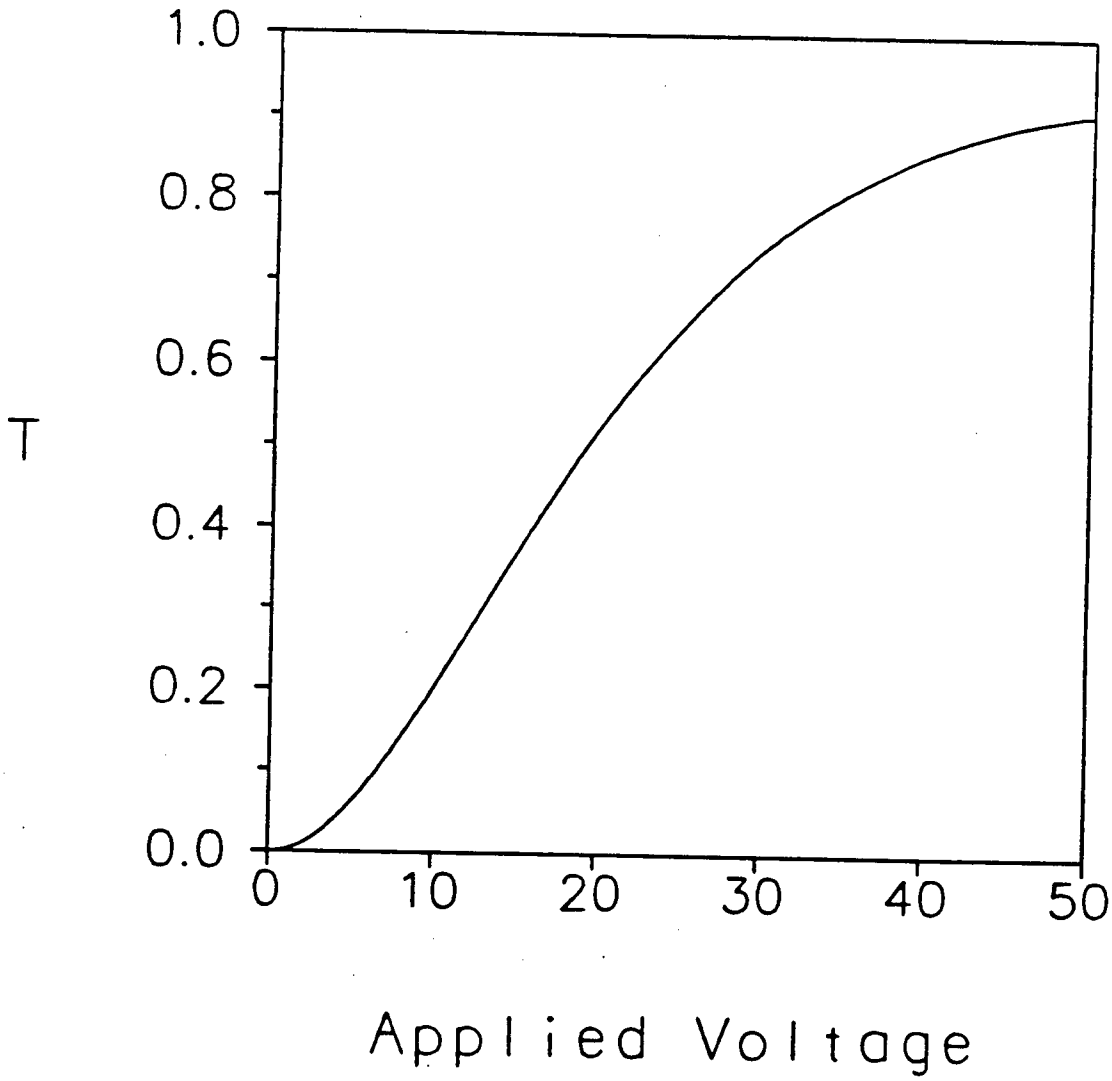

Figure 4.8: The coupling coefficient T vs. voltage for g = 4 μm where the coupling at 50 V is maximized.

refractive index profile brought about by the photorefractive effect.

In figure 4.9 are plotted the optimum fraction of power transfer that can be obtained for a planar VIOWM for light with a wavelength of 442 nm as a function of both voltage and interelectrode gap width. The fraction of power transfer is given by T^2. From this figure one can see that it is possible to obtain -3dB power transfer between an optical fiber that supports a mode with width parameters $w_{yf} = w_{zy} = 1.5$ μm and a VIOWM with an applied voltage of only 20 V. Extrapolating the curves presented in figure 4.9 shows that at smaller interelectrode gap widths it would be possible to obtain even better power transfer. Calculations for interelectrode gap widths less than 2 μm were not performed because a buffer layer thickness of 5% of the interelectrode gap width would be less than 1000 Å which would not result in sufficient attenuation of the evanescent field of the guided modes.*

Finally the use of the VIOWM as a small signal linear modulator between two optical fibers is considered. If the power is to be modulated in a linear fashion then the power in the output fiber, P_{out}, will be related to the power in the input fiber, P_{in}, by

---

* See chapter 2 section 2.3.1.2.

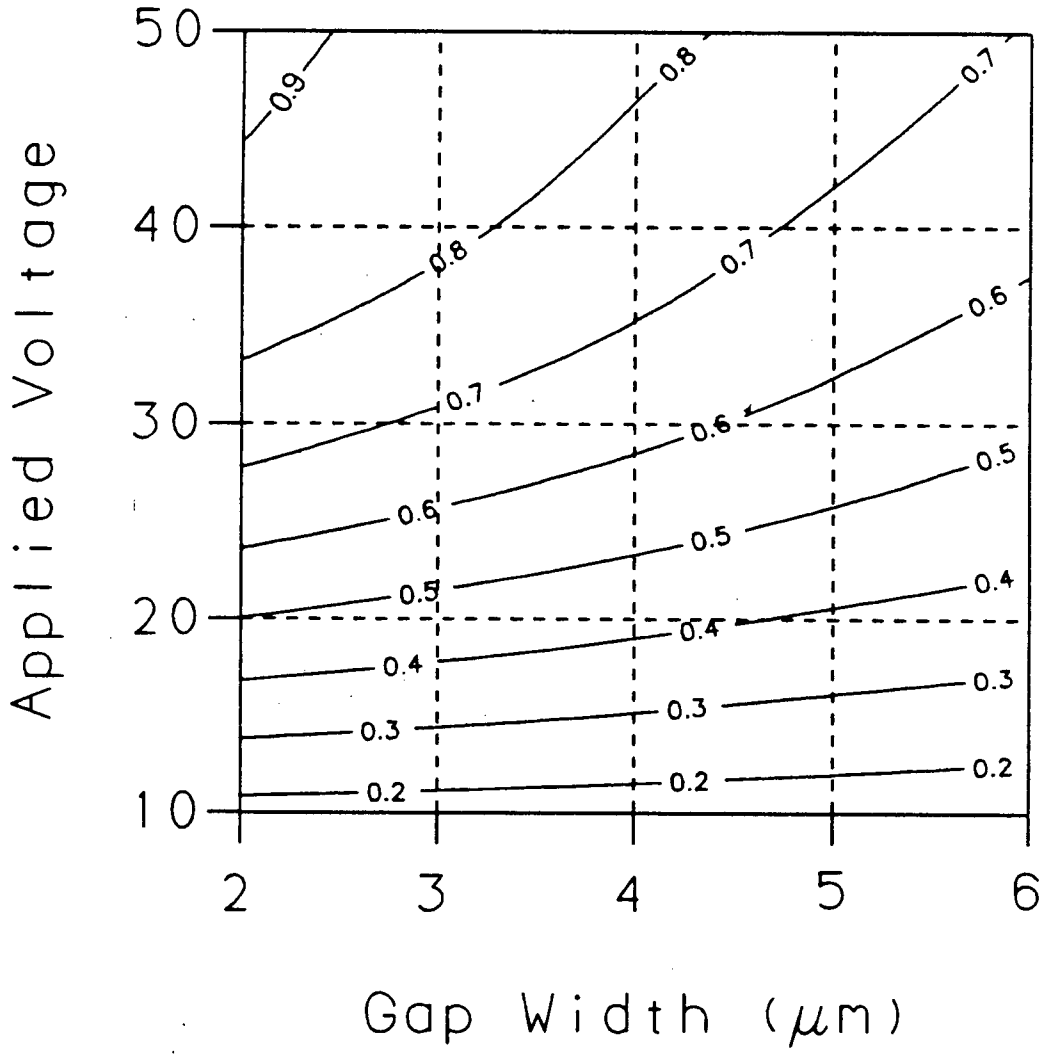

Figure 4.9: The optimum power transfer T^2 as a function of applied voltage and interelectrode gap width.

$$P_{out} = T^2_{in} T^2_{out} P_{in}$$

where T^2_{in} is the fraction of power transfer to the VIOWM at the input and similarly T^2_{out} is the fraction of power transfer from the VIOWM at the output. The input and output fibers could, of course, be located independently. For example one could be located so that the variation in the power transfer was minimized for a particular voltage and the other could be located at the point of steepest descent for the same voltage. Another possibility could be to locate both of the fibers to have the same amount of power transfer at the same voltage in which case the relation between the output power and the input power becomes

$$P_{out} = T^4 P_{in}$$

where T is the coupling coefficient at either the input or the output. In figures 4.10 and 4.11 are plotted T^4 for the cases in which both optical fibers are located so as to achieve the optimum coupling coefficient for a VIOWM with a 2 μm interelectrode gap for a wavelength of 442 nm when 30 V and 50 V applied to the electrodes respectively. As can be seen both figures indicate that there is a linear region in the transfer curves. In figure 4.10 the linear region appears to extend from an applied voltage of ~ 22 V to ~ 26 V in which the fraction of the power transferred goes from ~ 0.25 to ~ 0.55. In this case the appropriate bias voltage

would be ~ 24 V with a dynamic range of 4 V. Similarly in figure 4.11 the linear range extends from ~ 25 V to ~ 35 V and the fraction of power transferred goes from ~ 0.2 to ~ 0.6. Here an appropriate bias voltage would be ~ 30 V with a dynamic range of 10 V.

4.2.2 Measured Results

The apparatus (figure 4.12) consisted of a laser, a 40x objective, an optical fiber, the VIOWM under test, a 10x objective (acting as a projector), a polarizer, a chopper, and an aperture and a detector. The light, λ_o = 442 nm, was coupled into the fiber, with cleaved ends, using the 40x objective. The light was polarized in two planes at right angles. The fiber was wrapped on a spool. It was long enough for any cladding modes to be stripped. A loop, about 1 inch in diameter, was put in the fiber just before the output end to remove any loosely guided modes. This gives an output spot consisting primarily of the lowest order HE_{11} mode of the fiber. The polarization state at the output of the fiber was not known; however, upon monitoring the output of the fiber with a polarizer placed between the output and a detector the power was seen to vary over time by only a few percent (figure 4.13). The fiber was mounted on a three axis micropositioner with rotation in the vertical and

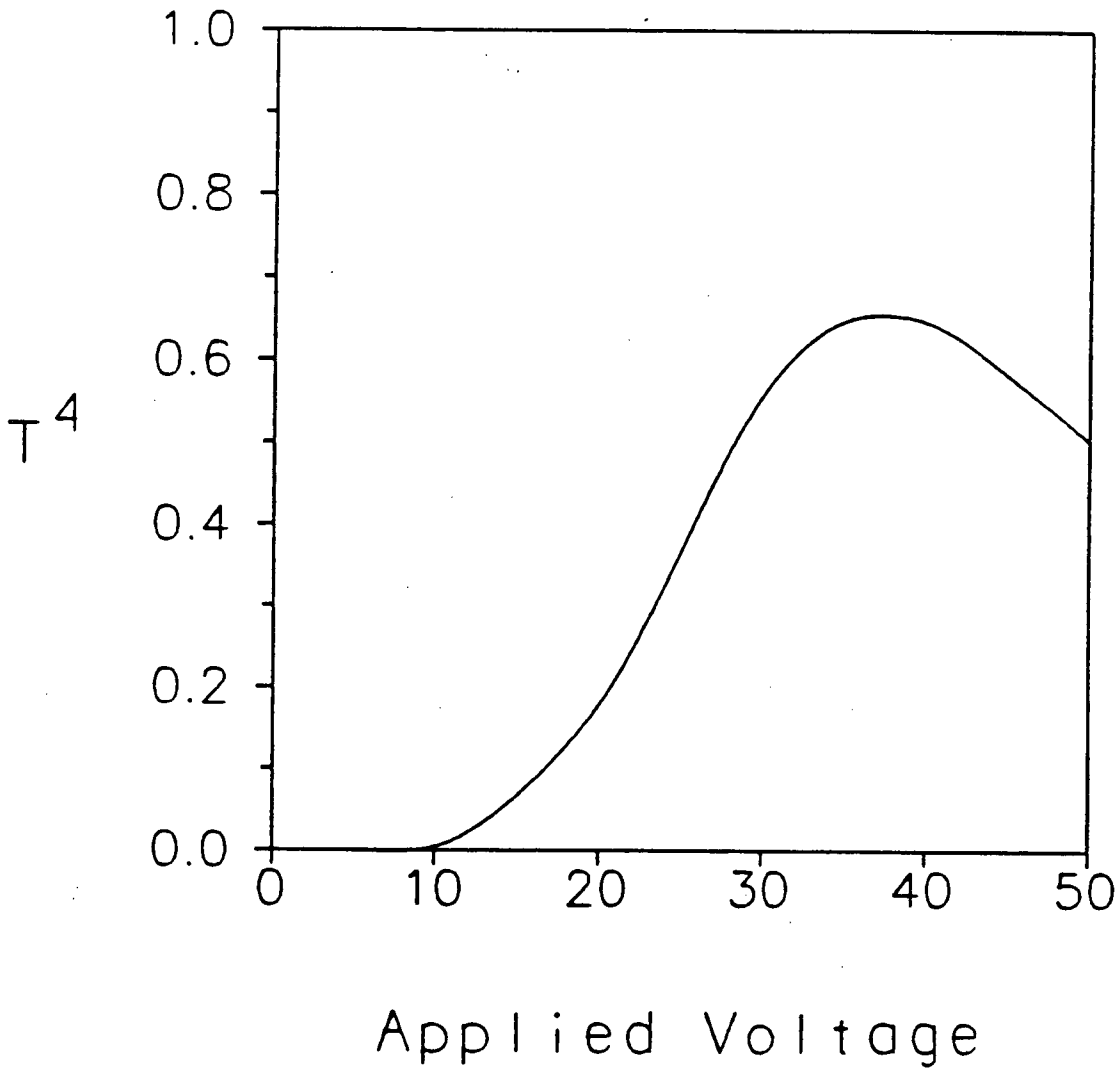

Figure 4.10: The power transfer T^4 between two optical fibers where the coupling at 30 V is maximized.

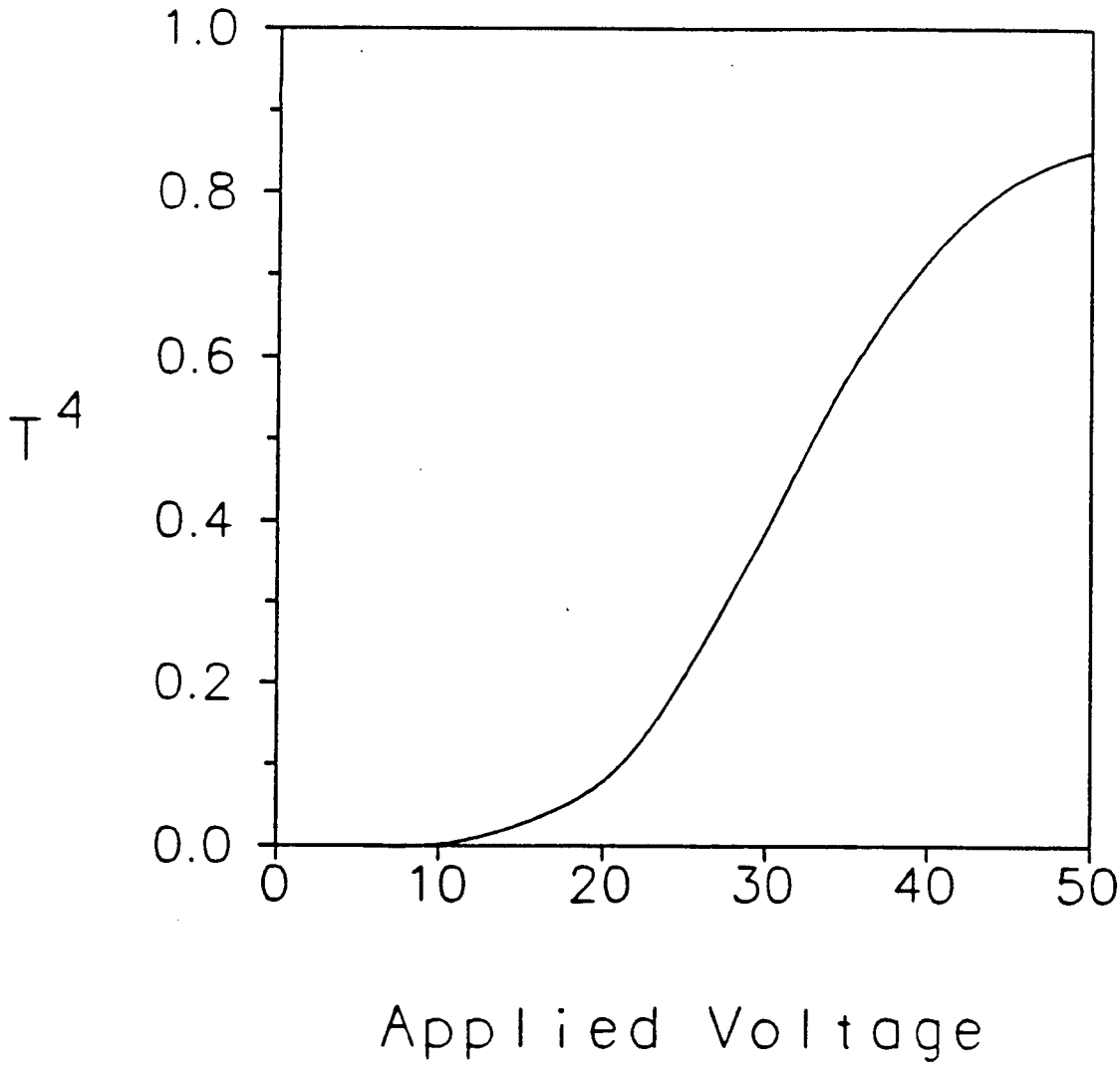

Figure 4.11: The power transfer T^4 between two optical fibers where the coupling at 50 V is maximized.

horizontal planes and thus could be aligned with the input face of the VIOWM under test. The stage holding the VIOWM was rigid. The output objective was also mounted on a three axis micropositioner. The polarizer was placed between the output objective and the aperture as was the chopper.

When light at the output of a VIOWM is focused upon an aperture the power transferred to the detector will depend on the shape and size of the aperture and the shape and size of the projected optical field distribution at the aperture. If the aperture is circular then the overlap is that between the optical field distribution of the guided mode and the rect(r/2c) function.* Since the transmission of the rect function is 1 in the region of the total transmission and 0 otherwise its effect is to set limits on the region of the projected image that is interrogated. If the aperture is large enough it will pass the majority of the power in the projected image of the optical field distribution for sufficiently high voltages and its effect on the measurements may reasonably be ignored. It is, however, included as it blocks much of the power in the bulk modes which would otherwise be collected by the detector. Still some of the power in the bulk modes is collected resulting

---

* A rect function is a two dimensional step function. The rect function is equal to 1 for $r \leq c$ and 0 otherwise where c is the radius of the aperture. See Collier, Burckhardt, and Lin [65] p. 94. This function is also referred to as the circ(r) function by Goodman [66] p. 14.

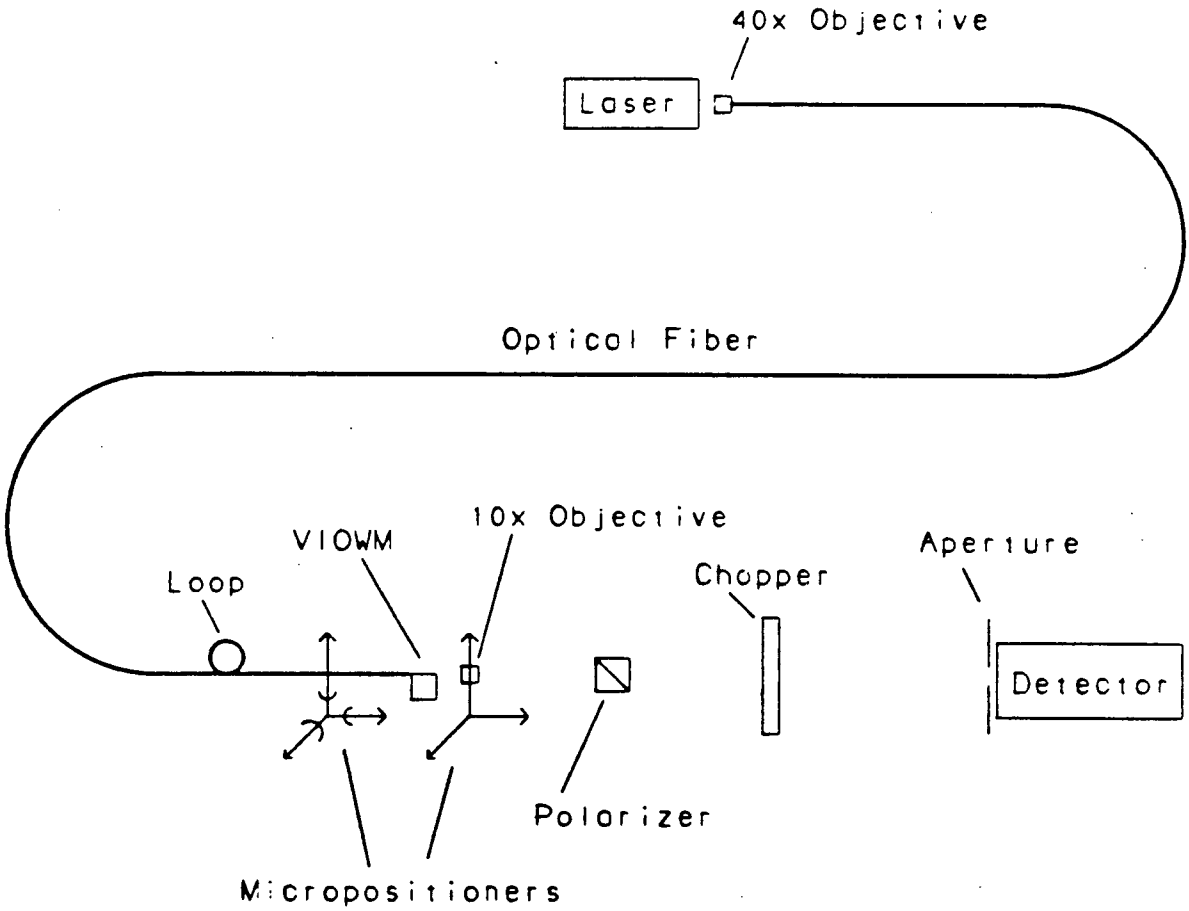

Figure 4.12: The basic laboratory apparatus used to make measurements on VIOWMs.

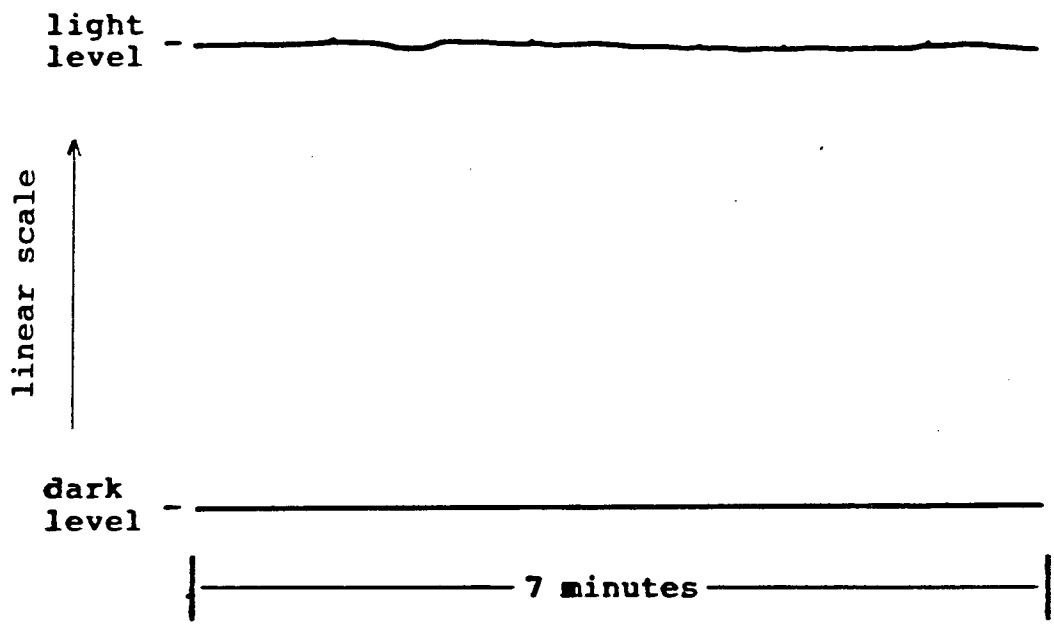

Figure 4.13: The polarized output of the optical fiber.

in nonzero coupling when zero volts are applied to the VIOWMs electrodes.

The detector was a was a LeCroy Fibercom Analog Receiver FAR-4HS. Its gain was adjusted so that 100 μW of input power corresponded to 1 V at the output. Before taking any measurements the fiber was positioned so that its output spot passed though the bulk of the crystal and was focused on the detector after passing through the polarizer and chopper. The peak value of the power was then recorded. This "straight through" power could then be used to calculate the coupling efficiency to the waveguide.

All of the tests were performed on VIOWMs with a 4μm interelectrode gap.

In figures 4.14, 4.15, and 4.16 a 500Hz triangle wave, with zero offset voltage, was applied to the electrodes of a VIOWM, nominally 1 mm long. the peak-to-peak voltages applied to the electrodes are 70, 100, and 130 volts respectively.

Figure 4.14 demonstrates the shape of the transfer curves at low voltages as well as the advantages of applying a negative voltage to the VIOWM in the off state. In this case -35V needed to be applied to reduce the optical throughput to a minimum. The negative portion of the input signal is useful for two reasons; first it acts to create an "anti-waveguide" and second it helps the VIOWM recover from changes in the refractive index distribution believed to be

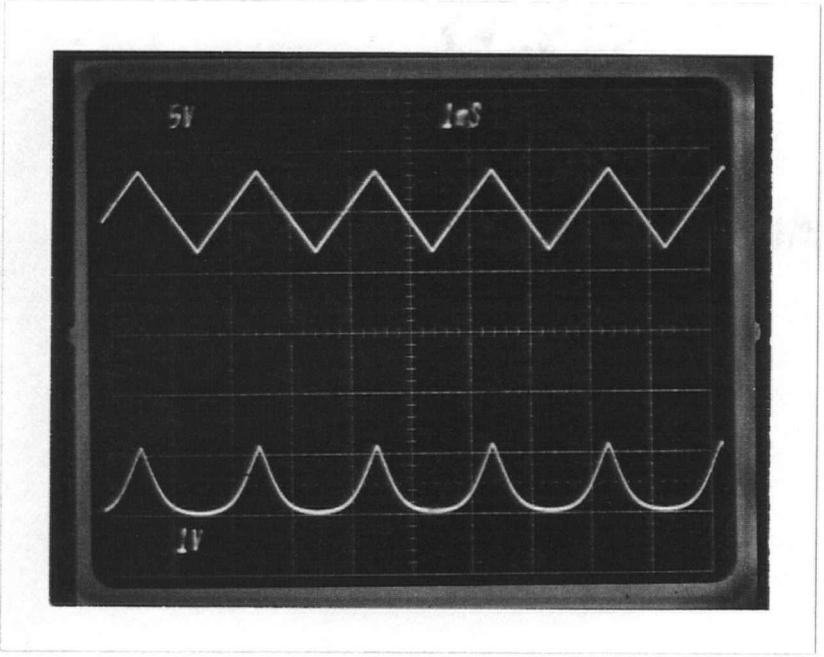

Figure 4.14: The output of a VIOWM with a 4 μm interelectrode gap for a 70 V peak-to-peak triangle wave applied to the electrodes.

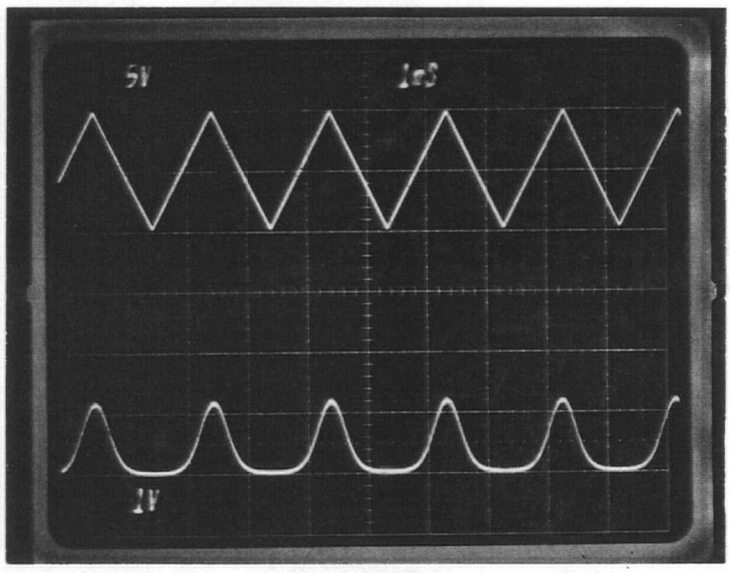

Figure 4.15: The output of a VIOWM with a 4 μm interelectrode gap for a 100 V peak-to-peak triangle wave applied to the electrodes.

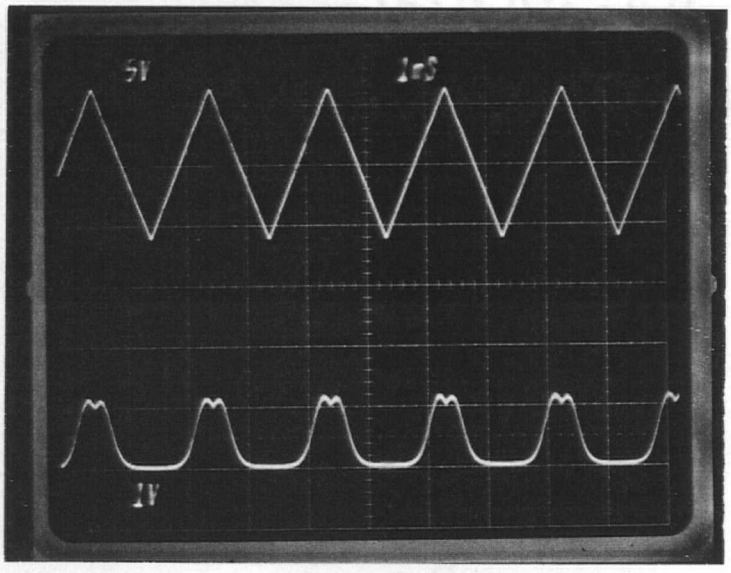

Figure 4.16: The output of a VIOWM with a 4 μm interelectrode gap for a 130 V peak-to-peak triangle wave applied to the electrodes.

due to the photorefractive effect [67]. By the term anti-waveguide is meant a low refractive index region out of which light propagating in the bulk modes is steered creating a dark spot in the interelectrode region. Upon the application of the negative voltage the dark spot was located exactly where the output spot was located upon the application of the positive voltage. Thus the extinction ratio was enhanced. The mechanism for the change in the refractive index distribution is discussed in more detail below.

Figure 4.15 demonstrates that increasing the applied voltage does, in fact, cause the power transfer to saturate, as predicted in the theory, furthermore figure 4.16 demonstrates that increasing the voltage further will cause a reduction in the coupling efficiency. The maximum coupling efficiency here was determined to be about -4dB. This calculation is obtained as 10 times the logarithm of the output optical power from its peak value to its value with 0 V applied divided by the straight through power. In this way attenuations and reflections for both the output and straight through powers would be the same with the exception that the output power would be scattered by interactions with the $LiNbO_3/SiO_2$ interface. However these interactions would be small based on the measurements of about -1 dB/cm loss for diffused waveguides which also have scattering at this interface [68].

In figure 4.17 the theoretical coupling coefficient T^2 and the measured data are compared. The theoretical curve is for a planar device having a 4 μm interelectrode gap with the coupling optimized for 50.0 V. The measured data is from figure 4.16 and has been scaled by a factor of about 2.0 to fit the theoretical predictions at 0.0 and 50.0 V. A factor of this order is to be expected due to a slight fiber to device misalignment. The shapes of the theoretical and measured curves are in good agreement except that there is a slight discrepancy at low voltage which is believed to be due to bulk mode coupling.

Other experiments were performed using the apparatus shown in figure 4.18. In this case polarized light was end-fire coupled into the VIOWM using a 40x microscope objective and the output was projected onto a detector (an Alphametrics model dc1010 using a model 1110s wide spectrum head), through an aperture, as before. The wavelength of the light was 633 nm and the VIOWM had a 4 μm interelectrode gap but this time it was about an inch long.

Figure 4.19 shows the output when a 0.5 Hz 70 V peak-to-peak triangle wave with zero offset voltage was applied to the electrodes. The total output power was low (21 μW peak) to reduce the photorefractive effect. The length of the VIOWM ensured that the bulk mode coupling would be small. The input coupling was such that the peak output occurred with about 30 V applied. This figure demonstrates,

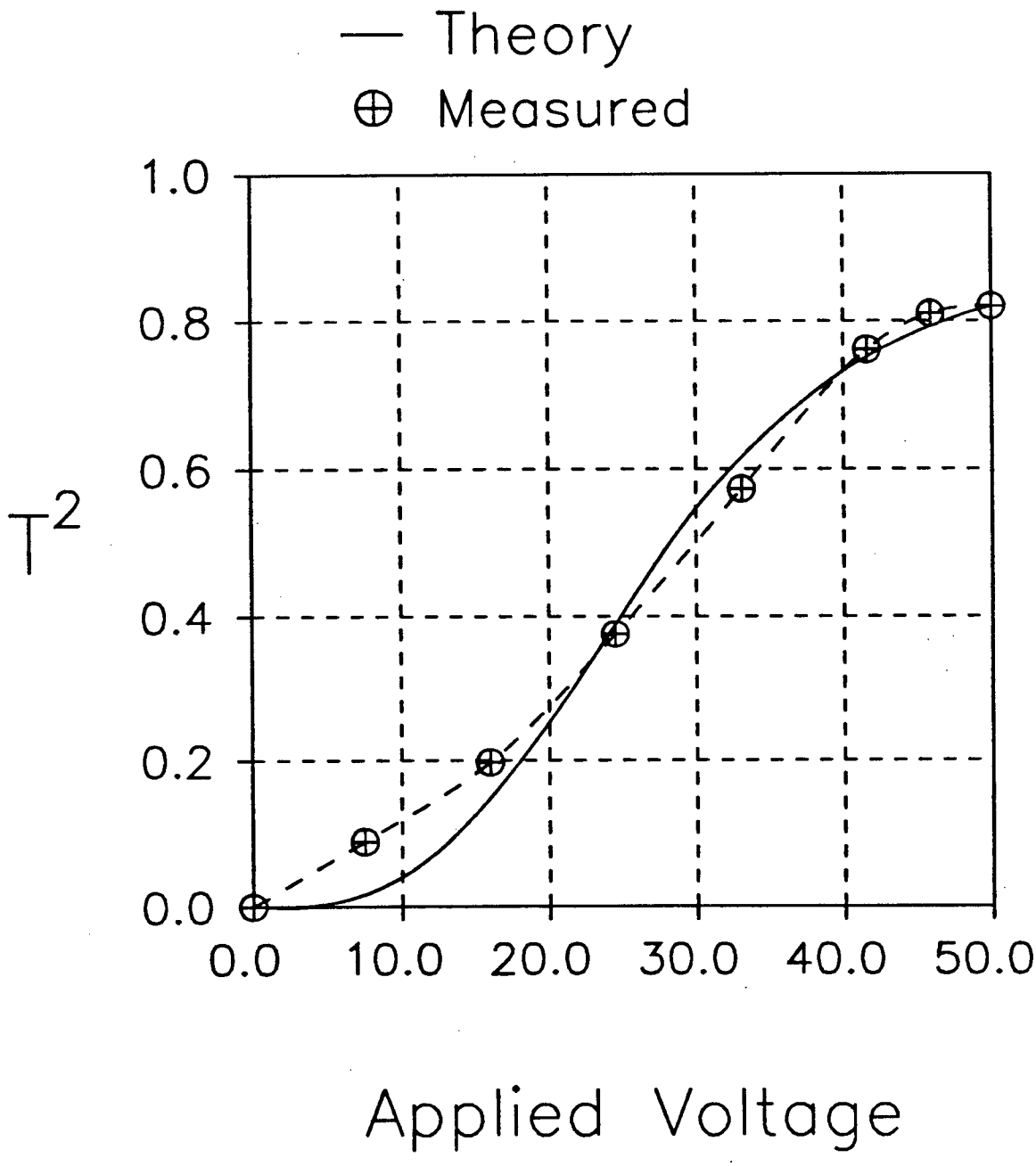

Figure 4.17: A comparison of the theoretical and measured results for a planar device.

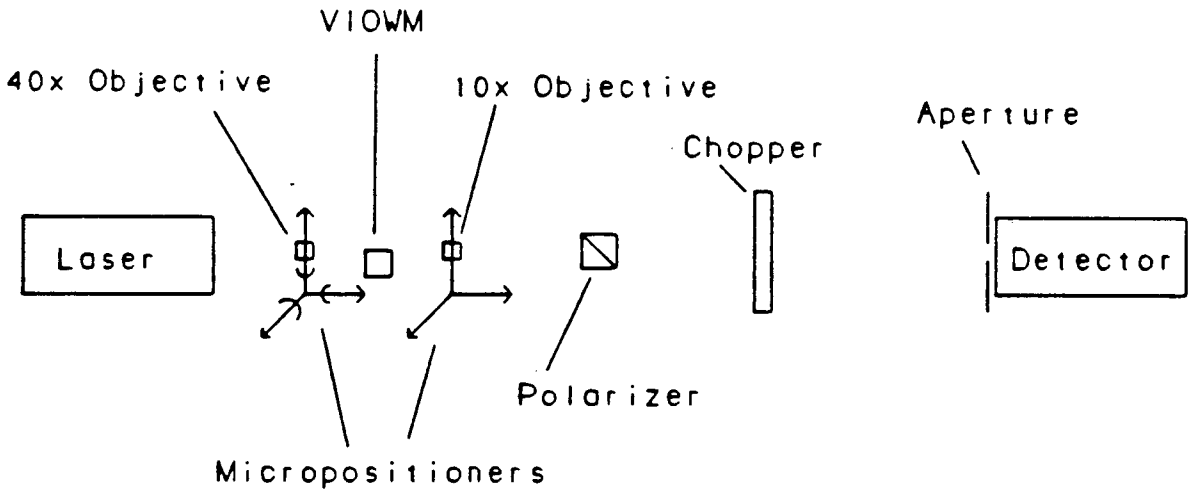

Figure 4.18: An alternate laboratory apparatus setup.

in the absence of the photorefractive effect and bulk mode coupling, the voltage controlled coupling behavior of the VIOWM. The extinction ratio was 23dB. At even lower optical power levels linear modulation of this device was demonstrated by applying a 15 V bias to the electrodes.

4.3 The Ridge VIOWM

The calculated results from the model for the planar VIOWM are presented in section 4.3.1 and the measured results are presented in section 4.3.2.

4.3.1 Calculated Results

The effect of ridge height on the operation of the VIOWM as regards the confinement of the guided mode as a function of ridge width and voltage is studied in this section. It is important to understand the effect of ridge height on the operation of VIOWMs. It will be shown that the coupling to an optical fiber, at a particular operating voltage, will depend on this parameter as will the "turn-on" voltage.

Here the turn-on voltage refers to the voltage below which the mode becomes detached from the ridge. At voltages below the turn-on voltage the width parameters of the mode

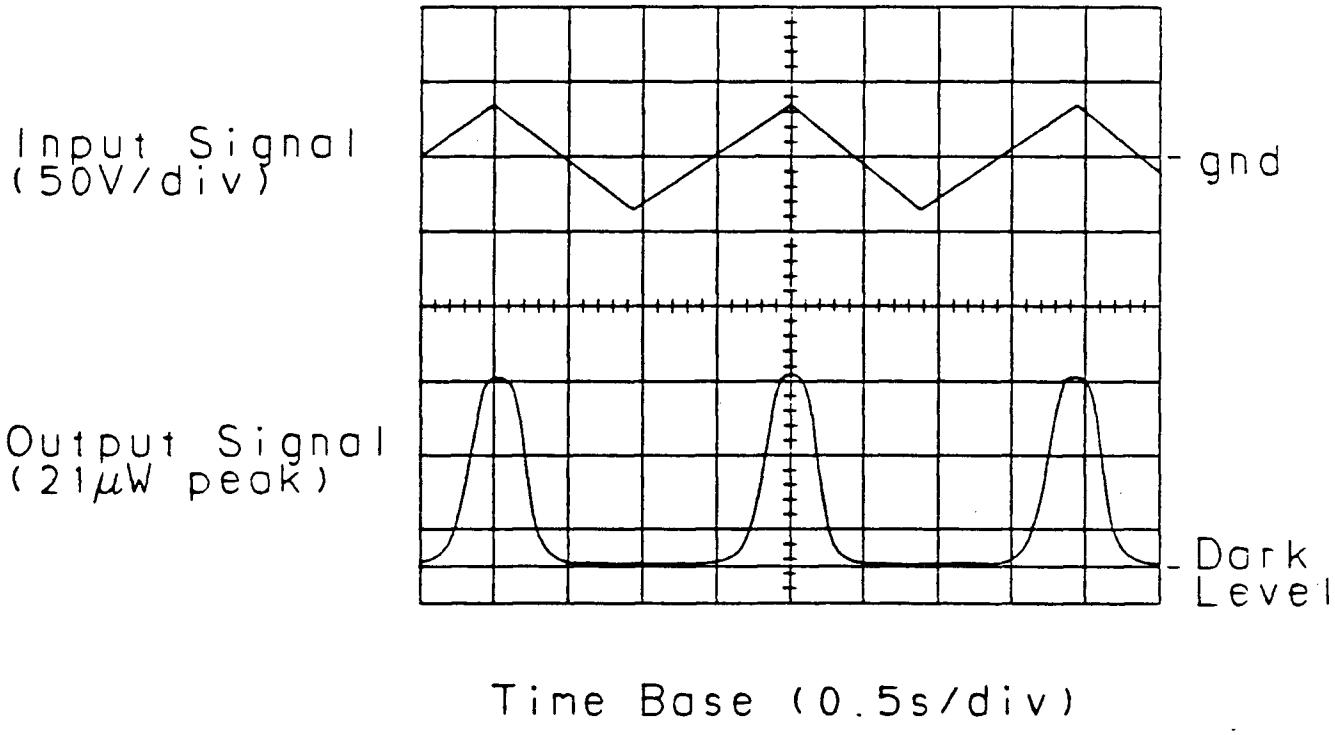

Figure 4.19: The output of a long VIOWM with a 70 V peak-to-peak triangle wave applied to the electrodes for λ_o = 663 nm.

increase rapidly however the ridge VIOWM will continue to act as a waveguide for any positive applied voltage. One can see this by considering what the refractive index distribution of the VIOWM looks like far away from the gap. Using the technique of conformal mapping for two coplanar electrodes separated by an infinitesimally small gap, with a voltage V_o applied between to the electordes, one finds that the electric field parallel to the Z-axis is given by

$$E_z(y,z) = - \frac{V_o \cos(\theta)}{\pi \rho}$$

where $\rho = [(\varepsilon_z/\varepsilon_y)y^2+z^2]^{1/2}$ and $\theta = \tan^{-1}[(\varepsilon_z/\varepsilon_y)^{1/2}y/z]$. From equation 2.2 one sees that the refractive index distribution will drop off as 1/r for any positive voltage (one can ignore the contribution of E_y as it will be small) as one moves away from the gap. Using either the WKB method [39] or the wave-vector method of Hocker and Burns [33] one finds that a ray travelling along a radial line will have a turning point for any positive voltage.*

Calculated results are presented for ridge VIOWMs with ridge heights 0.5, 1.0, and 1.5 times the gap width. These together with the results for the planar device complete our analysis of the effects of the variable parameters for

---

* Jaeger et al. [69] pp. 6-7.

VIOWMs for which trends can be predicted and the modus operandi explained.

Figures 4.20, 4.21 and 4.22 are topographical plots of the w_{yv} width parameters as functions of applied voltage and interelectrode gap width for ridge VIOWMs with heights of 0.5, 1.0, and 1.5 times the gap width respectively for λ_o = 442 nm. Figures 4.23, 4.24 and 4.25 are the corresponding plots for the w_{zv} width parameters. The shaded regions on the graphs indicate where the mode is detached from the ridge.

In figures 4.26 and 4.27 are plotted the coupling coefficients as functions of the applied voltage for a VIOWM with a 7 μm interelectrode gap and a half-height (0.5 times gap width) ridge. For these figures it has been assumed that the optical fibers are located so as to maximize the power transfer for applied voltages of 30 V and 50 V respectively. Again, as for the planar device, one sees that a greater degree of coupling will occur at voltages greater than either 30 V, in figure 4.26, or 50 V, in figure 4.27, however the degree of coupling at these voltages is the greatest that may be achieved.

In figures 4.28, 4.29 and 4.30 are plotted the optimum fraction of power transfer, T^2, that can be obtained for ridge VIOWMs with heights of 0.5, 1.0, and 1.5 times the gap width respectively, for λ_o = 442 nm, as functions of both voltage and interelectrode gap width. From figure 4.28 one

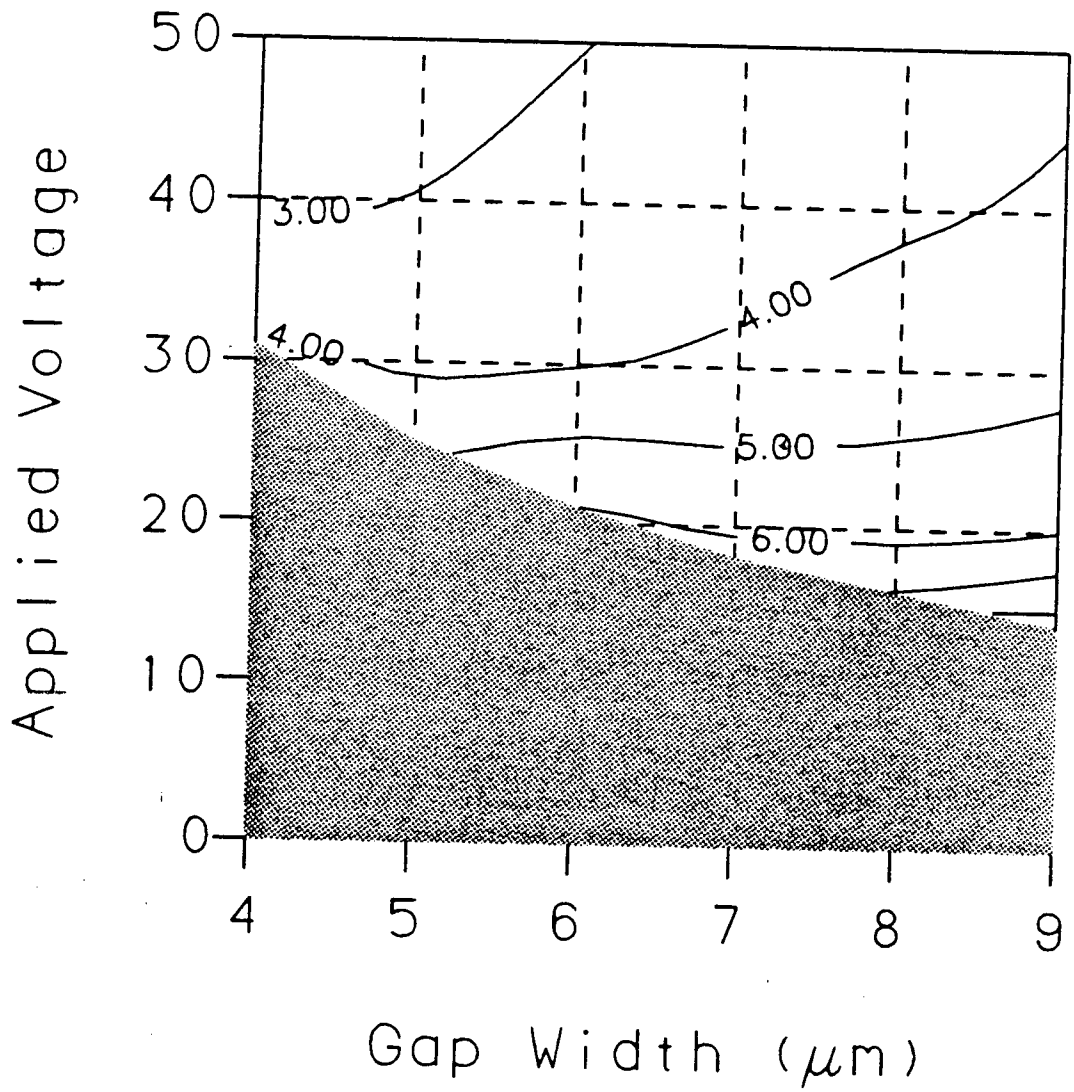

Figure 4.20: A topographical plot of w_{yv} for a ridge height 0.5 times the interelectrode gap width where λ_o = 442 nm.

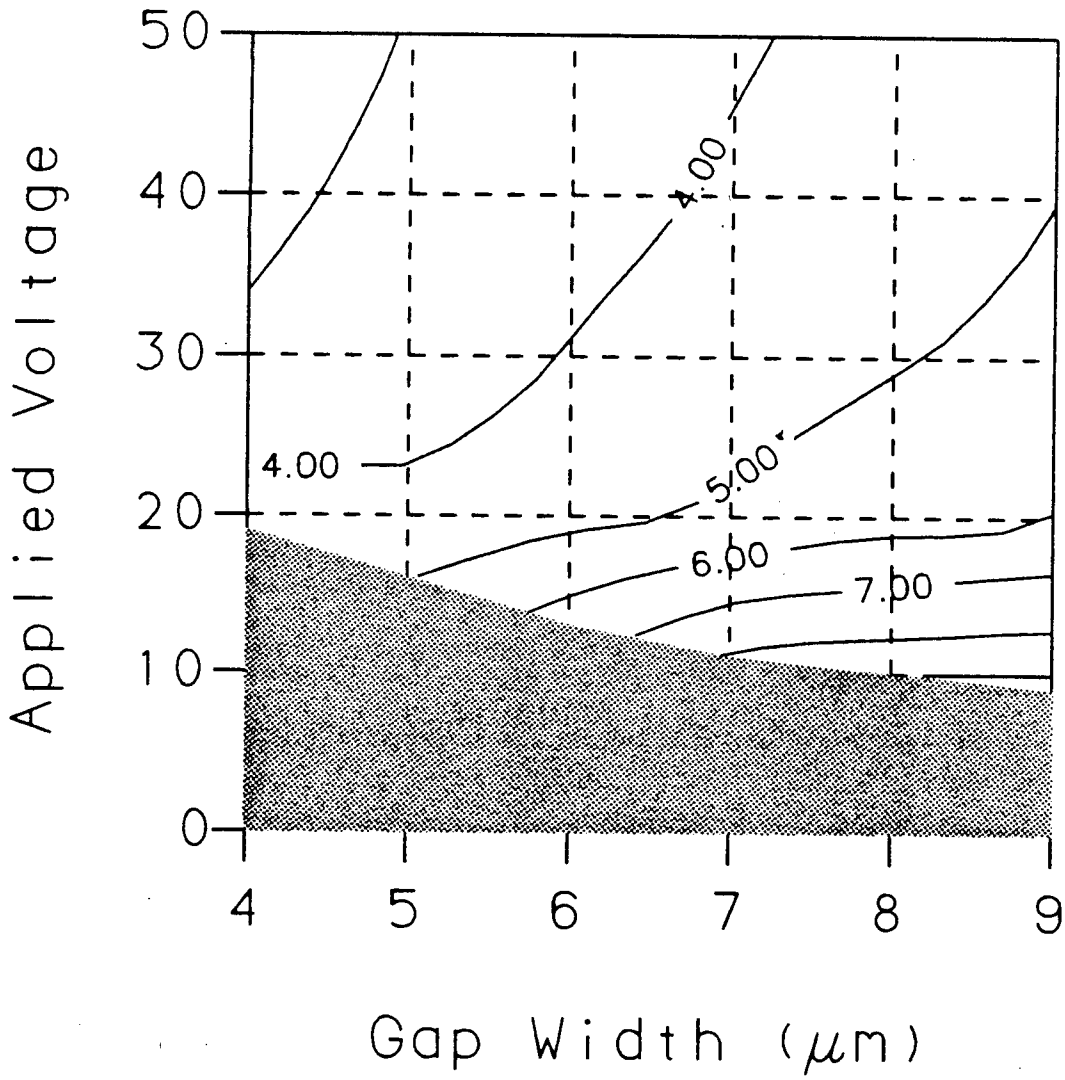

Figure 4.21: A topographical plot of w_{yy} for a ridge height 1.0 times the interelectrode gap width where λ_o = 442 nm.

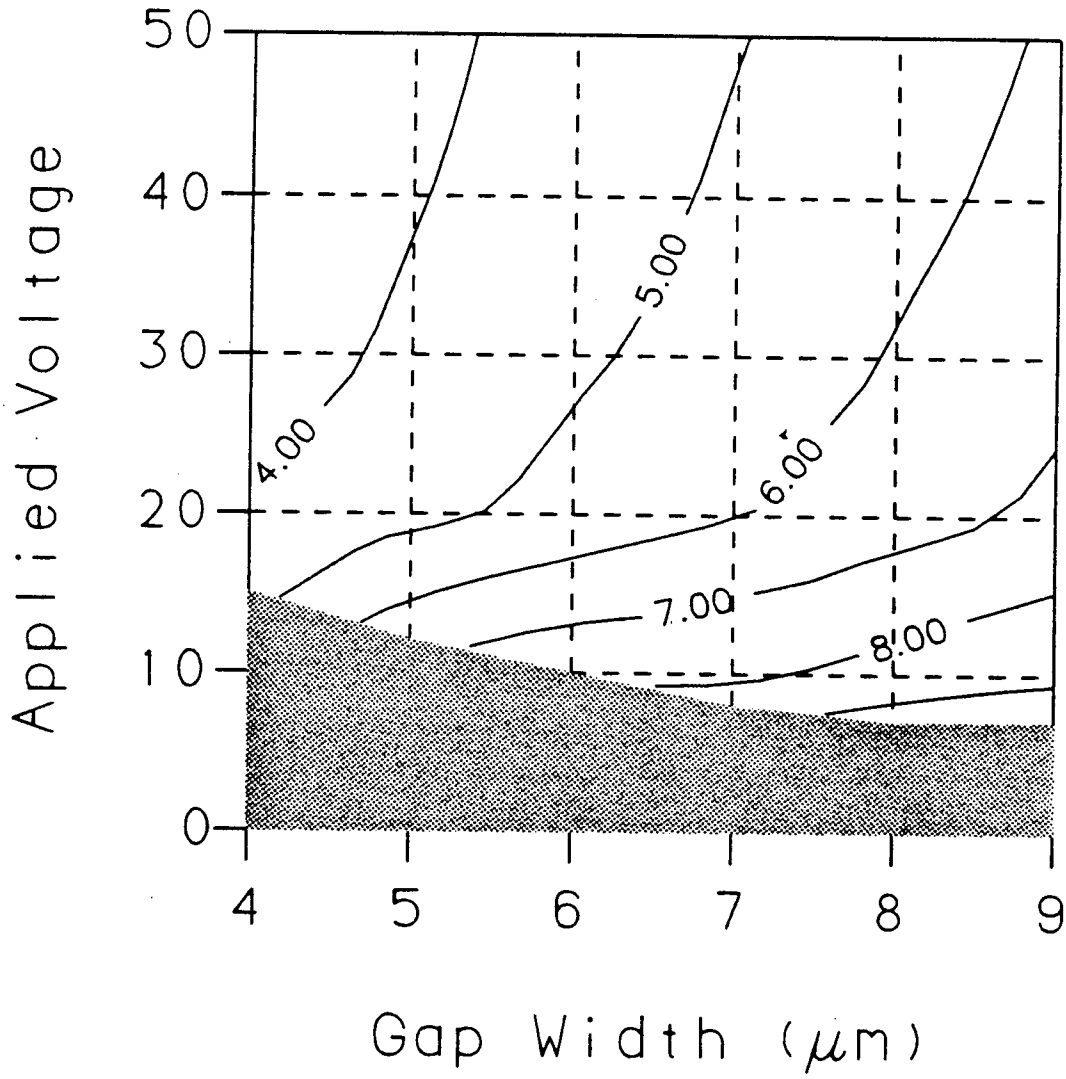

Figure 4.22: A topographical plot of w_{yy} for a ridge height 1.5 times the interelectrode gap width where λ_o = 442 nm.

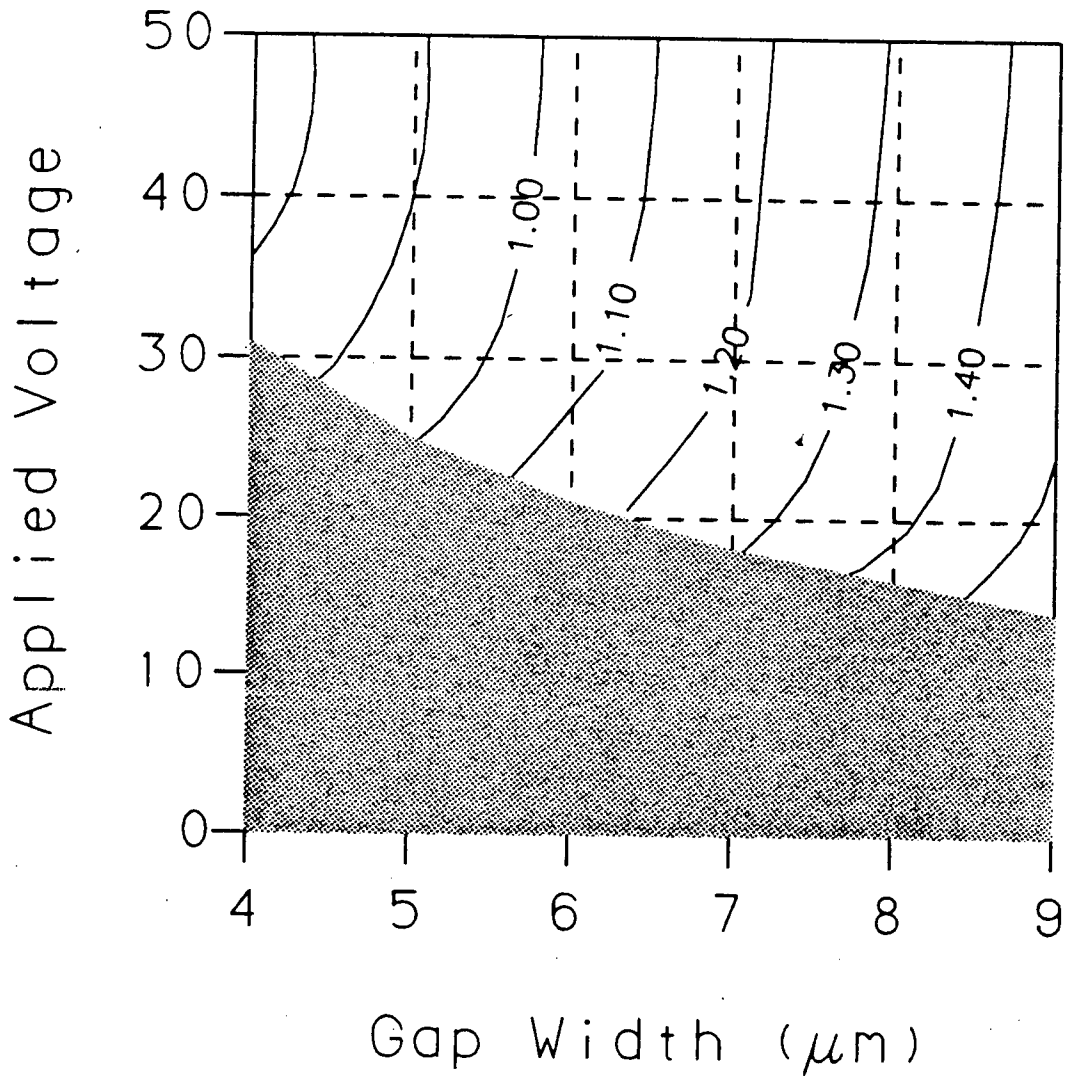

Figure 4.23: A topographical plot of w_{zv} for a ridge height 0.5 times the interelectrode gap width where λ_o = 442 nm.

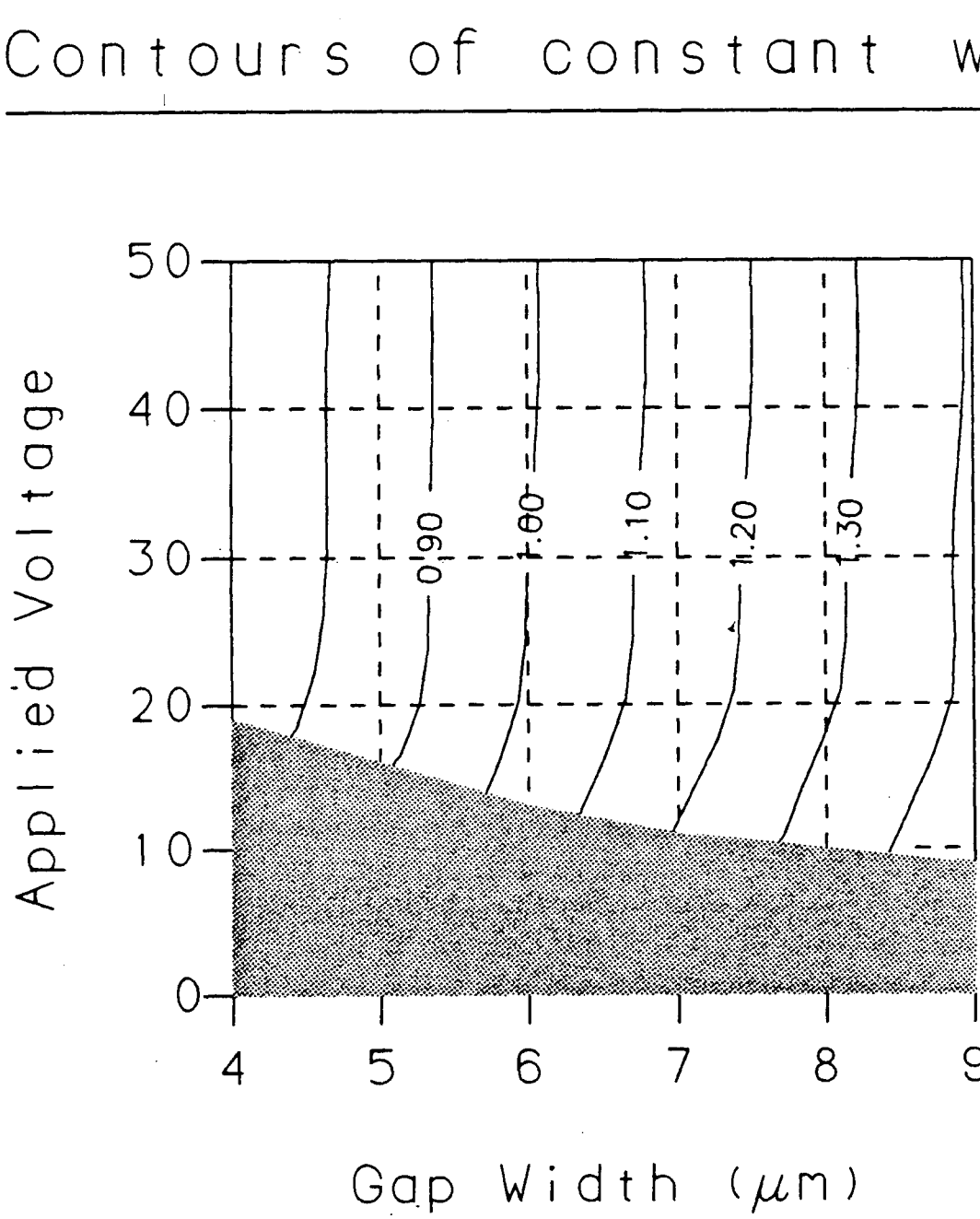

Figure 4.24: A topographical plot of w_{zv} for a ridge height 1.0 times the interelectrode gap width where λ_o = 442 nm.

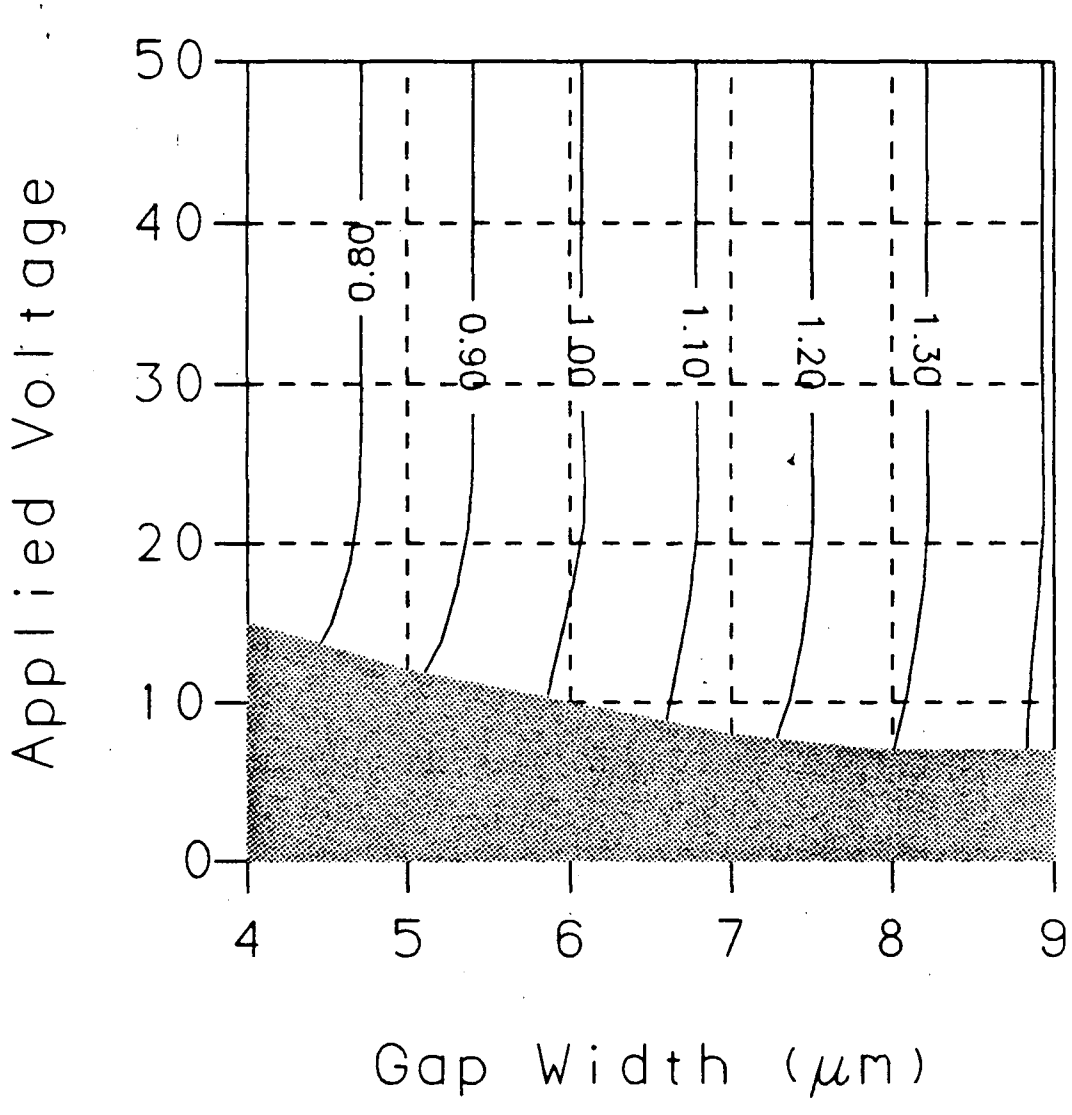

Figure 4.25: A topographical plot of w_{zv} for a ridge height 1.5 times the interelectrode gap width where λ_o = 442 nm.

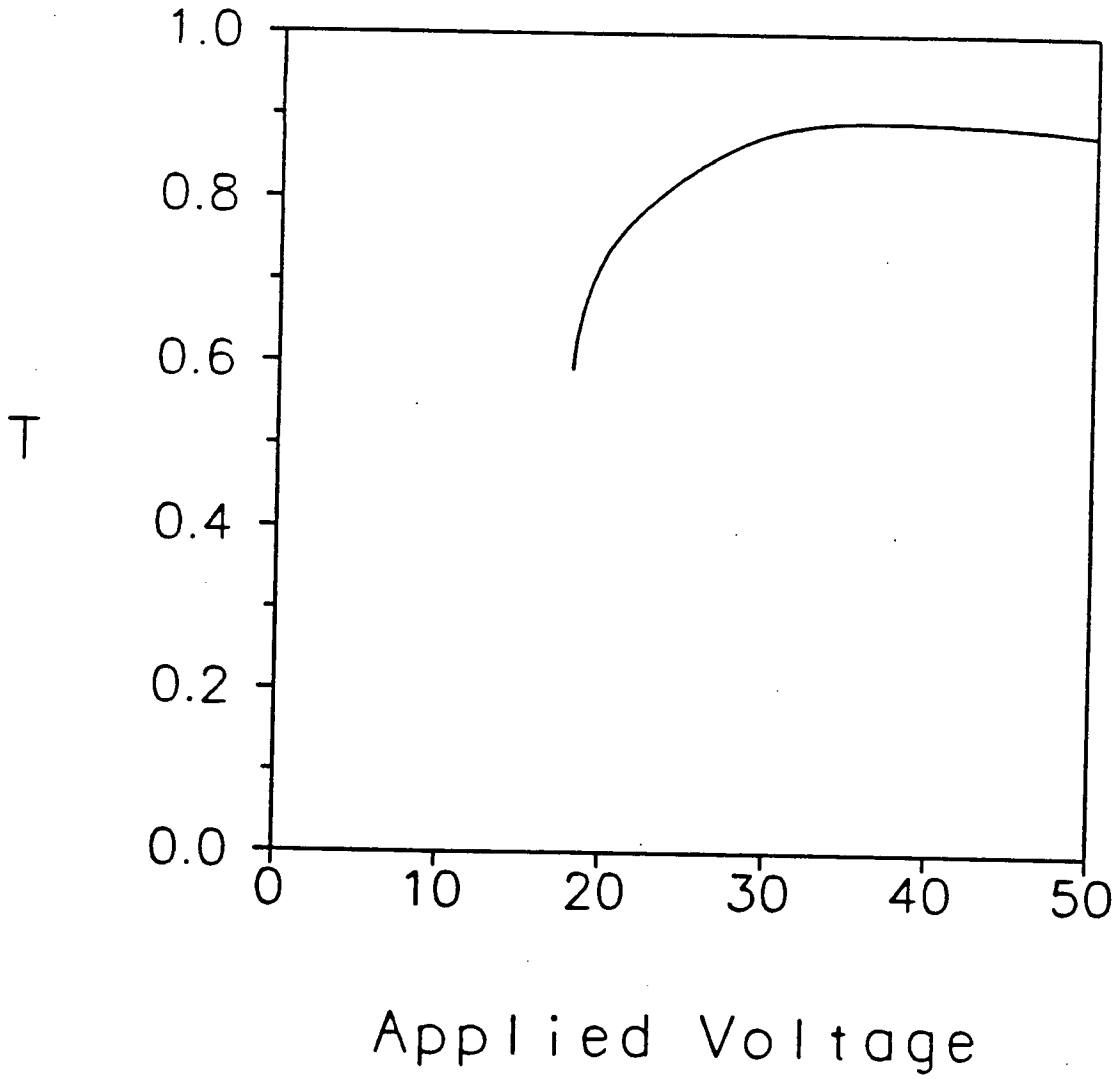

Figure 4.26: The coupling coefficient T vs. voltage for g = 7 μm for a half-height ridge where the coupling at 30 V is maximized.

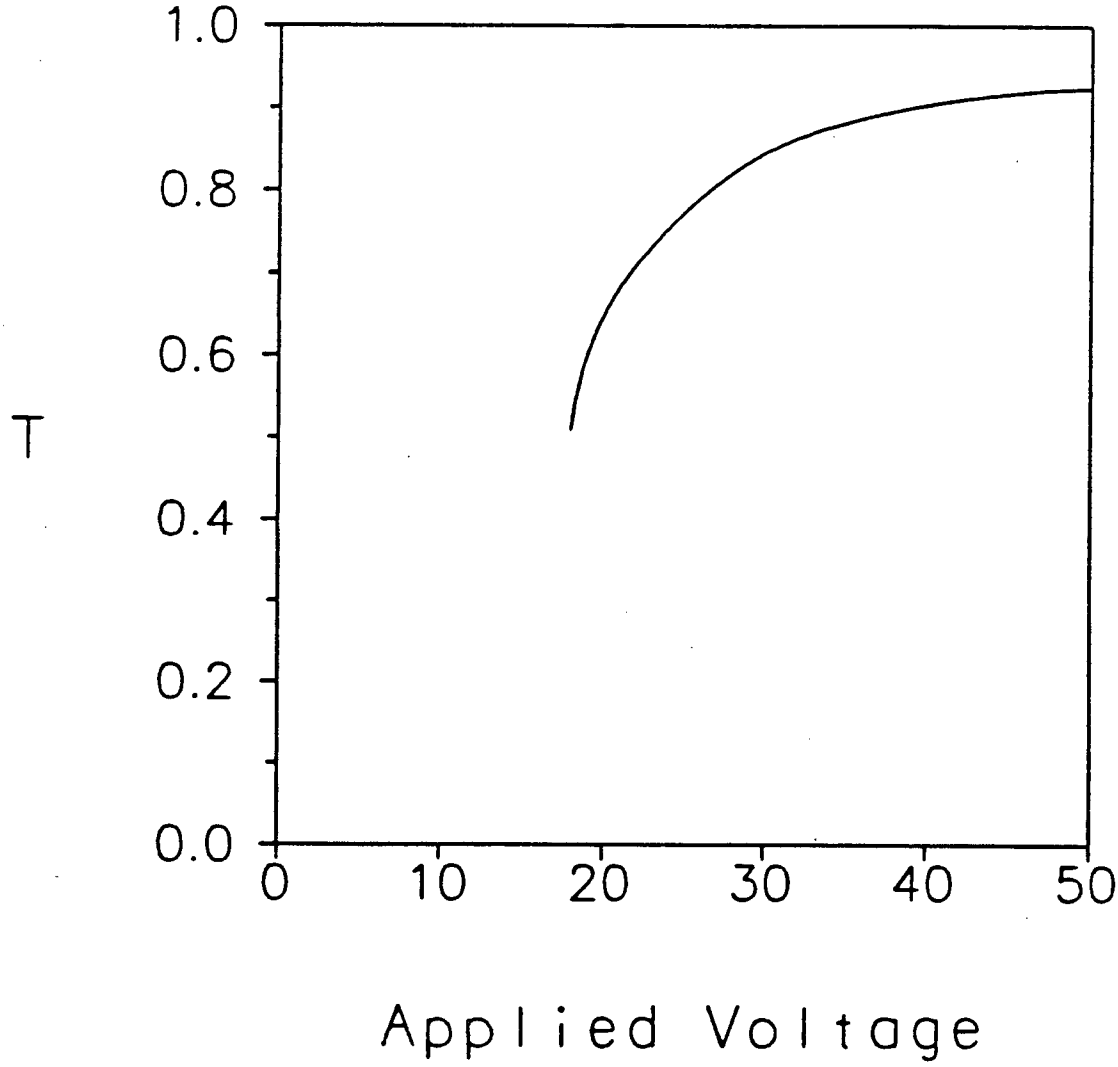

Figure 4.27: The coupling coefficient T vs. voltage for g = 7 μm for a half-height ridge where the coupling at 50 V is maximized.

can see that it is possible to obtain -3dB power transfer between an optical fiber that supports a mode with width parameters $w_{yf} = w_{zy} = 1.50$ μm and a half-height VIOWM with an applied voltage of only ~ 15 V. Also from figure 4.29 one can see that the same coupling can be obtained for ~ 12 V and from figure 4.30 for ~ 11.5 V.

Again we have considered that the ridge VIOWM could be used as a small signal linear modulator located between two optical fibers. In figures 4.31 and 4.32 are plotted T^4 for the cases in which both optical fibers are located so as to achieve the optimum coupling for a half-height ridge VIOWM with a 7 μm interelectrode gap for a wavelength of 442 nm when 30 V and 50 V applied to the electrodes respectively. Again both figures show small linear regions but neither figure indicates the same potential as a linear modulator as does figure 4.11 for a planar device with a 2μm interelectrode gap.

4.3.2 Measured Results

Figure 4.33 shows a 500 Hz, 100 V peak-to-peak triangle wave, with zero offset voltage, applied to a half-height ridge VIOWM with a fiber at the input as described in section 4.2.2. The base of the ridge is about 7.5 μm wide and the device was nominally 1 mm long. The knee in the

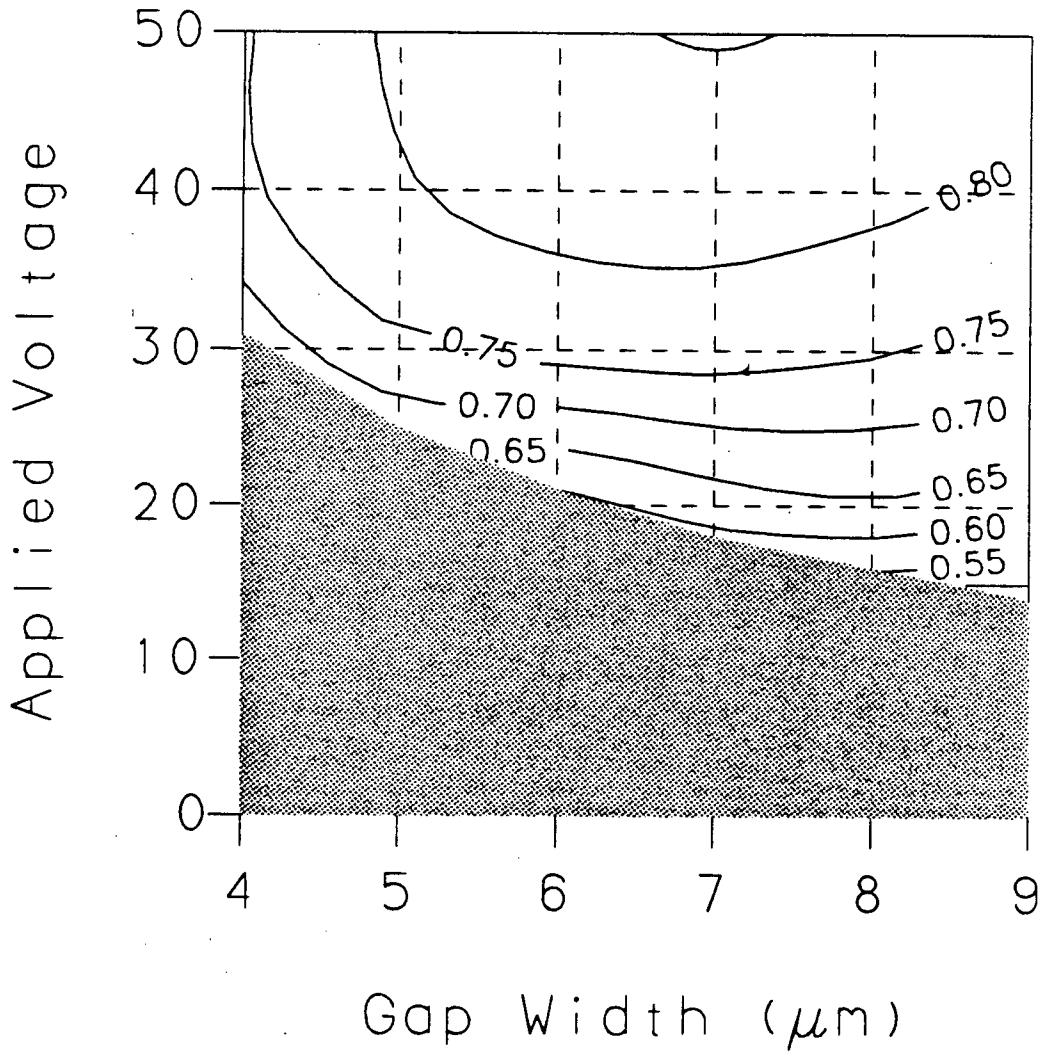

Figure 4.28: The optimum power transfer T^2 as a function of applied voltage and interelectrode gap width for a ridge 0.5 times the gap width.

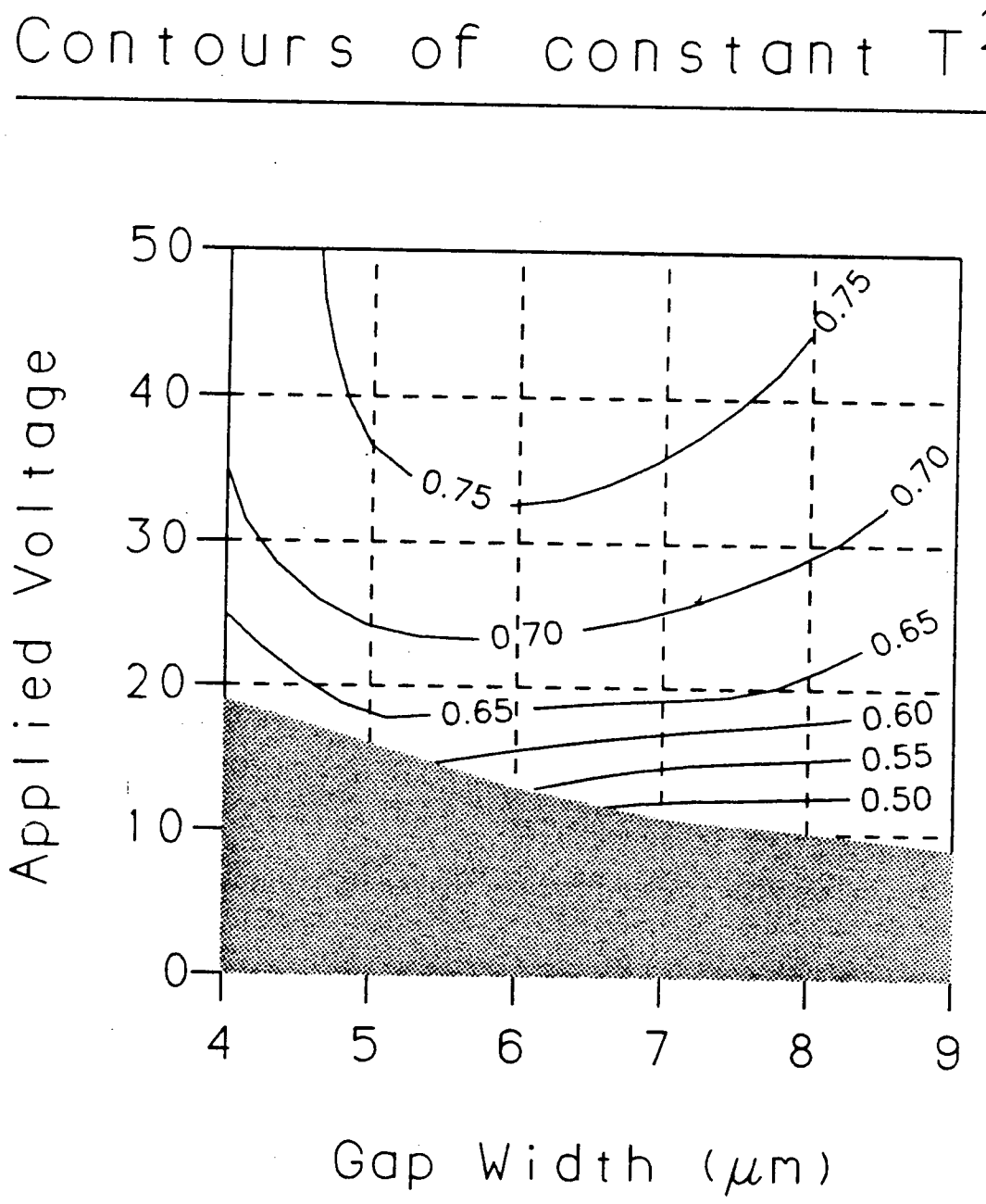

Figure 4.29: The optimum power transfer T^2 as a function of applied voltage and interelectrode gap width for a ridge 1.0 times the gap width.

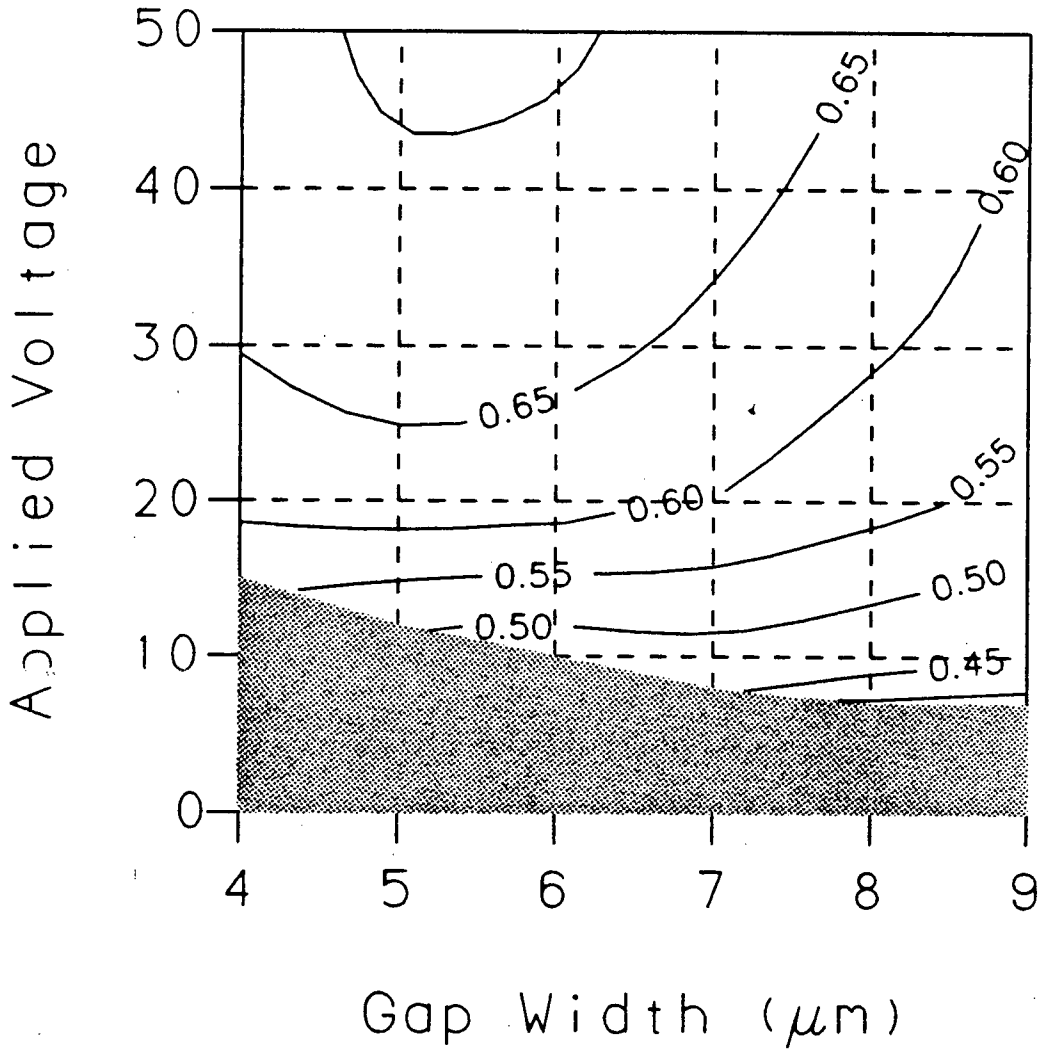

Figure 4.30: The optimum power transfer T^2 as a function of applied voltage and interelectrode gap width for a ridge 1.5 times the gap width.

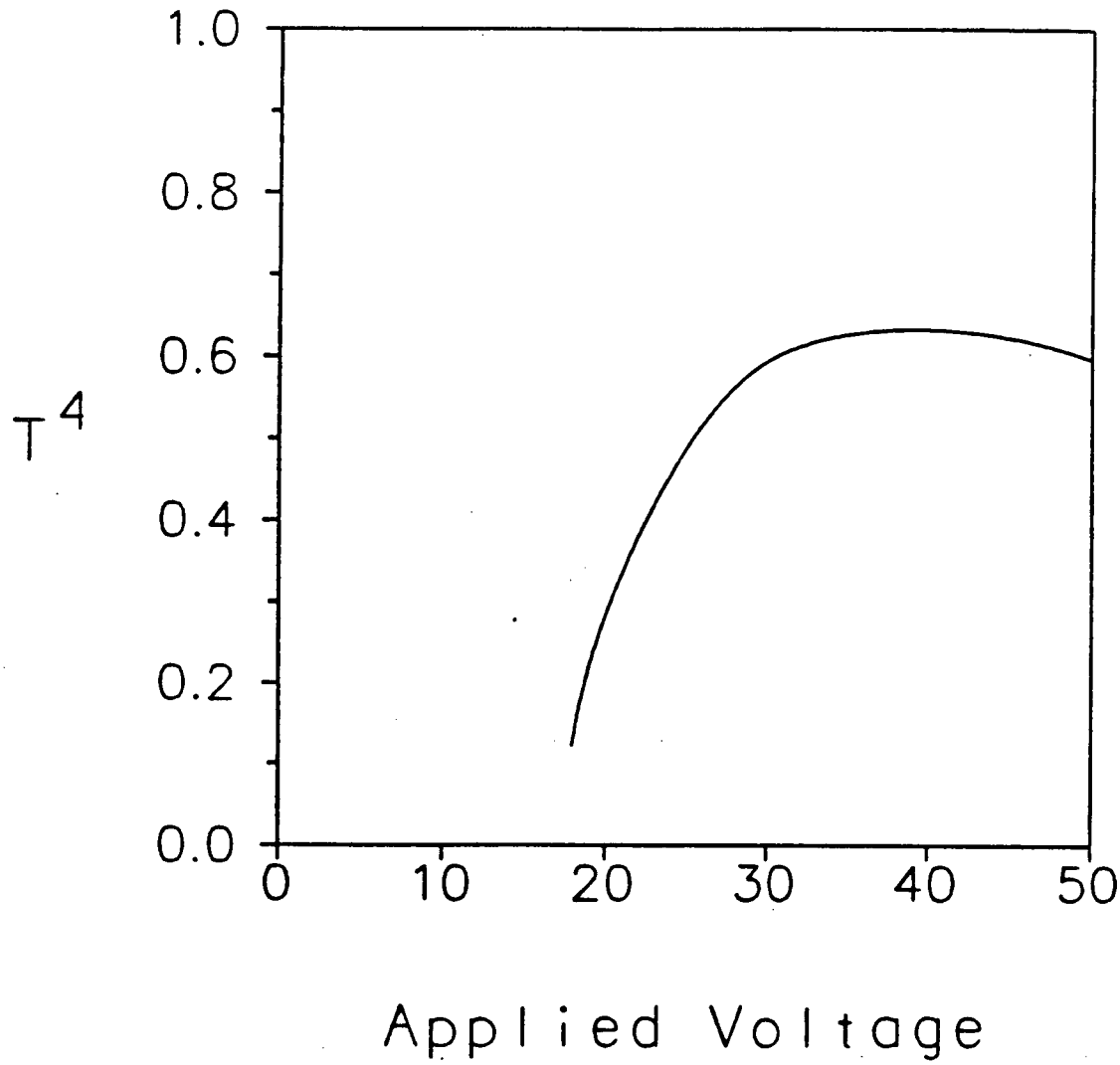

Figure 4.31: The power transfer T^4 between two optical fibers where the coupling at 30 V is maximized for the ridge device.

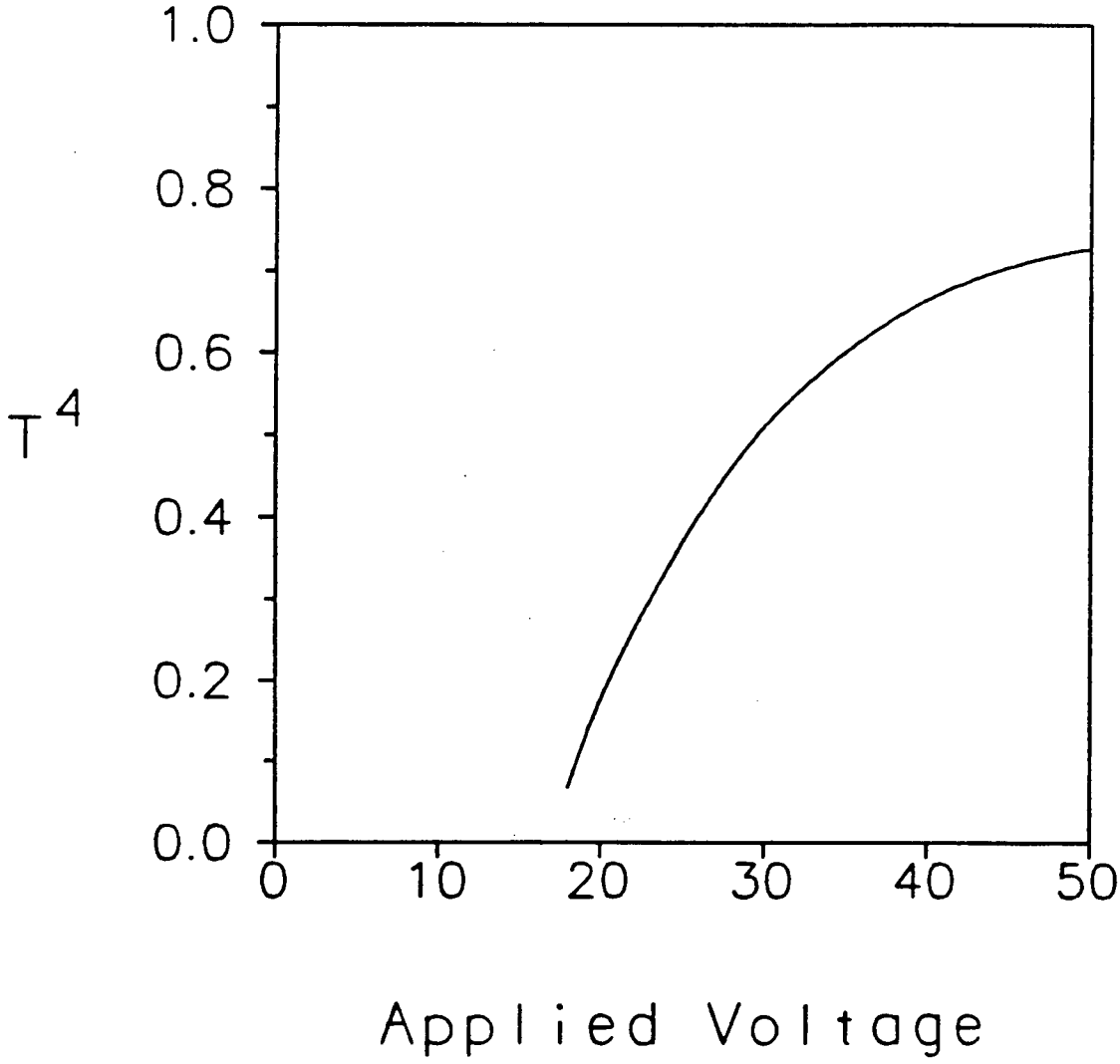

Figure 4.32: The power transfer T^4 between two optical fibers where the coupling at 50 V is maximized for the ridge device.

output can clearly be seen for an applied voltage of about 20 V. This effect is believed to be due to a rapid change in the width parameters of the fundamental mode of the VIOWM as it becomes more highly confined to the region of the ridge.

In figure 4.34 the theoretical coupling coefficient T^2 and the measured data are compared. The theoretical curve is for a rectangular half-height ridge having a 7 μm interelectrode gap with the coupling optimized for 40.0 V. The measured data is from figure 4.33 and has been scaled by a factor of about 2.2 to fit the theoretical predictions at 0.0 and 50.0 V. A factor of this order is to be expected due to a slight fiber to device misalignment and scattering at the ridge walls which were not ideally smooth. The measurements show a knee at about 18.0 V in good agreement with the theoretical turn-on voltage. The shape of the curves above 18.0 V do not agree well. This is believed to be due to the difference in the shapes of the rectangular ridges studied in the theory and the ridge with slanted walls that was fabricated.

Figure 4.35 shows a 500 Hz, 120 V peak-to-peak triangle wave, with zero offset voltage, applied to a half-height ridge VIOWM again with a fiber at the input. Again the base of the ridge is about 7.5 μm and the device is nominally 1 mm long. From this figure one can again see that the coupling reaches a maximum and then decreases. The maximum

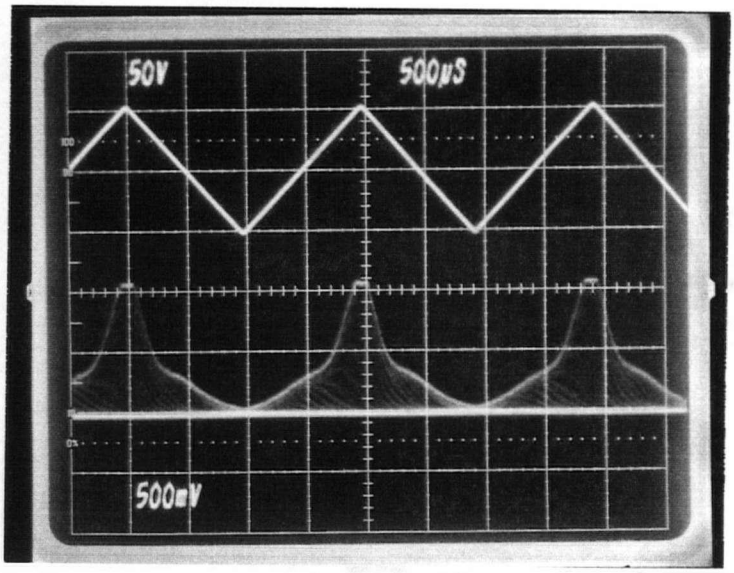

Figure 4.33: The output of a half-height VIOWM with a 7.5 μm interelectrode gap for a 100 V peak-to-peak triangle wave applied to the electrodes where λ_o = 442 nm.

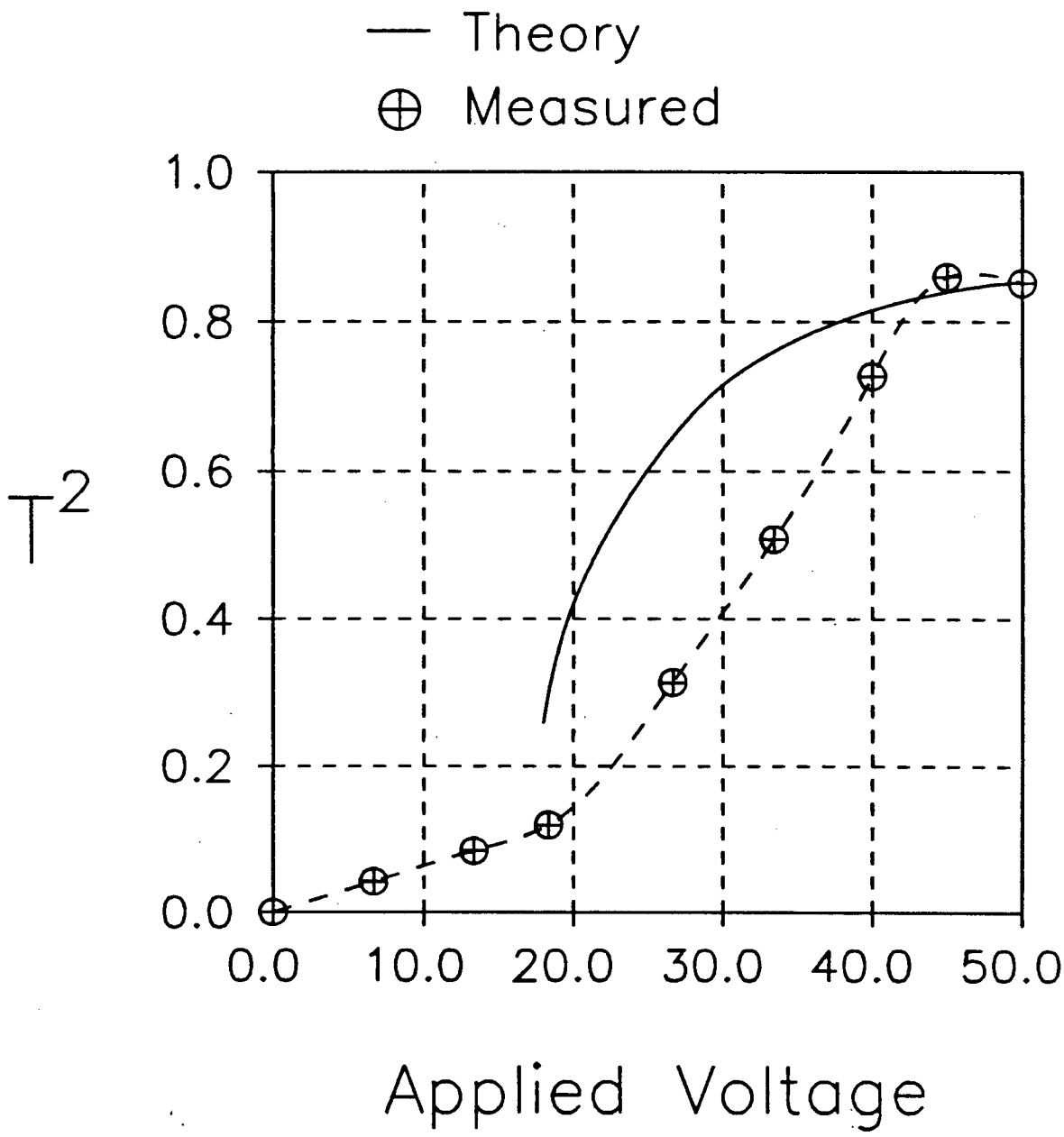

Figure 4.34: A comparison of the theoretical and measured results for a half-height ridge.

coupling efficiency here was determined to be about -4.5dB. Again, as in section 4.2.2, this calculation is obtained as 10 times the logarithm of the output optical power from its peak value to its value with 0 V applied divided by the straight through power. This was not compensated for the effects of scattering at the $LiNbO_3/SiO_2$ interface although, as can be seen in figure 3.2, the walls of the waveguide are far rougher than the surface and will probably result in much more scattering than for a planar device. It is believed, therefore, that the coupling effieciency at the input is better than this result indicates.

Figure 4.36 shows a 500Hz, ±20V square wave applied to the electrodes of a half-height VIOWM. The peak output power is seen to be about 50 μW and the minimum output is seen to be about 10 μW corresponding to an extinction ratio of about 7dB.

4.4 The Front-End Switch

In this section are presented the results of measurements on a VIOWM that was permanently aligned with an optical fiber in a flip-chip arrangement on an Si wafer with etched V-grooves. The voltage signal was applied via probes to the electrodes on the Si wafer. Here λ_o = 442 nm.

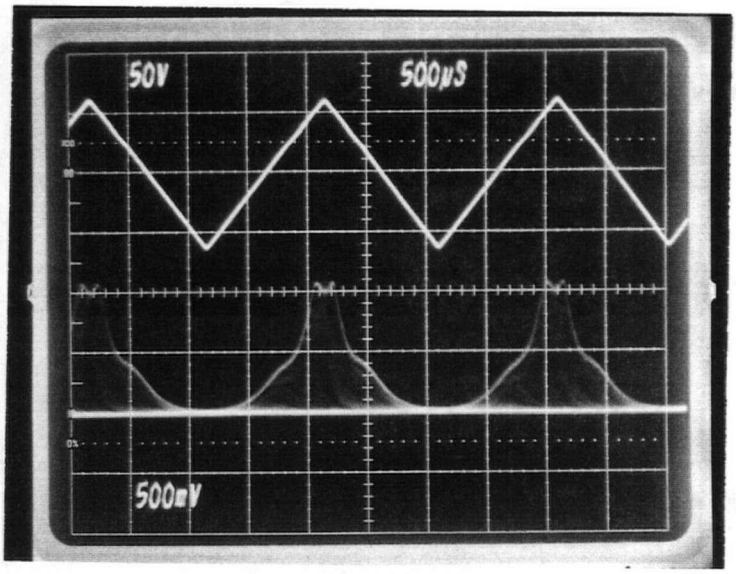

Figure 4.35: The output of a half-height VIOWM with a 7.5 μm interelectrode gap for a 120 V peak-to-peak triangle wave applied to the electrodes where λ_o = 442 nm.

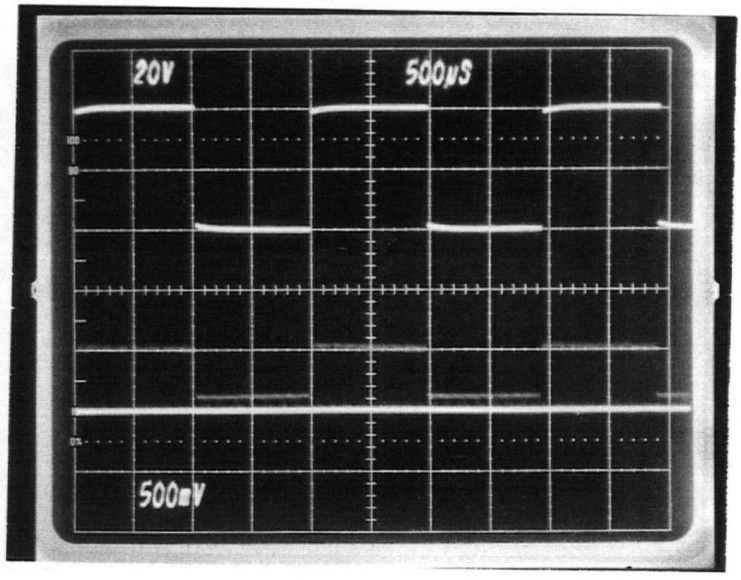

Figure 4.36: The output of a half-height VIOWM for a ±20 V square wave applied to the electrodes.

The application of a VIOWM as a digital switch is demonstrated by figure 4.37. In this figure a 500Hz, ±50V square wave is applied to the electrodes. The VIOWM is acting as a front-end switch controlling the amount of optical power coupled into the fiber. The other end of the fiber was inserted into the LeCroy Fibercom Analog Receiver. The output signal indicated that the peak-to-peak change in optical power was ~ 240 μW.

It was found that with a constant voltage applied to the electrodes over a period of time the waveguide would decay and, in effect, turn off. It took several seconds for the waveguide to turn off although the effect set in immediately. This was probably due to the photorefractive effect [22] rather than domain reversal [70,71]. Figure 4.38 shows a 0.1 Hz, ±50 V square wave applied to the electrodes. As can be seen when 50 V is applied to the electrodes, there is a rapid initial response by the VIOWM followed by a slow decay of the throughput. Similarly, when the polarity of the applied voltage is reversed the throughput is initially a minimum and increases with time. The "melting" away of the waveguide and the dark spot can be seen quite clearly when the output is projected on a screen.

We believe that this effect is due to the photorefractive effect rather than domain reversal. If it were due to domain reversal then after a long application of voltage, long enough for the waveguide to turn completely

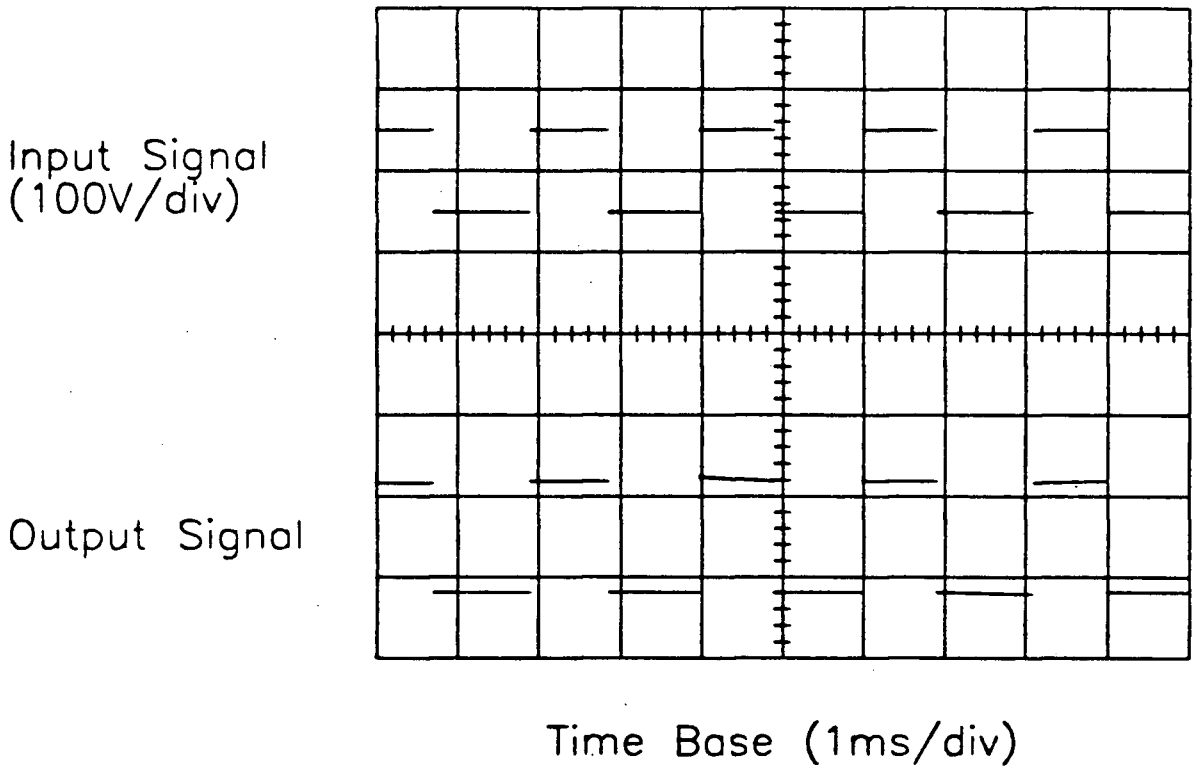

Figure 4.37: The output of an optical fiber with a VIOWM acting as a front-end switch for a ±50 V square wave. Here the switched optical power is ~ 240 μW.

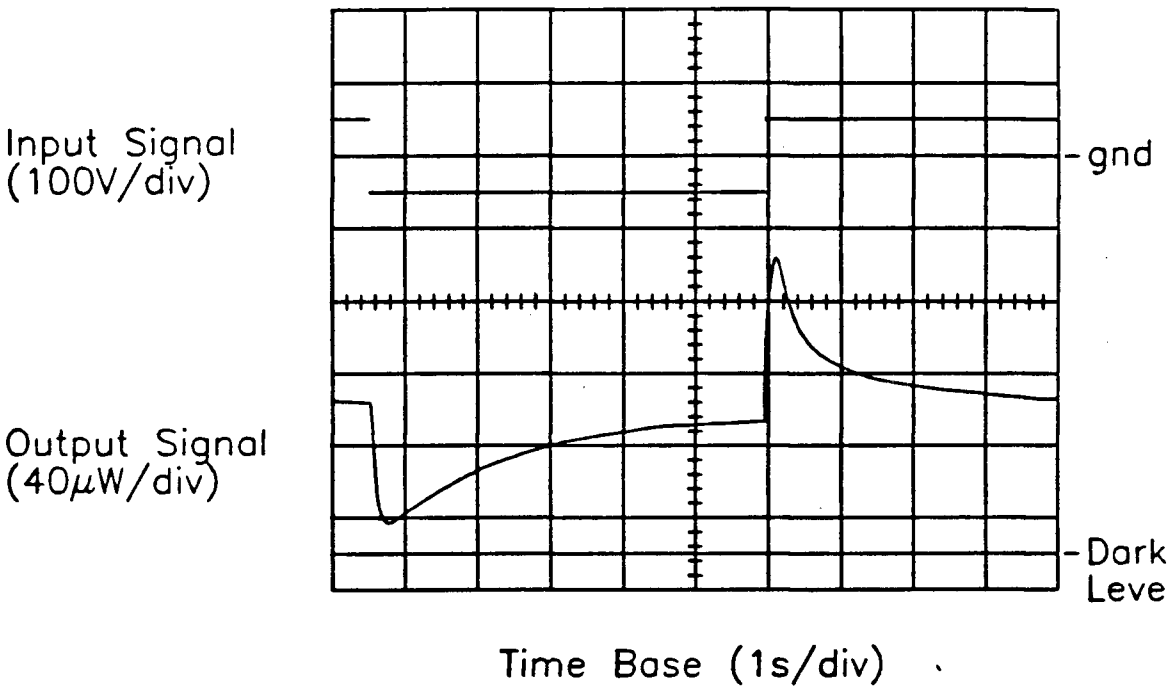

Figure 4.38: The decay of the output of a VIOWM as a function of time.

off, we would have achieved the reversal of a sufficient number of domains so that there would be virtually no electrooptic effect. If this were the case then upon the reversal of the field there should still be very little electrooptic effect and the output power should remain relatively constant. Figure 4.38 indicates that this was not the case. In fact we see that initially the throughput is a minimum and gradually increases, i.e. the dark spot at first is very much there and then gradually disappears. Again if this were due to domain reversal then upon a second reversal of the applied field there should be little change in the throughput but we see a rapid increase instead. In fact figure 4.38 indicates that during the application of a negative voltage the waveguide recovers. The negative voltage is therefore useful as a fly-back cycle. Furthermore domain reversal usually occurs in $LiNbO_3$ in which an impurity gradient exists [72], usually due to an in-diffusion, although Pendergrass [71] has seen domain reversal in substrates into which no impurities were diffused.

The photorefractive effect is the name given to a variety of effects that cause changes in the refractive indices of materials when they are exposed to light. In $LiNbO_3$ mobile electrons are produced when light is absorbed by impurities such as Fe [22]. Without any external electric field applied the photoexcited carriers move in the crystal

and so as to generate a voltage such that the +c-end of the crystal is negative [73]. This is the bulk photovoltaic effect. If the carriers are captured by traps at the edges of the illuminated region a space charge region may be established that alters the refractive index via the linear electrooptic effect.* Kraetzig and Kurz [73] found that an external field can be applied that will stop the photocurrent in $LiNbO_3$ doped with either Fe or Cu. In our substrates, intended for optical waveguiding, the Fe density is intentionally kept low, nominally 5ppm, so that the photorefractive effect will be minimized. This also means that the photovoltaic effect will be small. Therefore, as Jerominek et al. point out [75], when an electric field is applied the carriers can travel in any direction. However since the power density in the bulk modes is still rather high, especially at the input end of the VIOWM, the number of photoexcited electrons need not be small. These carriers can be attracted to the high field regions near the electrode edges where they will counteract the applied field. When the switching speed is low enough for sufficient accumulation of charge in the high field regions the presence of the charge should, in fact, act initially to enhance the reversed field upon switching, i.e., an extended

---

* See Guenter and Huignard [74] for a detailed discussion of the photorefractive effect and photorefractive materials.

application of a negative voltage during the fly-back cycle may reduce the positive voltage needed to obtain a desired degree of optical confinement. Such an effect may prove to be beneficial in applications where there is a dead cycle. At higher switching rates the charges do not have time to accumulate and the decay effect need not be a problem. Figure 4.37 illustrates that for high speed switching there is essentially no decay in the output.

4.5 Discussion

In this section various results are highlighted and others are compared for both the predicted and the measured results.

The most important result is that the predicted behavior of the VIOWM, as a voltage controlled waveguide, has been verified. It has been demonstrated experimentally that the throughput of a VIOWM will increase with increasing voltage until a point is reached at which the coupling is maximized, then, upon further increasing the voltage the coupling will decrease.

Figures 4.1 through 4.4 show that the confinement of the modes is greater for 442 nm radiation than for 633 nm radiation for any particular gap width/operating voltage combination. This is to be expected as the change in the

refractive index is less at longer wavelengths due to the reduction in the value of the refractive index. Also we see that the confinement is expected to increase with decreasing gap width and with increasing voltage for planar devices. This is a reasonable result since the change in the refractive index is inversely proportional to the gap width and is directly proportional to the applied voltage.

Figure 4.9 indicates that for as little as 20 V applied to a planar VIOWM with a 2 μm interelectrode gap -3 dB coupling can be obtained when λ_o = 442 nm and for less than 25 V when the interelectrode gap is 4 μm.

The possible application of the planar VIOWM as a linear modulator has been demonstrated theoretically and linear regions have been seen in the outputs of the experimental devices; figures 4.15, 4.16, and 4.19.

Another result that was predicted by the theory and confirmed by experiment was the turn-on voltage for ridge waveguides. In fact figures 4.20 and 4.23 indicate that a half-height ridge VIOWM with a 7 μm interelectrode gap should have a turn-on voltage of about 17 V and figure 4.33 shows the turn-on voltage to be between 15 and 20 V. This is where the knee at the onset of the increase in the throughput occurs indicating a rapid change in the confinement of light to the ridge.

While ridge waveguides were not predicted to be very useful as linear modulators, figures 4.31 and 4.32, we see

from figure 4.33 that our device in fact demonstrates a very linear region. This is perhaps due to the walls of the experimental device being slanted allowing for a greater variation in the width of the mode than is predicted for devices with vertical walls in figures 4.23, 4.24, and 4.25.

Another result that is interesting is that increasing the height of a ridge VIOWM relative to the interelectrode gap width can increase the coupling between a device and a fiber at low voltages but it reduces the coupling that can be obtained at higher voltages; figures 4.28, 4.29, and 4.30.

The improved digital application of the ridge VIOWM over the planar as a digital switch is seen by comparing figure 4.14 with 4.33. The voltage difference between the knee at the onset of the increase in the throughput and the maximum value of the throughput for the planar VIOWM is a full 50 V whereas for the ridge device it is only about 30 V.

Ridge devices are predicted to be able to achieve -3 dB coupling for as little as 11 V.

Finally for both device types we were able to achieve large extinction ratios, > 20 dB, by applying a large negative voltage to induce a low refractive index anti-waveguide out of which light in bulk modes was steered. That the need for a negative voltage was due to bulk mode coupling in short, ~ 1 mm, was confirmed by tests on a long

device, where bulk mode coupling is much reduced, for which a 23 dB extinction ratio was obtained for a much reduced negative voltage.

Chapter 5

Summary, Conclusions, and Suggestions for Further Work

5.1 Introduction

Here the contents of the thesis are summarized. Then the conclusions that were drawn from this work are presented. The chapter is concluded by a section suggesting possible further research in this area.

5.2 Summary

In this thesis the VIOWM has been studied. Both planar and ridge type devices were modeled (chapter 2), fabricated (chapter 3), and results predicted by the theory and tests on the devices were presented (chapter 4).

The model was developed in terms of the theory that the electric field established by the application of voltage to

two electrodes, separated by a small gap, can create a waveguide in an electrooptic substrate. The electric field distributions established in both the planar and ridge devices were calculated by conformal mapping methods. Using the refractive index distribution in the substrate, caused by the applied electric field via the electrooptic effect, width parameters for Hermite-Gaussian approximations to the optical field distributions of the guided modes of the VIOWM were obtained by a variational technique. An expression for the coupling coefficient between an optical fiber and a VIOWM was developed based upon the approximate optical field distributions. It was possible using all of the above results to study the predicted behavior of a VIOWM as a voltage controlled coupler. One envisioned application is as a linking waveguide between two optical fibers another is as a front-end switch between a focused laser beam and an optical fiber. The VIOWM's use as either a linear modulator or as a digital switch was studied.

Planar devices with interelectrode gaps of 4 μm and ridge devices with 7.5 μm gaps and 4 μm high ridges were fabricated and tested.

Finally a planar device used in conjuction with a silicon V-groove that acted as a front-end switch between a focused Gaussian laser beam and an optical fiber was fabricated and tested.

5.3 Conclusions

The VIOWM offers considerable potential as an optical modulator. Its possible application as a linear modulator or as a digital switch has been demonstrated. A front-end switch has been fabricated.

Both theoretical predictions and measured results have shown that the VIOWM acts as a voltage controlled coupler. While the voltages used are relatively large when compared to those used in devices such as integrated optical Mach-Zehnders and cross-couplers they are of the same magnitude as those used in some polarization converters.* Also the dynamic region of the VIOWM is such that large changes in the output power can be achieved without the need to apply the entire on-off voltage, i.e., bias voltages could be used to reduce the voltage differences needed. Furthermore we have shown that the VIOWM can be used near the absorption edge of $LiNbO_3$. This opens the VIOWM to applications at wavelengths where other devices would suffer from the effects of the photorefractive effect. While the VIOWM suffers from the photorefractive effect as do the other

---

* Examples of voltage levels for these devices can be obtained from the data sheets provided for optical guided wave devices by companies such as Crystal Technology Inc., Palo Alto, California, U.S.A.

types of device it will recover upon the application of a fly-back cycle.

The planar device is easy to fabricate. It uses relatively less real estate than other integrated optical devices. It therefore promises to give high yields and to be inexpensive. It does not require an in-diffusion cycle in the fabrication nor do the electrodes require precise alignment with preformed waveguides.

The ridge device, while more difficult to fabricate, needs lower switching voltages. Furthermore the ridge seems to fix the width parameter in the z direction of the mode rather precisely. This could be an advantage in designing a device to operate with a specific optical fiber.

5.4 Suggestions for Further Work.

While we have attempted to make our theoretical analysis of the VIOWM as thorough as possible there is still room for further study. The is also room for improvement in the fabrication techniques used.

One area which warrants further study is the optimization of the length of the devices. It is important to have devices that are as short as possible to minimize the capacitance and to reduce losses. While our devices were short, ~ 1 mm, they needed a rather large reverse

voltage to increase the extinction ratio. It is desirable to reduce this voltage if possible.

Of course here the reverse voltage also served as a fly-back cycle to cause the devices to recover from the photorefractive effect. The effect of the photorefractive effect on the performance of the devices needs to be studied further. Naturally it can be reduced by reducing the power in the guided mode but this solution also reduces the VIOWM's utility. As we have shown application of a negative voltage, equal in magnitude to the positive voltage, is sufficient for the VIOWM to operate as a digital switch. However a study of the effect of applying a large voltage, either positive or negative, during a dead cycle may be useful in a certain applications by reducing the voltages needed during normal operation.

Better polishing techniques are needed, for both the VIOWMs and the optical fibers, than those that were used.

Other methods of fabricating the ridge waveguides could also be pursued. While our method was adequate for demonstrating the devices behavior better throughput should be possible if the ridge wall roughness was reduced.

Finally it would be interesting to investigate the effect of ridge wall slant on the performance of ridge VIOWMs. The difference between our predicted results for ridge VIOWMs with vertical walls and our measured results on a device with slanted walls indicates that devices with

slanted walls can incorporate both the turn-on voltage of a ridge VIOWM while preserving the highly linear regions found in planar devices.

Appendix A

THE ELECTROOPTIC EFFECT

A.1 Introduction

This appendix covers topics relevant to this thesis regarding the linear electrooptic effect. It begins with a discussion of the optical indicatrix and its relationship to the relative dielectric impermeability tensor. Then the linear electrooptic effect is discussed and the reduced electrooptic coefficient tensor for $LiNbO_3$ is given. Finally both equations 2.1 and 2.2, relating the deformation of the optical indicatrix to the applied electric field in our example, are derived.

A.2 The Relative Dielectric Impermeability Tensor

The optical indicatrix* specifies the refractive index of a crystal. The equation describing the ellipsoid is

$$\frac{x^2}{n_x^2} + \frac{y^2}{n_y^2} + \frac{z^2}{n_z^2} = 1$$

when x, y, and z are the principal axes. The coefficients of the above equation, $1/n_x^2$, $1/n_y^2$, and $1/n_z^2$, are the principal components of the relative dielectric impermeability tensor. The notation used above is not convenient when discussing tensor transformations therefore in this appendix the principal axes will be called the x_1, x_2, and x_3 axes following the convention used by Nye [23]. Using this notation each of the components of the relative dielectric impermeability tensor is given by

$$B_{ij} = \varepsilon_o \frac{\partial E_i}{\partial D_j} \quad (i = 1, 2, \text{ and } 3;\ j = 1, 2, \text{ and } 3)$$

where ε_o is the permittivity of free space and E_i optical electric field. The general representation quadric of the relative dielectric impermeability can then be described by

---

* Also called the index ellipsoid by some authors; see Yariv and Yeh [45] chapter 7 pp. 220-275.

$$B_{ij}x_i x_j = 1 \ .$$

where the Einstein summation convention is assumed.

The relative dielectric impermeability is a symmetrical tensor*, i.e., $B_{ij} = B_{ji}$. Therefore it is possible to reduce the number of independent components. The nine components are reduced to six as shown below:

$$\begin{bmatrix} B_{11} & B_{12} & B_{13} \\ B_{21} & B_{22} & B_{23} \\ B_{31} & B_{32} & B_{33} \end{bmatrix} \rightarrow \begin{bmatrix} B_1 & B_6 & B_5 \\ B_6 & B_2 & B_4 \\ B_5 & B_4 & B_3 \end{bmatrix} .$$

A.3 The Electrooptic Effect

The change in the refractive index of a crystal due to an applied electric field is known as the electrooptic effect. In general a change in the refractive index of a crystal will result in a change in the size and orientation of the optical indicatrix. Because of the relationship between the optical indicatrix and the components of the relative dielectric impermeability tensor changes in the optical indicatrix corresponds to changes in the coefficients B_{ij}.

When a crystal exhibits the linear electrooptic effect the changes in the B_{ij} are related to the applied electric

---

* See Nye [23] p. 246.

field (the low frequency field applied to the crystal as opposed to the high frequency optical field) via the linear electrooptic coefficients r_{ijk} by*

$$\Delta B_{ij} = r_{ijk} E_k \quad (i = 1, 2, 3;\ j = 1, 2, 3;\ k = 1, 2, 3)$$

or using the reduced index notation

$$\Delta B_i = r_{ij} E_j \quad (i = 1, 2, 3, 4, 5, 6;\ j = 1, 2, 3) \ .$$

$LiNbO_3$ is a member of the trigonal system of crystals and it is of class 3m.** When the x_1 axis is defined as the axis perpendicular to the mirror plane of the crystal, i.e., $x_1 \perp m$, then the electrooptic coefficient tensor has the nonzero components: r_{12}, r_{13}, r_{22}, r_{23}, r_{33}, r_{42}, r_{51}, and r_{61}. In matrix form the electrooptic coefficient tensor looks like

$$\begin{bmatrix} 0 & r_{12} & r_{13} \\ 0 & r_{22} & r_{23} \\ 0 & 0 & r_{33} \\ 0 & r_{42} & 0 \\ r_{51} & 0 & 0 \\ r_{61} & 0 & 0 \end{bmatrix} .$$

The change in the B_i $(i = 1, 2, 3, 4, 5, 6)$ due to the applied electric field is given by

---

* Here constant temperature and pressure are assumed.

** See Yariv and Yeh [45] p. 232.

$$\begin{vmatrix} \Delta B_1 \\ \Delta B_2 \\ \Delta B_3 \\ \Delta B_4 \\ \Delta B_5 \\ \Delta B_6 \end{vmatrix} = \begin{bmatrix} 0 & r_{12} & r_{13} \\ 0 & r_{22} & r_{23} \\ 0 & 0 & r_{33} \\ 0 & r_{42} & 0 \\ r_{51} & 0 & 0 \\ r_{61} & 0 & 0 \end{bmatrix} \begin{vmatrix} E_1 \\ E_2 \\ E_3 \end{vmatrix} .$$

In $LiNbO_3$ $-r_{12} = r_{22} = -r_{61} = 3.4\times10^{-12}$m/V, $r_{13} = r_{23} = 8.6\times10^{-12}$m/V, $r_{42} = r_{51} = 28.0\times10^{-12}$m/V, and $r_{33} = 30.8\times10^{-12}$m/V.* When the applied electric field is in the x_2x_3 plane the components of the relative dielectric impermeability tensor become

$$B_1 = \frac{1}{n_o^2} - r_{22}E_2 + r_{23}E_3 ,$$

$$B_2 = \frac{1}{n_o^2} + r_{22}E_2 + r_{23}E_3 ,$$

$$B_3 = \frac{1}{n_e^2} + r_{33}E_3 ,$$

$$B_4 = r_{42}E_2 ,$$

$B_5 = 0$, and

$B_6 = 0$.

---

* Ibid.

A.4 Equations 2.1 and 2.2

If, for this problem, the relative dielectric impermeability tensor were transformed to a new set of axes where $x_1' = x_2$, $x_2' = x_3$, and $x_3' = x_1$, then the Mohr circle construction as set out in Nye* [23] can be applied directly to find the distortion of the indicatrix in the x_2x_3 plane.

The transformation of a second rank tensor from one set of mutually perpendicular axes to another is given by**

$$T'_{ij} = a_{ik}a_{jl}T_{kl}$$

where the a's are direction cosines and T and T' are tensor quantities. The transformation of a second rank tensor from the x_i set of axes to the x_i' set of axes, described above, can be accomplished using the direction cosines $a_{11} = 0$, $a_{12} = 1$, $a_{13} = 0$, $a_{21} = 0$, $a_{22} = 0$, $a_{23} = 1$, $a_{31} = 1$, $a_{32} = 0$, and $a_{33} = 0$. The impermeability tensor referred to the new set of axes is

$$B'_1 = \frac{1}{n_o^2} + r_{22}E_2 + r_{23}E_3 ,$$

---

* Chapter II section 4 pp. 43-47

** Nye [23] p. 11.

$$B_2' = \frac{1}{n_e^2} + r_{33}E_3 ,$$

$$B_3' = \frac{1}{n_o^2} - r_{22}E_2 + r_{23}E_3 ,$$

$$B_4' = 0 ,$$

$$B_5' = 0 , \text{ and}$$

$$B_6' = r_{42}E_2 .$$

where the subscripts on the electrooptic coefficients and the electric field components are unchanged (i.e., they still refer to the original set of axes).

With no applied field the major and minor axes of the ellipse formed by taking a cross section of the indicatrix in the plane $x_3' = 0$ are principal axes of the indicatrix. Upon the application of an electric field the indicatrix deforms in both size and orientation. Since the only nonzero off diagonal element of the relative dielectric impermeability tensor under the influence of the field is B_6' the rotation of the indicatrix is about the x_3'-axis. This being the case the Mohr circle can be used to find the angle of rotation and the principal components of the new indicatrix (i.e., the indicatrix when the field is applied). If the new principal axes of the relative dielectric impermeability tensor are labeled x_1'' and x_2'' and the angle

of rotation, measured from x_1'' to x_1', is Θ, then the principal components of the tensor are given by

$$B_1'' = \frac{B_1' + B_2'}{2} - r$$

and

$$B_2'' = \frac{B_1' + B_2'}{2} + r$$

where

$$r = \left[\frac{(B_2' - B_1')^2}{4} + B_6'^2 \right]^{1/2}$$

and the relationship giving the angle θ is

$$\tan(2\Theta) = \frac{2B_6'}{B_2' - B_1'} .$$

By direct substitution we obtain equation 2.1

$$\tan(2\Theta) = \frac{2r_{42}E_y}{n_e^{-2} - n_o^{-2} + r_{33}E_z - r_{22}E_y - r_{23}E_z} . \qquad (2.1)$$

where $E_y = E_2$, and $E_z = E_3$.

To obtain equation 2.2 we begin by finding an expression for B_2''. First a simple substitution gives

$$B_2'' = \frac{B_1' + B_2'}{2} + \frac{B_2' - B_1'}{2}\left[1 + \left(\frac{2B_6'}{B_2' - B_1'}\right)^2\right]^{1/2}$$

here we can use the approximation $(1 + x)^{1/2} \approx 1 + x/2$ for small x* since $[2B_6'/(B_2' - B_1')]^2 \ll 1$. We can now write

$$B_2'' = \frac{B_1' + B_2'}{2} + \frac{B_2' - B_1'}{2} + \frac{B_6'^2}{B_2' - B_1'} = B_2' + \frac{B_6'^2}{B_2' - B_1'},$$

or,

$$\frac{1}{n_2''^2} = \frac{1}{n_e^2} + r_{33}E_z + \frac{(r_{42}E_y)^2}{n_e^{-2} - n_o^{-2} + r_{33}E_z - r_{22}E_y - r_{23}E_z}.$$

The last two terms on the right hand side of the above equation represent the change in the relative dielectric impermeability due to the application of an electric field, i.e.,

$$\Delta n_e^{-2} = r_{33}E_z + \frac{(r_{42}E_y)^2}{n_e^{-2} - n_o^{-2} + r_{33}E_z - r_{22}E_y - r_{23}E_z} \approx r_{33}E_z + \frac{(r_{42}E_y)^2}{n_e^{-2} - n_o^{-2}}.$$

The relationship between the change in the refractive index and the change in the relative dielectric impermeability is given by

---

* See Spiegel [76] p. 110.

$$\Delta n \approx -\frac{n^3 \Delta n}{2}$$

obtained from $dn^{-2}/dn = -2/n^3$ since $\Delta n \approx dn$ for small Δn.

Now we can write equation 2.2

$$\Delta n_e(y,z) \approx -\frac{n_e^3 r_{33} E_z(y,z)}{2} - \frac{n_e^3 \{r_{42} E_y(y,z)\}^2}{2(n_e^{-2} - n_o^{-2})} . \qquad (2.2)$$

Appendix B

STATIONARY FORMULAS

B.1 Introduction

This appendix provides the proofs to several of the assertions made in chapter 2 about the stationary nature of certain integrals.

B.2 Equation 2.10

In section 2.4 it is claimed that the integral equation

$$I = \int_{-\infty}^{\infty} \int_{-\infty}^{\infty} \left\{ \left(\frac{\partial \psi}{\partial y} \right)^2 + \left(\frac{\partial \psi}{\partial z} \right)^2 - v^2(y,z)\psi^2 \right\} dydz = 0 \qquad (2.10)$$

is stationary and that the general form of the wave equation

$$\nabla_t^2 \psi + v^2(y,z)\psi = 0 \ ,$$

is the Euler-Lagrange eqaution, where

$$\nabla_t^2 \psi = \frac{\partial^2 \psi}{\partial y^2} + \frac{\partial^2 \psi}{\partial z^2} .$$

This is proven by taking the first variation of eqaution 2.10 which is given by

$$\delta I = \int_{-\infty}^{\infty} \int_{-\infty}^{\infty} \left\{ \delta \left(\frac{\partial \psi}{\partial y} \right)^2 + \delta \left(\frac{\partial \psi}{\partial z} \right)^2 - \delta [\nu^2(y,z) \psi^2] \right\} dydz$$

or

$$\delta I = \int_{-\infty}^{\infty} \int_{-\infty}^{\infty} \left\{ 2 \frac{\partial \psi}{\partial y} \frac{\partial \delta\psi}{\partial y} + 2 \frac{\partial \psi}{\partial z} \frac{\partial \delta\psi}{\partial z} - 2\nu^2(y,z) \psi \delta\psi - 2\psi^2 \nu(y,z) \delta\nu(y,z) \right\} dydz .$$

Applying Green's theorem to the first two terms in the above integral one obtains

$$\int_{-\infty}^{\infty} \int_{-\infty}^{\infty} \left\{ 2 \frac{\partial \psi}{\partial y} \frac{\partial \delta\psi}{\partial y} + 2 \frac{\partial \psi}{\partial z} \frac{\partial \delta\psi}{\partial z} \right\} dydz =$$

$$- \int_{-\infty}^{\infty} \int_{-\infty}^{\infty} 2\delta\psi \left(\frac{\partial^2 \psi}{\partial y^2} + \frac{\partial^2 \psi}{\partial z^2} \right) dydz + \int_C \delta\psi \frac{\partial \psi}{\partial n} ds$$

and the first variation of equation 2.10 becomes

$$\delta I = \int_{-\infty}^{\infty} \int_{-\infty}^{\infty} \left\{ - 2\delta\psi \left(\frac{\partial^2 \psi}{\partial y^2} + \frac{\partial^2 \psi}{\partial z^2} + \nu^2(y,z) \psi \right) - 2\psi^2 \nu(y,z) \delta\nu(y,z) \right\} dydz .$$

of which the expression contained within the parentheses is recognized to be the general form of the scalar wave equation and is equal to zero. Hence the general form of the scalar wave equation is the Euler-Lagrange equation provided that $v(y,z)$ is stationary, i.e., if the first variation of integral is to be zero then the last term in the integral must also be equal to zero which implies that $v(y,z)$ must be stationary, i.e.

$$\delta v(y,z) = 0 .$$

B.3 The Propagation Constant

The purpose of this section is to show that the propagation constant is a stationary value. To do this one begins with the equation

$$\beta_v^2 = - \frac{\int_{-\infty}^{\infty}\int_{-\infty}^{\infty}\left\{\left(\frac{\partial\psi}{\partial y}\right)^2+\left(\frac{\partial\psi}{\partial z}\right)^2-\left[\frac{\partial^2 \ln[n_z^2(y,z)]}{\partial z^2}-\frac{z}{w_{zv}^2}\frac{\partial \ln[n_z^2(y,z)]}{\partial z}+n_z^2(y,z)k_o^2\right]\psi^2\right\}dydz}{\int_{-\infty}^{\infty}\int_{-\infty}^{\infty}\psi^2\,dydz}$$

and takes its first variation. If the integral in the numerator on the right hand side of the above equation is labelled I_1 and the integral in the denominator is labelled I_2 then the first variation is given by

$$\delta\beta_v^2 = 2\beta_v\delta\beta_v = \delta\left(-\frac{I_1}{I_2}\right) = -\frac{I_2\delta I_1 - I_1\delta I_2}{I_2^2} = -\frac{\delta I_1 + \beta_v^2\delta I_2}{I_2} . \qquad \text{(B1.1)}$$

The first variation of I_1 is

$$\delta I_1 = \int_{-\infty}^{\infty}\int_{-\infty}^{\infty}\left\{ 2\frac{\partial\psi}{\partial y}\frac{\partial\delta\psi}{\partial y} + 2\frac{\partial\psi}{\partial z}\frac{\partial\delta\psi}{\partial z} - 2\rho^2(y,z)\psi\delta\psi - 2\psi^2\rho(y,z)\delta\rho(y,z) \right\} dydz .$$

where

$$\rho^2(y,z) = \left\{ \frac{\partial^2 \ln[n_z^2(y,z)]}{\partial z^2} - \frac{z}{w_{zv}^2}\frac{\partial \ln[n_z^2(y,z)]}{\partial z} + n_z^2(y,z)k_o^2 \right\}$$

and the first variation of integral I_2 is

$$\delta I_2 = \int_{-\infty}^{\infty}\int_{-\infty}^{\infty} 2\psi\delta\psi \; dydz$$

so that the terms

$$\beta_v^2\delta I_2 = \beta_v^2\int_{-\infty}^{\infty}\int_{-\infty}^{\infty} 2\psi\delta\psi \; dydz$$

and

$$-\int_{-\infty}^{\infty}\int_{-\infty}^{\infty} 2\rho^2(y,z)\psi\delta\psi \; dydz$$

can be combined to result in

$$-\int_{-\infty}^{\infty}\int_{-\infty}^{\infty} 2\rho^2(y,z)\psi\delta\psi \; dydz + \beta_v^2\int_{-\infty}^{\infty}\int_{-\infty}^{\infty} 2\psi\delta\psi \; dydz = -\int_{-\infty}^{\infty}\int_{-\infty}^{\infty} 2\nu^2(y,z)\psi\delta\psi \; dydz .$$

Applying Green's theorem to the first to terms in δI_1 gives

$$\int_{-\infty}^{\infty}\int_{-\infty}^{\infty}\left\{ 2\frac{\partial\psi}{\partial y}\frac{\partial\delta\psi}{\partial y} + 2\frac{\partial\psi}{\partial z}\frac{\partial\delta\psi}{\partial z}\right\} dydz =$$

$$-\int_{-\infty}^{\infty}\int_{-\infty}^{\infty} 2\delta\psi\left(\frac{\partial^2\psi}{\partial y^2}+\frac{\partial^2\psi}{\partial z^2}\right) dydz + \int_C \delta\psi\frac{\partial\psi}{\partial n}\,ds$$

and the numerator of equation B1.1 becomes

$$\int_{-\infty}^{\infty}\int_{-\infty}^{\infty}\left\{ -2\delta\psi\left(\frac{\partial^2\psi}{\partial y^2}+\frac{\partial^2\psi}{\partial z^2}+\nu^2(y,z)\psi\right) - 2\psi^2\rho(y,z)\delta\rho(y,z)\right\} dydz\ .$$

The expression within the parentheses is recognizable as the scalar wave equation and is equal to zero. It follows that $\delta\beta_v$ is stationary provided that the first variation of $\rho(y,z)$ is zero i.e.

$$\delta\rho(y,z) = 0$$

which is obviously so provided that an a priori knowledge of w_{zv} is assumed.

Appendix C

THE COUPLING COEFFICIENT

C.1 Introduction

In this appendix equation 2.17 is derived. In section 2.6 we derived the expression

$$T = \frac{2a_f\beta_f \int_{-\infty}^{\infty}\int_{0}^{\infty}\left(\frac{y}{w_{yv}}\right) e^{-\{y^2/w_{yv}^2+z^2/w_{zv}^2+(y-a)^2/w_{yf}^2+(z-b)^2/w_{zf}^2\}/2}\,dydz}{a_v(\beta_f+\beta_v)\int_{-\infty}^{\infty}\int_{0}^{\infty}\left(\frac{y}{w_{yv}}\right)^2 e^{-(y^2/w_{yv}^2+z^2/w_{zv}^2)}\,dydz}$$

by assuming that the power coupled to reflected radiated modes could be neglected. This was done using the approximate field distributions motivated in section 2.5 for the optical fiber and the VIOWM. Here the variables a and b locate the center of the optical fiber relative to the

center of the surface of the waveguiding region of the VIOWM.

C.2 The Normalized Amplitudes a_f and a_v

The time-averaged power propagating in a guided mode of an optical waveguide may be given terms of the fields by*

$$P = \frac{1}{2} \mathrm{Re} \int_{-\infty}^{\infty}\int_{-\infty}^{\infty} \left[\mathbf{E} \times \mathbf{H}^* \right] \cdot \mathbf{u}_x \, dydz$$

where $\mathbf{E}$ is the electric field, $\mathbf{H}$ is the magnetic field, and $\mathbf{u}_x$ is a unit vector in the direction of propagation. When the electric field of the guided mode is polarized in the plane normal to the direction propagation, the transverse plane, the mode is called a transverse electric or TE mode. The expression for the power in a TE mode may be reduced to

$$P = \frac{\beta}{2\mu\omega} \int_{-\infty}^{\infty}\int_{-\infty}^{\infty} \left| E_t \right|^2 dydz$$

where the subscript t indicates the transverse component of the electric field. In our case the transverse component of the electric field is polarized parallel the z-axis and is

---

* See for example Snyder and Love [77] chapter 11 pp. 208-237.

given for the optical fiber by equation 2.11 and for the VIOWM by equation 2.12.

If the power in the mode is normalized so that the mode carries p Watts then the amplitude of the field is calculated using

$$a_f^2 = \frac{2\mu_f \omega p}{\beta_f \int_{-\infty}^{\infty}\int_{-\infty}^{\infty} e^{-(y^2/w_{yf}^2 + z^2/w_{zf}^2)}\, dydz}$$

for the fiber and using

$$a_v^2 = \frac{2\mu_v \omega p}{\beta_v \int_{-\infty}^{\infty}\int_{0}^{\infty} \left(\frac{y}{w_{yv}}\right)^2 e^{-(y^2/w_{yv}^2 + z^2/w_{zv}^2)}\, dydz}$$

for the VIOWM.

The ratio a_f/a_v is determined by taking the square root of the ratio a_f^2/a_v^2 and by assuming that $\mu_f = \mu_v = \mu_o$. It is given by

$$\frac{a_f}{a_v} = \left[\frac{\beta_v \int_{-\infty}^{\infty}\int_{0}^{\infty} \left(\frac{y}{w_{yv}}\right)^2 e^{-(y^2/w_{yv}^2 + z^2/w_{zv}^2)}\, dydz}{\beta_f \int_{-\infty}^{\infty}\int_{-\infty}^{\infty} e^{-(y^2/w_{yf}^2 + z^2/w_{zf}^2)}\, dydz} \right]^{\frac{1}{2}}.$$

Substituting the ratio a_f/a_v into the expression for the coupling coefficient gives

$$T = \frac{2(\beta_v\beta_f)^{1/2}\int_{-\infty}^{\infty}\int_{0}^{\infty}\left(\frac{y}{w_{yv}}\right)e^{-\{y^2/w_{yv}^2+z^2/w_{zv}^2+(y-a)^2/w_{yf}^2+(z-b)^2/w_{zf}^2\}/2}dydz}{(\beta_f+\beta_v)\left[\int_{-\infty}^{\infty}\int_{-\infty}^{\infty}e^{-(y^2/w_{yf}^2+z^2/w_{zf}^2)}dydz\int_{-\infty}^{\infty}\int_{0}^{\infty}\left(\frac{y}{w_{yv}}\right)^2 e^{-(y^2/w_{yv}^2+z^2/w_{zv}^2)}dydz\right]^{\frac{1}{2}}}.$$

C.3 The Numerator of the Coupling Coefficient

The integral in the numerator of the above expression for the coupling coefficient is

$$\Gamma = \int_{-\infty}^{\infty}\int_{0}^{\infty}\left(\frac{y}{w_{yv}}\right)e^{-\{y^2/w_{yv}^2 + z^2/w_{zv}^2 + (y-a)^2/w_{yf}^2 + (z-b)^2/w_{zf}^2\}/2}dydz .$$

First the integral is to separated into two integrals one in y and one in z

$$\Gamma = e^{-a^2/2w_{yf}^2-b^2/2w_{zf}^2}\int_{0}^{\infty}\left(\frac{y}{w_{yv}}\right)e^{-y^2/\Omega_y+ay/w_{yf}^2}dy\int_{-\infty}^{\infty}e^{-z^2/\Omega_z+bz/w_{zf}^2}dz$$

where

$$\Omega_y = \frac{2w_{yv}^2 w_{yf}^2}{w_{yv}^2 + w_{yf}^2}$$

and

$$\Omega_z = \frac{2w_{zv}^2 w_{zf}^2}{w_{zv}^2 + w_{zf}^2} .$$

Next the substitutions of variables

$$y' = \frac{y}{\Omega_y^{1/2}}$$

and

$$z' = \frac{z}{\Omega_z^{1/2}}$$

are made yielding

$$\Gamma = \frac{\Omega_y \Omega_z^{1/2}}{w_{yv}} e^{-(a^2/w_{yf}^2 + b^2/w_{zf}^2)/2} \int_0^\infty y' e^{-y'^2 + a\Omega_y^{1/2} y'/w_{yf}^2} dy' \int_{-\infty}^{\infty} e^{-z'^2 + b\Omega^{1/2} z'/w_{zf}^2} dz' .$$

We shall solve the above integrals one at a time begining with

$$\int_0^\infty y' \, e^{-y'^2 + a\Omega_y^{1/2} y'/w_{yf}^2} \, dy'$$

which can be written in terms of the Hermite polynomial $H_1(y')$

$$\int_0^\infty y' \, e^{-y'^2 + a\Omega_y^{1/2} y'/w_{yf}^2} \, dy' = \frac{1}{2} \int_0^\infty H_1(y') \, e^{-y'^2 + a\Omega_y^{1/2} y'/w_{yf}^2} \, dy' \, .$$

The generating function for Hermite polynomials is*

$$H_n(x) = (-1)^n \, e^{x^2} \, \frac{d^n \, e^{-x^2}}{dx^n} \, , \quad n = 0,1,2,\ldots$$

which can be substituted into the preceding integral giving

$$\int_0^\infty H_1(y') \, e^{-y'^2 + a\Omega_y^{1/2} y'/w_{yf}^2} \, dy' = - \int_0^\infty e^{a\Omega_y^{1/2} y'/w_{yf}^2} \, \frac{de^{-y'^2}}{dy'} \, dy' =$$

$$- \int_0^\infty e^{a\Omega_y^{1/2} y'/w_{yf}^2} \, de^{-y'^2} \, .$$

the last term of which is solved using integration by parts**

$$- \int_0^\infty e^{a\Omega_y^{1/2} y'/w_{yf}^2} \, de^{-y'^2} =$$

---

* Lebedev [78] p. 60.

** All of the integrals in this appendix involving exponentials can be solved using the formulas in Spiegel [79] on p. 98 and using the special values for the gamma function on p. 101.

$$- e^{-y'^2 + a\Omega_y^{1/2} y'/w_{yf}^2} \Big|_0^\infty + \int_0^\infty e^{-y'^2 + a\Omega_y^{1/2} y'/w_{yf}^2} dy' =$$

$$1 + \frac{a\Omega_y^{1/2}\pi^{1/2}}{2w_{yf}^2} e^{a^2\Omega_y/4w_{yf}^4} \operatorname{erfc}\left(\frac{-a\Omega^{1/2}}{2w_{yf}^2} \right) .$$

The second integral is easily solved giving

$$\int_{-\infty}^{\infty} e^{-z'^2 + b\Omega^{1/2} z'/w_{zf}^2} dz' = \pi^{1/2} e^{b^2\Omega_z/4w_{zf}^4} .$$

The numerator of the coupling coefficient can now be written as

$$\Gamma = \frac{\Omega_y \Omega_z^{1/2}}{2w_{yv}} \pi^{1/2} e^{-(a^2/w_{yf}^2 + b^2/w_{zf}^2)/2 + b^2\Omega_z/4w_{zf}^4}$$

$$\times \left[1 + \frac{a\Omega_y^{1/2}\pi^{1/2}}{2w_{yf}^2} e^{a^2\Omega_y/4w_{yf}^4} \operatorname{erfc}\left(\frac{-a\Omega^{1/2}}{2w_{yf}^2} \right) \right] .$$

C.4 The Denominator of the Coupling Coefficient

The integrals in the denominator of the expression for the coupling coefficient are

$$\Gamma' = \int_{-\infty}^{\infty}\int_{-\infty}^{\infty} e^{-(y^2/w_{yf}^2 + z^2/w_{zf}^2)}\,dydz \int_{-\infty}^{\infty}\int_{0}^{\infty} \left(\frac{y}{w_{yv}}\right)^2 e^{-(y^2/w_{yv}^2 + z^2/w_{zv}^2)}\,dydz$$

which can be separated into four integrals each of which is solved in a straight forward manner

$$\int_{-\infty}^{\infty} e^{-y^2/w_{yf}^2}\,dy = w_{yf}\pi^{1/2} ,$$

$$\int_{-\infty}^{\infty} e^{-z^2/w_{zf}^2}\,dz = w_{zf}\pi^{1/2} ,$$

$$\int_{0}^{\infty} \left(\frac{y}{w_{yv}}\right)^2 e^{-y^2/w_{yv}^2}\,dy = \frac{w_{yv}\pi^{1/2}}{4} ,$$

and

$$\int_{-\infty}^{\infty} e^{-z^2/w_{zv}^2}\,dz = w_{zv}\pi^{1/2} .$$

The expression for Γ' becomes

$$\Gamma' = \frac{w_{yv}w_{zv}w_{yf}w_{zf}\pi^2}{4}$$

or for $\Gamma'^{1/2}$

$$\Gamma'^{1/2} = \frac{(w_{yv}w_{zv}w_{yf}w_{zf})^{1/2}\,\pi}{2}$$

C.5 Equation 2.17

Now the coupling coefficient can be given by

$$T = \frac{2(\beta_f \beta_v)^{1/2} \Gamma}{(\beta_f + \beta_v)\ \Gamma'^{1/2}}$$

which reduces to

$$T = \frac{2(\beta_f \beta_v)^{1/2} \Omega_y \Omega_z^{1/2}\ e^{-(a^2/w_{yf}^2 + b^2/w_{zf}^2)/2 + b^2\Omega_z/4w_{zf}^4}}{\pi^{1/2}(\beta_f + \beta_v)(w_{yv} w_{zv} w_{yf} w_{zf})^{1/2} w_{yv}}$$

$$\times \left[1 + \frac{a\Omega_y^{1/2} \pi^{1/2}\ e^{a^2\Omega_y/4w_{yf}^4}\ \mathrm{erfc}\left(\frac{-a\Omega_y^{1/2}}{2w_{yf}^2} \right)}{2w_{yf}^2} \right] \qquad (2.17)$$

References

1. R. V. Schmidt and I. P. Kaminow, "Metal-diffused optical waveguides in $LiNbO_3$," Appl. Phys. Lett., vol. 25, no. 8, pp. 458-460, 1974.

2. J. L. Jackel, C. E. Rice, and J. J. Veselka, "Proton exchange for high-index waveguides in $LiNbO_3$," Appl. Phys. Lett., vol. 47, no. 7, pp. 607-608, 1982.

3. M. Papuchon, Y. Combemale, X. Mathieu, D. B. Ostrowsky, L. Reiber, A. M. Roy, B. Sejourne, and M. Werner, "Electrically switched optical directional coupler: Cobra," Appl. Phys. Lett., vol. 27, no. 5, pp. 289-291, 1975.

4. Y. Ohmachi and J. Noda, "Electro-optic light modulator with branched ridge waveguide," Appl. Phys. Lett., vol. 27, no. 10, pp. 544-546, 1975.

5. M. Papuchon, A. M. Roy,and D. B. Ostrowsky, "Electrically active optical bifurcation: Boa," Appl. Phys. Lett., vol. 31, no. 4, pp. 266-267, 1977.

6. W. K. Burns, T. G. Giallorenzi, R. P. Moeller, and E. J. West, "Interferometric waveguide modulator with polarization independent operation," Appl. Phys. Lett., vol. 33, no. 11, pp. 944-947, 1978.

7. Y. Silverberg, P. Perlmutter, and J. E. Baran, "Digital optical switch," Appl. Phys. Lett., vol. 51, no. 16, pp. 1230-1232, 1987.

8. R. C. Alferness, "Efficient waveguide electro-optic TE↔TM mode converter/wavelength filter," Appl. Phys. Lett., vol. 36, no. 7, pp. 513-515, 1980.

9. Suwat Thaniyavarn, "Wavelength independent, optical damage immune Z-propagation $LiNbO_3$ waveguide polarization converter," Appl. Phys. Lett., vol. 47, no. 7, pp. 674-677, 1985.

10. F. Heismann and R. Ulrich, "Integrated-Optical Single-Sideband Modulator and Phase Shifter," IEEE J. Quantum Electron., vol QE-18, no. 4, pp. 767-771, 1982.

11. W. A. Stallard, B. E. Daymond-John, and R. C. Booth, "$LiNbO_3$ Optical Frequency Translators for Coherent Optical Fibre Systems," Integrated Optics, Berlin: Springer-Verlag, pp. 164-168, 1985.

12. D. J. Channin, "Voltage-induced optical waveguide," Appl. Phys. Lett., vol. 19, no. 5, pp. 128-130, 1971.

13. R. A. Soref and A. R. Nelson, "Compound optical crosspoint with low crosstalk," Appl. Opt., vol. 16, no. 12, pp. 3223-3229, 1977.

14. J. C. Baumert, C. Walther, P. Buchmann, H. Melchior, and P. Guenter, "Electro-optically Induced Optical Waveguide in $KNbO_3$," Integrated Optics, Berlin: Springer-Verlag, pp. 44-48, 1985.

15. I. Savatinova, S. Tonchev, K. Pushkarov, and F. Scharf, "Electrically Induced Ti:$LiNbO_3$ Strip Waveguides: Effect of Electrooptic Modulation," J. Opt. Commun., vol. 5, no. 1, pp. 10-15, 1984.

16. R. A. Soref, D. H. McMahon, and A. R. Nelson, "Multimode achromatic electro-optic waveguide switch for fiber-optic communications," Appl. Phys. Lett., vol. 28, no. 12, pp. 716-718, 1976.

17. W. K. Burns and G. B. Hocker, "End fire coupling between optical fibers and diffused channel waveguides," Appl. Opt., vol. 16, no. 8, pp. 2048-2050, 1977.

18. M. Kawabe, S. Hirata, and S. Namba, "Ridge Waveguides and Electro-Optical Switches in $LiNbO_3$ Fabricated by Ion-Bombardment-Enhanced Etching," IEEE Trans. Circ. and Syst., vol. CAS-26, no. 12, pp. 1109-1112, 1979.

19. D. Marcuse, Light Transmission Optics 2nd Edition, New York: Van Nostrand Reinhold, 1982.

20. C. M. Miller, "Fiber-Optic Array Splicing With Etched Silicon Chips," Bell Syst. Tech. J., vol. 57, no. 1, pp. 75-90, 1976.

21. H. P. Hsu and A. F. Milton, "Flip-chip approach to endfire coupling between single-mode optical fibres and channel waveguides," Electron. Lett., vol. 12, no. 16, pp. 404-405, 1976.

22. F. S. Chen, "Optically Induced Change of Refractive Index in $LiNbO_3$ and $LiTaO_3$," J. Appl. Phys., vol. 40, no. 8, pp. 3389-3396, 1969.

23. J. F. Nye, Physical Properties of Crystals, Oxford: Oxford University Press, 1979.

24. A. Yariv, Introduction to Optical Electronics 2nd Edition, New York: Holt, Rinehart, and Winston, 1976.

25. E. A. J. Marcatili, "Dielectric Rectangular Waveguide and Directional Coupler for Integrated Optics," Bell Syst. Tech. J., vol. 48, no. 7, pp. 2071-2102, 1969.

26. S. Ramo, J. R. Whinnery, and T. Van Duzer, Fields and Waves in Communications Electronics 2nd Edition, John Wiley and Sons, 1984.

27. M. E. Lines and A. M. Glass, Principles and Applications of Ferroelectrics and Related Materials, Oxford: Oxford University Press, 1977.

28. A. Nussbaum, Electromagnetic Theory for Engineers and Scientists, New Jersey: Prentice-Hall, 1965.

29. E. Snitzer, "Cylindrical Dielectric Waveguide Modes," J. Opt. Soc. Am., vol. 51, no. 5, pp. 491-498, 1961.

30. C. Yeh, "Elliptical Dielectric Waveguides," J. Appl. Phys., vol. 33, no. 11, pp. 3235-3243, 1962.

31. H. A. Haus, Waves and Fields in Optoelectronics, New Jersey: Prentice-Hall, 1984.

32. R. M. Knox and P. P. Toulios, "Integrated Circuits for the Millimeter Through Optical Frequency Range," Symposium on Submillimeter Waves Polytechnic Institute of Brooklyn, pp. 497-516, March 31 - April 2, 1970.

33. G. B. Hocker and W. K. Burns, "Modes in Diffused Optical Waveguides of Arbitrary Index Profile," IEEE J. Quantum Electron., vol. QE-11, no. 6, pp. 270-276, 1975.

34. R. W. Hornbeck, Numerical Methods, New Jersey: Prentice-Hall, 1975.

35. S. Ahmed and P. Daly, "Finite-element methods for inhomogeneous waveguides," Proc. IEE, vol. 116, no. 10, pp. 1661-1664, 1969.

36. C. Yeh, S. D. Dong, and W. Oliver, "Arbitrarily shaped inhomogeneous optical fiber or integrated optical waveguides," J. Appl. Phys., vol. 46, no. 5, pp. 2125-2129, 1975.

37. M. Koshiba, K. Hayata, and M. Suzuki, "Approximate Scalar Finite-Element Analysis of Anisotropic Optical Waveguides with Off-Diagonal Elements in a Permittivity Tensor," IEEE Trans. Microwave Theory and Tech., vol. MTT-32, no. 6, pp. 587-593, 1984.

38. J. E. Goell, "A Circular-Harmonic Computer Analysis of Rectangular Dielectric Waveguides," Bell Syst. Tech. J., vol. 48, no. 7, pp. 2133-2160, 1969.

39. E. Conwell, "Optical waveguiding in graded-index layers," Appl. Phys. Lett., vol. 25, no. 1, pp. 40-42, 1974.

40. L. Eyges, P. Gianino, and P. Wintersteiner, "Modes of dielectric waveguides of arbitrary cross sectional shape," J Opt. Soc. Am., vol. 69, no. 9, pp. 1226-1235, 1979.

41. D. Marcuse, "Gaussian approximation of the fundamental modes of graded-index fibers," J. Opt. Soc. Am., vol. 68, no. 1, pp. 103-109, 1978.

42. R. F. Harrington, Time-Harmonic Electromagnetic Fields, New York: McGraw-Hill, 1961.

43. T. Okoshi, Optical Fibers, New York: Academic Press, 1982.

44. P. P. Silvester and R. L. Ferrari, Finite Elements for Electrical Engineers, Cambridge: Cambridge University Press, 1983.

45. A. Yariv and P. Yeh, Optical Waves in Crystals, New York: John Wiley and Sons, 1984.

46. C. Fox, An Introduction to the Calculus of Variations, New York: Dover Publications, 1987.

47. J. T. Verdeyen, Laser Electronics, New Jersey, Prentice-Hall, 1981.

48. L. G. Cohen, "Power Coupling from GaAs Injection Lasers into Optical Fibers," Bell Syst. Tech. J., vol. 51, no. 3, pp. 573-594, 1971.

49. R. Keil and F. Auracher, "Coupling of single-mode Ti-diffused $LiNbO_3$ waveguides to single-mode fibers," Opt. Commun., vol. 30, no. 1, pp. 23-28, 1979.

50. P. G. Suchoski, Jr. and R. V. Ramaswamy, "Minimum-Mode-Size Low-Loss Ti:$LiNbO_3$ Channel Waveguides for Efficient Modulator Operation at 1.3 μm," IEEE J. Quantum Electron., vol QE-23, no. 10, pp. 1673-1679, 1987.

51. W. K. Burns and A. F. Milton, "Mode Conversion in Planar-Dielectric Separating Waveguides," IEEE J. Quantum Electron., vol QE-11, no. 1, pp. 32-39, 1975.

52. R. G. Hunsperger, A. Yariv, and A. Lee, "Parallel end-butt coupling for optical integrated circuits," Appl. Opt., vol. 16, no. 4, pp. 1026-1032, 1977.

53. M. Hatzakis, B. J. Canavello, and J. M. Shaw, "Single-Step Optical Lift-Off Process," IBM J. Res. Develop., vol. 24, no. 4, pp. 452-460, 1980.

54. S. K. Ghandhi, VLSI Fabrication Principles, New York: John Wiley and Sons, 1983.

55. I. P. Kaminow, V. Ramaswamy, R. V. Schmidt, and E. H. Turner, "Lithium niobate ridge waveguide modulator," Appl. Phys. Lett., vol. 24, no. 12, pp. 622-624, 1974.

56. C. L. Lee and C. L. Lu, "CF_4 plasma etching on $LiNbO_3$," Appl. Phys. Lett., vol. 35, no. 10, pp. 756-758, 1979.

57. S. Matsui, T. Yamato, H. Aritome, and S. Namba, "Microfabrication of $LiNbO_3$ by Reactive Ion-Beam Etching," Japanese J. Appl. Phys., vol. 19, no. 8, pp. L463-L465, 1980.

58. J. L. Jackel, R. E. Howard, E. L. Hu, and S. P. Lyman, "Reactive ion etching of $LiNbO_3$," Appl. Phys. Lett., vol. 38, no. 11, pp. 907-909, 1981.

59. D. B. Lee, "Anisotropic Etching of Silicon," J. Appl. Phys., vol. 40, no. 11, pp. 4569-4574, 1969.

60. W. Kern, "Chemical Etching of Silicon, Germanium, Gallium Arsenide, and Gallium Phosphide," RCA Review, vol. 39, pp. 278-308, 1978.

61. S. K. Sheem and T. G. Giallorenzi, "Two-dimensional silicon grooves for altitudinal alignment in fiber end-butt coupling," Opt. Lett., vol. 3, no. 3, pp. 73-75, 1978.

62. W. Kern and D. A. Puotinen, "Cleaning Solutions Based on Hydrogen Peroxide for use in Silicon Semiconductor Technology," RCA Review, vol. 31, no. 2, pp. 187-206, 1970.

63. B. E. Deal, "The Oxidation of Silicon in Dry Oxygen, Wet Oxygen and Steam," J. Electrochem. Soc., vol. 110, no. 6, pp. 527-533, 1963.

64. D. F. Nelson and R. M. Mikulyak, "Refractive indicies of congruently melting lithium niobate," J. Appl. Phys., vol. 45, no. 8, pp. 3688-3689, 1974.

65. R. J. Collier, C. B. Burckhardt, and L. H. Lin, Optical Holography, New York: Academic Press, 1971.

66. J. W. Goodman, Introduction to Fourier Optics, New York: McGraw-Hill, 1968.

67. N. A. F. Jaeger and L. Young, "Voltage-Induced Optical Waveguide Modulator in Lithium Niobate," IEEE J. Quantum Electron., scheduled to appear April 1989.

68. I. P. Kaminow and L. W. Stulz, "Loss in cleaved Ti-diffused $LiNbO_3$ waveguides," Appl. Phys. Lett., vol. 33, no. 1, pp. 62-64, 1978.

69. N. A. F. Jaeger and L. Young, "Integrated Optical Modulator," Final report to the science council of British Columbia, Grant #74 RC-12, 35 pages, 1986.

70. S. Thaniyavarn, T. Findakly, D. Booher, and J. Moen, "Domain inversion effects in Ti-$LiNbO_3$ integrated optical devices," Appl. Phys. Lett., vol. 46, no. 10, pp. 933-935, 1985.

71. L. L. Pendergrass, "Ferroelectric microdomain reversal at room temperature in lithium niobate," J. Appl. Phys., vol. 62, no. 1, pp. 231- 236, 1987.

72. J. C. Peuzin, "Comment on 'Domain inversion effects in Ti-$LiNbO_3$ integrated optical devices,'" Appl. Phys. Lett., vol. 48, no. 16, pp. 1104-1105, 1986.

73. E. Kraetzig and H.Kurz, "Spectral Dependence of the Photorefractive Recording and Erasure Process in Doped $LiNbO_3$," Ferroelectrics, vol. 10, pp. 159-162, 1976.

74. P. Guenter and J. P. Huignard, Photorefractive Materials and Their Applications I, Berlin: Springer-Verlag, 1988.

75. H. Jerominek, C. Delisle, and R. Tremblay, "Optical branching effect in Ti:$LiNbO_3$ waveguides: near-field pattern studies," Appl. Opt., vol. 25, no. 5, pp. 732-736, 1986.

76. M. R. Spiegel, Mathematical Handbook of Formulas and Tables, New York: McGraw-Hill, 1968.

77. A. W. Snyder and J. D. Love, Optical Waveguide Theory, London: Chapman and Hall, 1983.

78. N. N. Lebedev, Special Functions and Their Applications, New York: Dover Publications, 1972.